Fall 12-15-2021

Thermal and Mechanical Numerical Modeling of Extrusion-based 3d Printed Reinforced Polymers for Selecting Manufacturing Process Parameters

Sunil Bhandari
University of Maine, sunil.bhandari@maine.edu

THERMAL AND MECHANICAL NUMERICAL MODELING OF EXTRUSION-BASED 3D PRINTED REINFORCED POLYMERS FOR SELECTING MANUFACTURING PROCESS PARAMETERS

By

Sunil Bhandari

B.Eng. Tribhuvan University, 2012

M.Sc. University of Maine, 2017

A DISSERTATION

Submitted in Partial Fulfillment of the

Requirements for the Degree of

Doctor of Philosophy

(in Civil Engineering)

The Graduate School

The University of Maine

December 2021

Advisory Committee:

Roberto A. Lopez-Anido, Professor of Civil Engineering, Committee Chair

Douglas J. Gardner, Professor of School of Forest Resources, Committee Co-chair

William G. Davids, Professor of Civil Engineering

Senthil Vel, Professor of Mechanical Engineering

Bashir Khoda, Assistant Professor of Mechanical Engineering

THERMAL AND MECHANICAL NUMERICAL MODELING OF EXTRUSION-BASED 3D PRINTED REINFORCED POLYMERS FOR MANUFACTURING PROCESS IMPROVEMENT

By Sunil Bhandari

Dissertation Advisors: Dr. Roberto A. Lopez-Anido and Dr. Douglas J. Gardner

An Abstract of the Dissertation Presented
in Partial Fulfillment of the Requirements for the
Degree of Doctor of Philosophy
(in Civil Engineering)
December 2021

Extrusion-based 3D printing of thermoplastic polymer composites manufactures parts that have non-homogenous, orthotropic, and process-dependent macro-scale material properties. As a part of the dissertation, research works were carried out to:

- improve the interlayer mechanical properties and reduce the orthotropy,
- use experimentally homogenized orthotropic material properties to numerically model the mechanical behavior of the non-homogenous orthotropic 3D printed parts,
- create an efficient numerical thermal model to predict the process-dependent thermal history of the 3D printed part, and
- aid the manufacturing process by selecting a suitable set of processing parameters based on a simplified sequentially coupled thermomechanical model.

The dissertation presents four studies that improve the understanding of the mechanical behavior and aid the manufacturing process of the 3D printed thermoplastic polymer composites. Three journal publications that resulted from the research work carried out are listed below:

- *Bhandari, S., Lopez-Anido, R. A., & Gardner, D. J. (2019). Enhancing the interlayer tensile strength of 3D printed short carbon fiber reinforced PETG and PLA composites via annealing. Additive Manufacturing, 30, 100922.*

- *Bhandari, S., Lopez-Anido, R.A., Wang, L. et al. (2020). Elasto-Plastic Finite Element Modeling of Short Carbon Fiber Reinforced 3D Printed Acrylonitrile Butadiene Styrene Composites. JOM 72, 475–484.*

- *Bhandari, S.; Lopez-Anido, R.A. (2020). Discrete-Event Simulation Thermal Model for Extrusion-Based Additive Manufacturing of PLA and ABS. Materials, 13, 4985.*

ACKNOWLEDGEMENTS

I would like to thank my advisor Dr. Roberto A. Lopez-Anido for his constant support and guidance throughout the years. In addition to his expertise in structural mechanics and composite materials, his encouraging, kind, warm, and approachable nature made discussing research problems something to look forward to every week. Dr. Lopez-Anido's positive outlook towards life and kindness towards others have been the source of my inspiration. I would also like to thank my advisor Dr. Douglas J. Gardner for his guidance and support. Dr. Gardner's expert knowledge of polymers as well as his positive joyful persona inspired confidence in working with polymers. I would like to thank my committee members Dr. William G. Davids, Dr. Senthil S. Vel, and Dr. Bashir Khoda for comments, suggestions, and revisions to my research works.

I would also like to thank the faculty and staff at the Advanced Structures and Composites Center for their expertise and their kindness I have not witnessed elsewhere. I feel lucky to have worked at this place as a graduate student researcher.

I would like to give special thanks to Dr. Lu Wang for helping me with his immense knowledge and deep insights on polymers and experimental techniques.

Finally, and probably most importantly, I would like to thank my friends and my family for their constant support throughout the years. I could not have completed this undertaking without knowing that you were always at my side to support me should I falter. I am truly blessed to have you in my life.

TABLE OF CONTENTS

LIST OF TABLES

LIST OF FIGURES

CHAPTER 1
INTRODUCTION

Additive manufacturing (AM) is a transformative manufacturing technique that creates physical objects by successive deposition of material. Several additive manufacturing techniques exist and are categorized into seven major groups by ISO/ASTM 52900. The different categories of additive manufacturing are listed below [1].

1. *Binder jetting* is a process in which a liquid bonding agent is selectively deposited to join powder materials.
2. *Directed energy deposition* is a process in which focused thermal energy (e.g. laser, electron beam, plasma arc, etc.) is used to fuse materials by melting as they are being deposited.
3. *Material extrusion* is a process in which material is selectively dispensed through a nozzle or an orifice.
4. *Material jetting* is a process in which droplets of build material are selectively deposited.
5. *Powder bed fusion* is a process in which thermal energy selectively fuses regions of a powder.
6. *Sheet lamination* is a process in which sheets of material are bonded to form a part.
7. *Vat photopolymerization* is a process in which liquid photopolymer in a vat is selectively cured by light-activated polymerization.

The most common additive manufacturing method for thermoplastic polymers is extrusion-based additive manufacturing [2]. It is also commonly called FFF (fused filament fabrication) or FDM (Fused Deposition Modeling).

The process of polymer extrusion-based additive manufacturing can be divided into three major steps [3]–

1 creation of a 3D geometry of the part,

2 generation machine instructions from 3D geometry, and

3 manufacturing of part by the machine using machine instruction.

The first step involves the creation of the 3D geometry of the part using CAD modeling software or by scanning a physical object [3]. The second step is the generation of movement and extrusion path in the form of machine instructions from the 3D geometry via the process commonly called “slicing”. The STL (stereolithography) file format is the most commonly used format in additive manufacturing for representing the 3D geometry of the part to be manufactured. The STL file format stores the information about the periphery surface of the 3D geometry as a list of triangles. The triangles have stored a list of three points and a normal [4, 5]. Other newer file formats like AMF or 3DF offer advantages over the STL format by enabling storage of material or color data, by allowing definition of curved surfaces, and by reducing the file size via the use of topological description of triangles [6, 7]. However, STL still remains the most commonly used file format for 3D printing applications because of its simplicity and ease of use [8]. The STL file is read by slicing software. Based on the geometry data from the STL file and the process parameters, the slicing software generates the toolpath for the additive manufacturing equipment in the form of machine-readable instructions. Zhao and Guo reviewed different slicing and path planning algorithms [9]. Some of the different slicing algorithms used in polymer extrusion-based additive manufacturing are implicit slicing [10], uniform and variable layer thickness slicing [11, 12], unidirectional slicing and multidirectional slicing [13-15], and curved layer slicing and curved layer adaptive slicing [16, 17]. Different 2D and 3D path planning algorithms are have been used to deposit the material in the outer boundary, inner boundary, filling paths in the boundary, and paths for support [9]. Some of the several toolpath planning algorithms that have been used are

simple raycasting [18], continuous zigzag path raycasting [19, 20], Hilbert curve based toolpath [21], wavy toolpaths [22], non-retraction toolpath [23], and curved layer 3D toolpaths [24].

The process parameters are the operating parameters and the system settings that are used during the process of extrusion-based additive manufacturing. The process parameters are also commonly called printing parameters. The most commonly altered printing parameters are [25]:

- layer thickness,
- bead width,
- extrusion temperature,
- bed temperature,
- infill percentage,
- infill angle, and
- printing speed.

A comprehensive list of printing parameters used in extrusion-based additive manufacturing can be found at the websites of Cura and Simplify3D, which are commonly used slicing software for polymer extrusion-based additive manufacturing. These parameters have a significant impact on the mechanical properties as well as the part accuracy of the manufactured part [25-27]. For example, in a study by Kuznetsov et. al [28], the ultimate fracture strength of 3D printed PLA specimens in bending increased by 16% on increasing the extrusion temperature from 200 °C to 250 °C. In the same study, doubling the printing speed from 25 mm/s to 50 mm/s at 250 °C increased the ultimate fracture strength of 3D printed PLA specimens in bending by 35.0%. Wu et. al[29] observed that increasing the layer thickness from 200 µm to 300 µm increased the bending strength of PEEK specimens by 8% but further increasing the layer thickness from 300 µm to 400 µm reduced the bending strength by 13.2%. Kumar et al. [30]demonstrated a 38% increase in tensile strength of 3D printed PETG specimens by increasing the

infill percentage from 25% to 100%. Beniak et. al [31]studied the effect of extrusion temperature on the deviation of a 3D printed part from the input CAD geometry. The study found that changing the extrusion temperature from 180°C to 220°C in 3D-printed PLA reduced the deviation from CAD geometry of the part from 0.7 % to 0.4%. Akbaş et. al[32] studied the effect of extrusion temperature and speed on the deviation of strip width of a rectangular part from the input CAD geometry. The study observed that the most accurate width dimension (5% deviation in width) for ABS was observed with 240°C print temperature and 50 mm/s.

The second major step in extrusion-based additive manufacturing is the extrusion and the deposition of molten material based on machine-readable instructions. The second step of manufacturing involves supplying the feedstock material into the machine, melting the feedstock material, extruding the molten material at specified locations through a nozzle. The feedstock for small-scale 3D printers is usually in the form of filaments that are fed into the heated liquefier via feed pinch rollers [33]. However, for large-scale extrusion-based additive manufacturing machines, the feedstock is in the form of pellets. The pellets are heated and extruded in an auger and screw-based extruder [34].

Recent advances in extrusion-based additive manufacturing of thermoplastic polymers include scaling up to large scale, non-planar layers, and use of reinforcement. The build envelope of polymer extrusion-based additive manufacturing of the thermoplastic polymer ranges from a few hundred centimeters [17, 35] for small desktop 3D printers to several meters for large-scale machines [36, 37]. Short carbon fiber, short glass fiber, glass fiber, and natural fibers are the most commonly used short fiber reinforcements that have been introduced to feedstock polymer [38, 39]. Continuous reinforcement of carbon fiber [40] and glass fiber [41] has also been used in additive manufacturing of 3D printed composites. The introduction of reinforcement to the feedstock material has been shown to improve the mechanical

properties of the manufactured parts [41, 42]. The reinforcements also reduce the coefficient of thermal expansion and hence reduce the shrinkage and warping of the manufactured parted [43-45].

Advantages of polymer extrusion-based additive manufacturing include simplicity, scalability, low cost, and availability of many polymers and composites for different use cases [46, 47]. The polymer extrusion-based additive manufacturing process can be viewed as a combination of computer numerical control (CNC) technology for positioning the extrusion nozzle and thermoplastic polymer extrusion technology. Polymer extrusion is a mature technology and has been used in industry for manufacturing for a long time. As a result, polymer extrusion-based additive manufacturing can employ the technical know-how of polymer extrusion to produce parts using a wide variety of polymers and their composites. A wide variety of thermoplastic polymers and composite parts have been successfully manufactured using polymer extrusion-based additive manufacturing [7, 39, 48, 49]. Unlike most other additive manufacturing techniques, polymer extrusion additive manufacturing has been successfully applied in the production of large-scale parts [36, 50, 51].

The drawbacks of polymer extrusion-based additive manufacturing include medium manufacturing resolution, medium manufacturing speed, and low interlayer mechanical properties [46]. The manufacturing resolution is governed by the diameter of the nozzle and the height of the layer deposited. The speed of manufacture depends on several factors including the maximum extrusion rate of the extruder, thermal properties of the polymer, geometry of the part, nozzle diameter, and layer height. In general, the higher the resolution of the manufactured part, the lower the manufacturing speed.

The orthotropic nature of polymer parts manufactured using polymer extrusion-based additive manufacturing has been well documented [7, 52-55]. The orthotropy arises attributable to the

incomplete bonding between the extruded beads and the presence of voids among the deposited beads. Due to the orthotropy, the mechanics of the 3D printed parts are comparable to the mechanics of laminate structures [7, 56]. The orientation of reinforcing fibers in a laminated structure is tracked by assigning a material coordinate system to each ply in the laminated structure. Ferreira et. al [57], Bhandari et. al [55], and Somireddy et al. [54] used the material coordinate axes to define the orientation of beads in a 3D printed part. A local coordinate system, also called material axes, can be used to define the orientation of the deposited material at different locations in a 3D-printed part. Figure 1 shows the local material axes and the global machine axes for a part printed using a polymer extrusion additive manufacturing 3D printer. Axes X, Y, and Z are the global machine axes and describe the location of the manufactured part with respect to the 3D printer. The machine instructions used by the machine references the global machine axes to define the movement of the nozzle for the deposition of polymer. The local material axes 1, 2, and 3 show the relative orientation of the 3D printed material with respect to the extrusion direction. The 1-axis aligns with the direction of deposition of the material. The 2-axis is perpendicular to the 1-axis. The 3-axis is normal to the plane created by the 1-axis and the 2-axis. As shown in the Figure 1, the material coordinate axes 1,2,and 3 at points a, b and c are oriented at different angles with respect to the machine coordinates axes X, Y, and Z. E1, E2, and E3 are Young's moduli along the 1, 2, and 3-axes respectively. Similarly, S1, S2, and S3 are the strengths along the 1, 2, and 3-axes respectively.

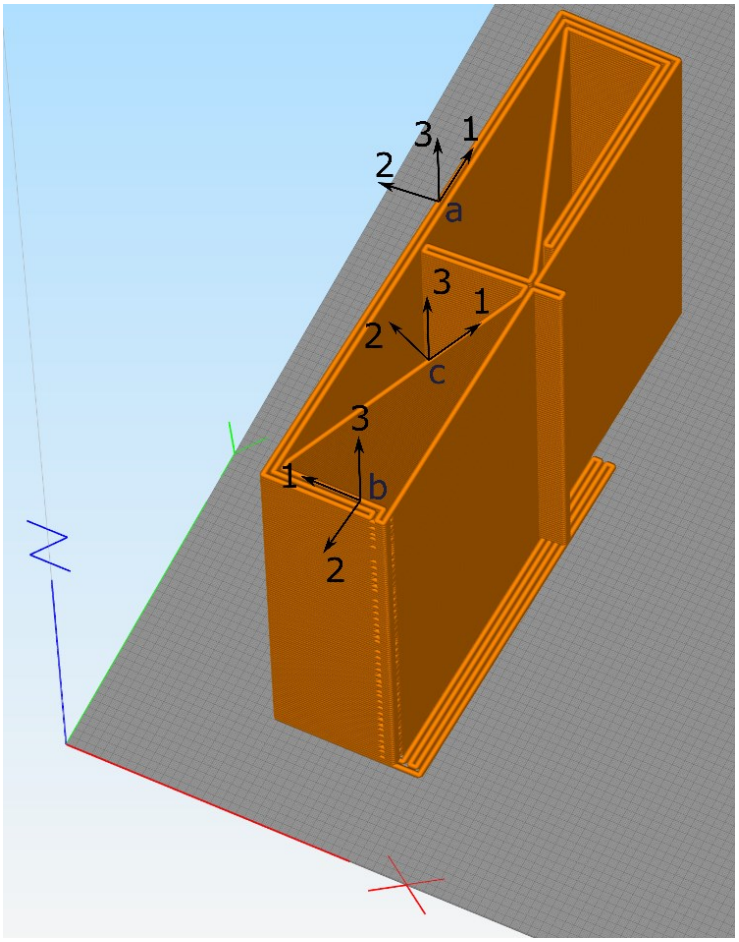

Figure 1: Material axes and machine axes in extrusion-based additive manufacturing.

Many studies have shown that the parts manufactured using polymer extrusion-based additive manufacturing have the highest mechanical properties in the 1-direction (along the direction of deposition) and the lowest mechanical properties in the 3-direction (through the thickness direction) [7, 52, 54, 58].

Chapter 1 of this dissertation introduces the polymer extrusion-based additive manufacturing process and provides a simplified overview of the manufacturing process.

Chapter 2 explores the effects of the addition of reinforcements to the polymer on the bonding mechanism and the interlayer mechanical properties of the 3D printed part. Chapter 2 also evaluates the effectiveness of annealing as a method to improve the interlayer mechanical properties.

Chapter 3 explores the use of laminate analysis for analyzing 3D printed parts. An analogy can be drawn between the polymer extrusion-based 3D printed parts and the unidirectional fiber-reinforced composites manufactured from unidirectional prepreg tapes. Both have orthotropic mechanical properties, and both are manufactured by depositing layers of material one over another. CLT (classical laminate theory) and laminate analysis are commonly used to model the mechanical behavior of unidirectional fiber-reinforced composites. Chapter 3 also explores the bimodular nature of short carbon fiber reinforced 3D printed parts and its effect on the bending behavior of polymer extrusion-based additively manufactured parts. Finite element modeling of 3D printed ABS (acrylonitrile butadiene styrene) reinforced with short carbon fibers to account for the bimodular bending behavior.

The bonding between the deposited beads and the resulting orthotropic nature of the 3D printed part is highly dependent on the process parameters and the thermal history of the part. The thermal history of the part also affects the shrinkage, the warping, and the residual stresses. Several methods have been used to simulate the thermal history of 3D printed parts using analytical models, finite difference methods, and finite element methods. The available methods either provide qualitative results or have very high computational demand. Chapter 4 introduces a new method to generate the thermal history of 3D printed parts and compares the results from the new method with the results obtained from the computationally expensive finite element method.

Chapter 5 uses the new method introduced in chapter 4 to solve a practical problem of determining a suitable extrusion rate for large-scale additive manufacturing of PLA (polylactic acid) with wood filler composite. In a layer-by-layer deposition of molten polymers, the speed of layer deposition and the extrusion temperature are of significant importance. If the layer is deposited too slowly, the bonding between the layers is inadequate resulting in lowered interlayer mechanical properties. Furthermore, the overall time required for manufacture increases, and hence the total cost of manufacture increases.

If the layer is deposited too quickly, the previous layer would not cool down enough to support the weight of the deposited layer. As a result, the layers would collapse and the manufacturing process will fail. A suitable deposition speed needs to be determined specifically for each part and for each material used. The deposition speed is currently determined via a trial and error approach. The proposed tool provides a guideline for designers to determine a suitable deposition speed and a suitable extrusion temperature.

Chapter 6 presents the conclusions of the research work and potential future work to further the research.

The objectives of the dissertation can be summarized into the following points:

1. Study how across-the-layer orthotropy is affected by the addition of carbon fibers to the polymer and how annealing affects orthotropy.

2. Model the orthotropic mechanical behavior of 3D printed parts using laminate analysis while accounting for the bimodular nature of 3D printed ABS/carbon fiber composites.

3. Develop a fast-yet-accurate numerical method to generate the thermal history of 3D printed parts and compare the results with commercially available FE model results.

4. Demonstrate the use of the numerical model to solve the practical problem of determining a suitable extrusion rate and extrusion temperature for large-scale additive manufacturing parts.

The dissertation advances the state of art by:

1) Implementing a novel approach by combining thermal, mechanical, and rheological experimental techniques to understand the effect of a filler reinforcement and thermal annealing on the mechanical properties of the additive manufacturing polymer system.

2) Presenting and experimentally validating a material model that accounts for the bimodular orthotropic elastic and elastoplastic mechanical behavior of 3D printed polymer composite parts.
3) Offering an efficient alternative to the commercially available finite element analysis-based thermal models for generating process-dependent thermal history in 3D printed polymer composites.
4) Exploring a simplified efficient numerical approach to solve a prevalent practical problem in large-format additive manufacturing to aid the manufacturing process.

CHAPTER 2
EFFECTS OF CARBON FIBER REINFORCEMENT AND ANNEALING ON INTERLAYER MECHANICAL PROPERTIES

2.1 Chapter abstract

Previous studies have shown that 3D printed composites exhibit an orthotropic nature with inherently lower interlayer mechanical properties. This research work is an attempt to improve the interlayer tensile strength of extrusion-based 3D printed composites. Annealing was identified as a suitable post-processing method and was the focus of this study. Two distinct thermoplastic polymers, which are common in 3D printing, were selected to study the enhancement of interlayer tensile strength of composites by additive manufacturing: a) an amorphous polyethylene terephthalate-glycol (PETG), and b) a semi-crystalline poly (lactic acid) (PLA). It was determined that short carbon fiber reinforced composites have lower interlayer tensile strength than the corresponding neat polymers in 3D printed parts. This reduction in mechanical performance was attributable to an increase in melt viscosity and the consequential slower interlayer diffusion bonding. However, the reduction in interlayer tensile strength could be recovered by post-processing when the annealing temperature was higher than the glass transition temperature of the amorphous polymer. In the case of the semi-crystalline polymer, the recovery of the interlayer tensile strength was only observed when the annealing temperature was higher than the glass transition temperature but lower than the cold-crystallization temperature. This study utilized rheological and thermal analysis of 3D printed composites to provide a better understanding of the interlayer strength response and, therefore, overcome a mechanical performance limitation of these materials.[1]

---

[1] The research work presented in this chapter has been published as:
Bhandari, S., Lopez-Anido, R. A., & Gardner, D. J. (2019). Enhancing the interlayer tensile strength of 3D printed short carbon fiber reinforced PETG and PLA composites via annealing. Additive Manufacturing, 30, 100922. Doi: https://www.doi.org/10.1016/j.addma.2019.100922.

2.2 Introduction

Material extrusion-based additive manufacturing operates by extruding beads of molten thermoplastic composite layer by layer to manufacture a part. . Zaldivar et al. [59] studied the effect of printing orientation on 3D printed ULTEM 9085 parts and found that the interlayer tensile strength (S3) was lower compared to the tensile strength along with the deposition (S1). Torrado and Roberson [52] showed that the interlayer tensile strength (S3) and Young's modulus (E3) are significantly lower compared to the tensile strength (S1) and Young's modulus (E1) along the bead deposition direction. Caminero et al. [58] showed that interlayer bonding decreases with an increase in layer thickness for unreinforced nylon 3D printed parts. Zhang et al. [60] also reported lower strength (S2) in the direction perpendicular to bead deposition compared to strength (S1) in the direction along the direction of bead deposition.

The addition of carbon fiber as a reinforcement increases the mechanical properties along the 1-axis [61]. Studies have shown that the mechanical properties, along the 2-axis, remain largely unchanged or are reduced by the addition of carbon fibers. Jiang and Smith [62] studied the effect of carbon fiber reinforcement on the strength of 3D printed polymers. Their study showed that while the addition of carbon fiber increased the tensile strength along the 1-axis, tensile strength along the 2-axis was unaffected or reduced. Hwang et al. [63] studied the thermomechanical properties of ABS-copper particle 3D printed parts. The study found that by increasing the weight fraction of copper particles from 10 % to 30 %, the tensile strength along the 2-axis decreased significantly. The authors stated that the decrease in the tensile strength was attributable to the corresponding increase in voids and the increased disturbance in bonding between the layers by the copper particles.

The mechanical properties along the 3-axis, however, are significantly decreased with the addition of carbon fiber to the 3D printed polymer [45, 60]. Zhang et al. [60] studied the interfacial bonding strength

of 3D printed acrylonitrile butadiene styrene (ABS) parts reinforced with short carbon fibers. The study showed that the interlayer shear strength (S12) of the short carbon fiber (CF) reinforced ABS parts were reduced in strength compared to those of the unreinforced ABS parts. Similarly, Love et al. [45]reported a significant decrease in interlayer tensile strength (S3) of CF reinforced ABS parts compared to unreinforced ABS parts. Duty et al. [64] discussed the mechanical anisotropy in extrusion-based additive manufacturing and compared reduction in ultimate tensile strength in the Z-direction for different 3D printed reinforced and unreinforced polymers.

The interlayer mechanical properties are governed by the diffusion bonding of polymer across the interface. The reptation model developed by de-Gennes [65] helps explain the diffusion bonding of polymeric materials across the 3D printed layer interface. Kim and Lee [66] presented the motion of chains across the interface with five distinct stages of surface rearrangement, surface approach, wetting, diffusion, and randomization. Lee and Springer [67] reorganized the diffusion bonding process of polymer interfaces into two simple steps, intimate contact, and autohesion. Sun et al. [68] extended the concept of intimate contact and autohesion to the bonding of bead deposition in extrusion-based 3D printed polymer parts. Their study, as shown in Figure 2, identified three different stages in the bond formation between deposited filament beads, a) surface contacting, b) neck growth and c) molecular diffusion at interface and randomization. Surface contacting occurs when a new bead is extruded and deposited next to another bead. As the beads are in a molten state, the viscous flow of the polymer causes neck formation. Molecular diffusion at the interface and randomization is well explained by reptation theory and the time required for diffusion and randomization is approximated by the reptation time of the polymer chain. Coogan and Kazmer [69] predicted the bond strength based on the diffusion-controlled healing model.

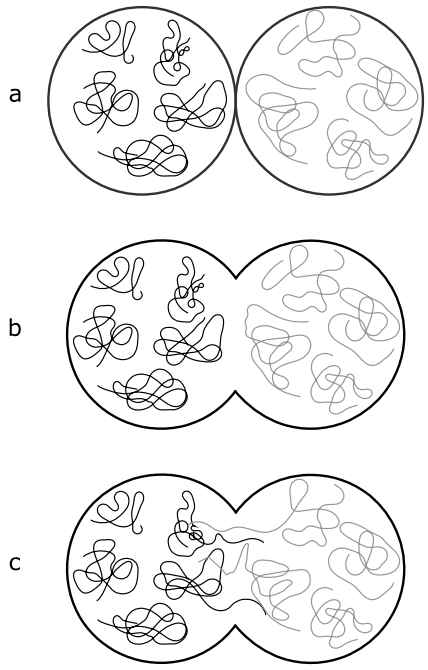

Figure 2: Three stages in bond formation between filaments a) surface contact, b) neck growth and c) molecular diffusion at interface and randomization described by Sun et al. [18].

When 3D printed parts are used in load-bearing structures, reduced interlayer strength causes performance problems. Delamination of layers causes the 3D printed parts to fail at significantly lower stress compared to an injection molded part. Different methods have been used to increase the interlayer mechanical properties. Chesser et al. [70] used post-tensioning of large-scale 3D printed parts for load-bearing structures. Yerazunis et al. [71] used stress tensor alignment techniques and five-axis printing to strengthen a polymer extrusion-based 3D printed part. Sweeney et al. [72] used microwave irradiation of carbon nanotubes for localized heating to weld interfaces between thermoplastic interfaces. Ravi et al. [73] used a local laser-based pre-deposition heating to increase interlayer interface temperature during extrusion-based 3D printing. Deshpande et al. [74] optimized the laser-based pre-deposition heating process to improve the interlayer strength even further. Kishore et al. [50] used infrared preheating to improve the interlayer strength of big area additive manufacturing components

made from CF reinforced ABS polymer. Faes et al. [75] found that slowing down interlayer cooling increases the tensile strength in the 3-direction. Pan et al. [28] studied the effects of layer thickness and nozzle speed on interlayer strength of PLA 3D printed parts.

Annealing is also effective for improving the mechanical properties of a 3D printed part along the direction of deposition. Annealing is the process of heating a polymer part to a specified temperature, holding the temperature for a specified time, and slowly cooling the part to room temperature. The annealing process has been used on polymers to increase the crystallinity of semi-crystalline polymers [76-80]. Annealing of 3D printed polymer parts has been used to release residual thermal stresses [79, 81, 82]. Residual thermal stresses reduce the effective interlayer mechanical properties of 3D printed parts and are inevitably present in 3D printed parts [82-85]. Annealing reduces such stresses by allowing the viscoelastic relaxation of the polymer.

Wootthikanokkhan et al. annealed injection molded PLA/Kenaf-fiber composites at 100 °C and found that tensile strength was unchanged while heat deflection temperature increased. Torres et al. studied the effect of annealing on 3D printed PLA composites and found that heat treatment at 100 °C for 30 min increased the interlayer shear strength of the part. Ivey et al. studied the effects of heat treatment at 30 °C, 60 °C, and 90 °C above glass transition temperature on CF reinforced PLA 3D printed part with alternating 0°/90° infill. The study found that heat treatment did not have any significant effect on the mechanical properties of the 3D printed part. The authors stated that better consolidation of the part was achieved but further investigation was required to understand the significance of this effect. Wang et al. found that the effective annealing via printer bed heating of a 3D printed PLA part increased its crystallinity and impact strength. Hart et al. found that fracture toughness of 3D printed amorphous thermoplastics can be increased significantly via thermal annealing as a result of sintering and reptation between inter-laminar layers. The study also found that the inter-laminar fracture

toughness was governed by the reptation time of the polymer. The interlaminar fracture toughness was also governed by the time required for the polymer to flow and make intimate contact during the annealing process.

Prior studies provide some insight into the effect of annealing on the mechanical properties of 3D printed polymers. Post-tensioning is usually carried out on large-scale 3D printed parts with short-term use. Loss of prestress due to relaxation of 3D printed polymer and complexity of the prestressing process would make post-tensioning unsuitable for smaller 3D printed parts. Z-pinning disrupts the continuity of filament deposition which leads to slower printing time and requires a more intricate setup for placing the pins. Stress tensor alignment techniques use 5-axis 3D printing which is not very common in extrusion-based 3D printing and is slower compared to the 3-axis 3D printing process. The microwave heating technique requires the introduction of microwave-sensitive particles at the interface to heat the interface and induce diffusion bonding. Laser local pre-deposition heating (LLPH) and infrared heating require modification of existing 3D printers to include heaters. Interlayer cooling time reduction is an effective technique but is limited by the complexity of geometry and infill of the 3D printed part. Annealing does not any require modification of the 3D printer or the 3D printing process and can be used in addition to other processes discussed to further enhance the interlayer tensile strength of the 3D printed part.

Further investigation is needed on the effects of annealing on interlayer mechanical properties of 3D printed composites of amorphous and semi-crystalline polymers. Prior studies did not consider the effects of annealing on the interlayer strength of CF reinforced semi-crystalline and amorphous polymers. The objective of this study is to explore the effects of annealing on interlayer mechanical properties of 3D printed carbon fiber reinforced polymers.

2.3 Materials and methods

2.3.1 Materials

Polyethylene terephthalate with glycol copolymer (PETG) and poly (lactic acid) (PLA) were selected for the study. These are commonly used 3D printing materials representing different degrees of crystallinity. PETG is known to be an amorphous polymer while PLA is known to be semi-crystalline. The two polymers were selected to study the effect of annealing on amorphous and semi-crystalline polymers. Neat and carbon fiber-filled filaments of PETG and PLA were used to study the effect of reinforcement on interlayer strength and the effect of subsequent annealing.

Two carbon fiber reinforced polymers materials were used for the study. Two neat polymer materials were used for comparison. The polymer filaments used for the study are listed below:

i) MAX-G PETG filament from 3DXTECH

ii) CARBONX CFR-PETG filament from 3DXTECH with 20 % by weight fiber reinforcement

iii) ECOMAX PLA filament from 3DXTECH

iv) CARBONX CFR-PLA filament from 3DXTECH with 20 % by weight fiber reinforcement

2.3.2 Material characterization tests

2.3.2.1 Fiber length distribution measurement

Fiber length distribution was measured to characterize the reinforcement fiber in the 3D printing filament. Previous research has shown that the length of the fiber reinforcement affects the mechanical properties as well as the viscosity of the molten polymer.

Approximately 2 g of reinforced polymer filament was dissolved in N, N-dimethylformamide by heating at 70 °C for 30 min. N, N-dimethylformamide was supplied by Sigma-Aldrich. The mixture was filtered through a standard filter paper. The residue on the filter paper was spread over conductive carbon tape

and observed under a Hitachi TM3000 scanning electron microscope. Micrographs were taken at x200 magnification. ImageJ software was used to measure the length of the fibers in the micrographs. Fibers that were at the edge of the micrograph and had only one end in the micrograph were not measured. Fibers that had both ends within the micrograph were measured. All such fibers in each image were measured. A new image was analyzed if the total number of fiber lengths measured was less than 1000. Figure 3a is the micrograph of the carbon fibers seen at 200x magnification. Figure 3b highlights the fibers that were measured for the fiber length analysis.

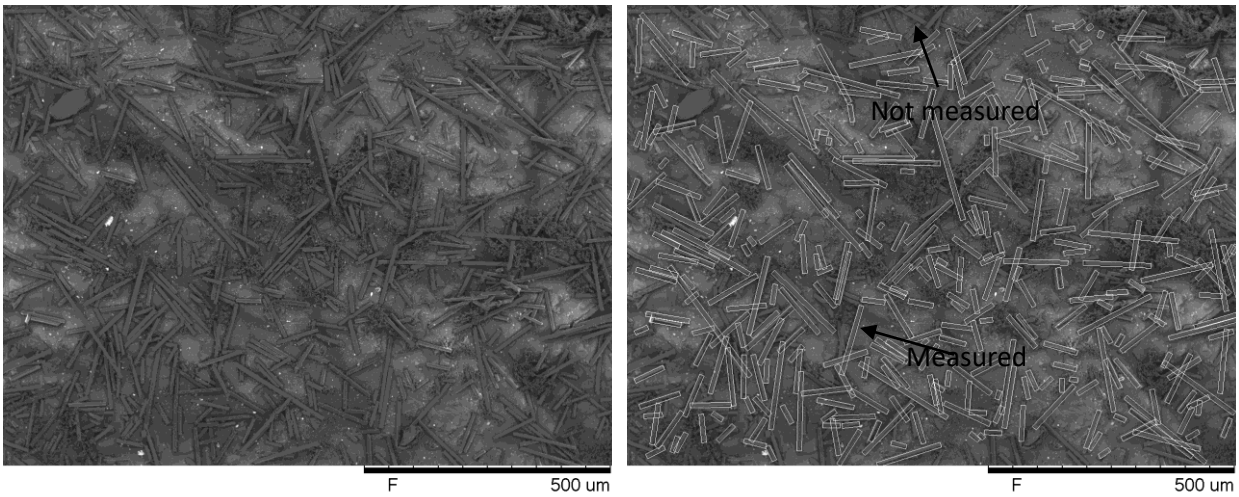

a) Micrograph(x200) showing carbon fibers. b) Micrograph highlighting measured fibers.

Figure 3: Micrographs showing fibers that were considered for fiber length distribution analysis.

2.3.2.2 Dynamic mechanical analysis (DMA)

DMA was carried out to measure the glass transition temperature of the polymers. The purpose of this test was to determine a suitable annealing temperature for the 3D printed specimens. The annealing temperature was higher than the glass transition temperature but low enough so that the material did not deform significantly under its own weight during annealing. A Dynamic Mechanical Analyzer Q800 from TA Instrument was used for performing measurements. The glass transition temperature was determined using DMA per ASTM E1640-18[47]. Three rectangular specimens with dimensions 40mm (L)

x 13mm (W) x 1.3mm (H) were prepared for tensile loading. The specimens were loaded at a frequency of 1 Hz. The amplitude of loading was set to 15 N. The specimens were equilibrated at 30 °C for 5 minutes and then ramped up at 1 °C per minute up to 130 °C for PETG specimens and up to 125 °C for PLA specimens. The storage modulus was plotted for the temperature range considered. The region of storage modulus curve below the transition temperature and the region after the transition was identified. The temperature where these tangent lines to these regions intersect was reported as the glass transition temperature as per ASTM E1640-18. Loss modulus and tan delta were also measured to identify the regions where the polymer begins to show a fluid-like behavior.

2.3.2.3 Viscosity Measurements

Viscosity measurements were carried out to determine the viscosity difference in reinforced and unreinforced polymers at their extrusion temperature. Past research works have shown that the interlayer tensile strength depends on initial contact and neck growth during the deposition process [86-89]. The neck growth and reptation process are dependent on the viscosity of the polymer specimen. Hence viscosity of polymer at extrusion temperature would be useful in understanding the interlayer mechanical properties of the 3D printed polymer.

The viscosity of the melt was measured through parallel-plate rotational rheometry using a Bohlin Gemini Rheometer. A 25mm diameter parallel plate set was used. The specimen was placed in between the parallel plates and heated up to a specified temperature. PETG and PETG-CF were heated up to a temperature of 270 °C. PLA and PLA-CF specimens were heated up to a temperature of 230 °C. A gap of 1 mm was specified. Any excess material that oozed out of the plates was removed by opening the heating chamber and scraping using a metal spatula. The specimen was heated again to the set temperature and the temperature was held for 1 minute. The temperature was reduced at a rate of 5 °C per minute until it reached the lower set temperature.

A temperature window of 40 °C was selected so that the trend of viscosity on lowering temperature could be established. The temperature range was 220 °C to 180 °C for PLA and PLA-CF specimens. The temperature range was 260 °C to 220 °C for PETG and PETG-CF specimens. For both polymers, the temperature range was selected such that viscosities 10 °C above and 30 °C below the extrusion temperature could be measured. Steady state shear with 1 s^{-1} was used. Based on previous research works, PLA shows Newtonian behavior and PETG shows slightly non-Newtonian behavior at the test temperature ranges.

2.3.3 Additive manufacturing of test specimens

A Prussa i3 MK2 open-source printer was used to manufacture the test specimens. Figure 4 shows the process of making tensile test specimens. Hollow boxes, 90mm (L) x 90mm (B) x 190 mm (H), with a wall thickness of 3.20 mm were printed using the printing parameters listed in Table 1.

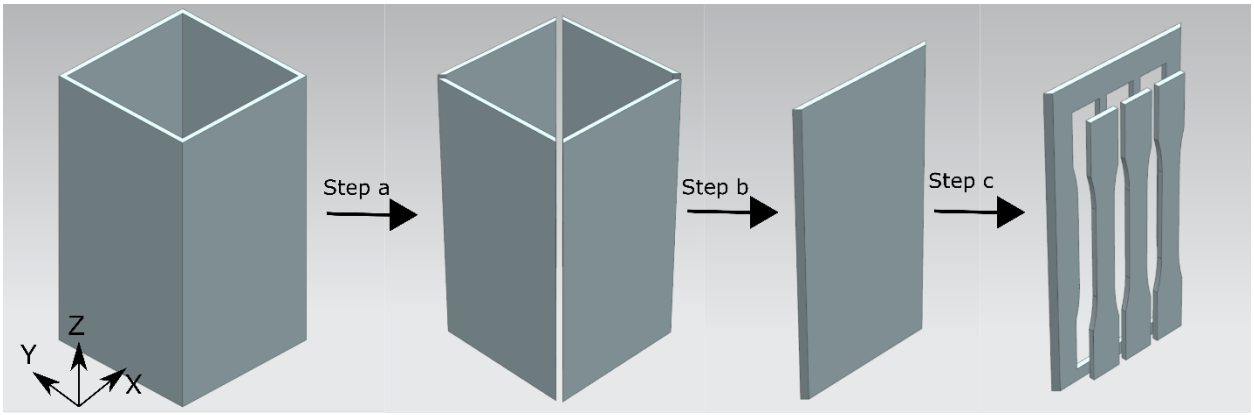

Figure 4: Process of making ASTM D638 dog-bone specimens from a 3D printed box.

The four walls were machined using a vertical band saw (Step a). The walls were separated and secured on the bed of a waterjet cutting machine (Step b). Three ASTM D638 type I dog-bone specimens were prepared from each of the walls using a waterjet cutter (Step c). This particular approach of making tensile coupons was chosen because the tension coupons themselves are thin and slender and could not

be printed upright. Another benefit of using this approach is that the effect of bed heating can be minimized as the specimen is prepared at a distance from the base region.

Figure 5 shows the dimensions and print orientation of tensile test specimens. The 3-axis of the material axis aligns with the Z-axis of the printer.

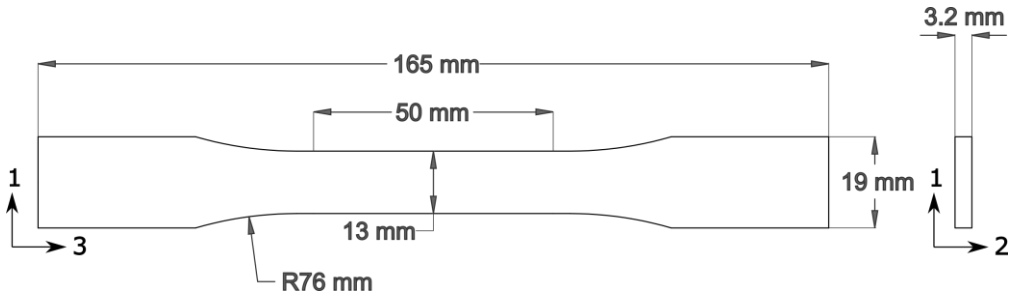

Figure 5: Tensile specimen with dimensions and print orientation [90].

Table 1: Printing parameters for the 3D printed specimens.

Parameter	Value
Nozzle Diameter	0.8 mm
Retraction distance	1.5 mm
Retraction speed	60 mm/s
Layer height	0.36 mm
Outline perimeters/shells	2
Top/ bottom solid layers	0
Infill	None
Extruder Temperature	250 °C (PETG and PETG-CF) 210 °C (PLA and PLA-CF)
Bed Temperature	90 °C (PETG and PETG-CF) 55 °C (PLA and PLA-CF)
Printing speed	30 mm/s

Printing speed for first layer	15 mm/s
Movement speed	60 mm/s
Layer cooling fan	Off

2.3.4 Scanning electron microscopy of test specimens

A Hitachi TM3000 scanning electron microscope was used to obtain micrographs of waterjet cut surfaces of the 3D printed specimens. The micrographs were used to ascertain the state of neck formation and reptation of the specimens as printed. Hart et. al[87] suggested that viscosity at melt during extrusion affects the neck formation. The micrographs would help to observe if the neck formation process of the specimens was affected by the change in viscosity due to the addition of carbon fibers.

2.3.5 Annealing of test specimens

A total of 110 tensile test specimens were manufactured. These specimens were divided into 22 sets of test groups with 5 specimens in each group. Each set was subjected to a different annealing time and temperature. The time and temperature the specimens were subjected to are listed in

Table 2.

Table 2: Sets of specimens of different materials and annealing times.

Set	Material	Annealing Temperature (°C)	Annealing Time (minutes)
1, 2, 3, 4	PETG	120	0, 30, 240,480
5, 6, 7, 8	PETG-CF	120	0, 30, 240, 480
9, 10, 11, 12	PLA	120	0, 30, 240, 480
13, 14, 15, 16	PLA-CF	120	0, 30, 240, 480

17, 18, 19	PLA	90	30, 240, 480
20, 21, 22	PLA-CF	90	30, 240, 480

The annealing temperature of 120 °C was chosen for PETG because it was considered reasonably high above the glass transition temperature of PETG as measured using DMA. The storage modulus decreased by three orders of magnitude at this temperature. This annealing temperature was considered suitable as the specimens had enough stiffness to avoid deforming under their own weight.

Two annealing temperatures of 90 °C and 120 °C were chosen for annealing PLA and PLA-CF parts. The cold crystallization temperature of PLA began at 110 °C and peaked at 120 °C. Two temperatures were used to compare the effect of cold crystallization during the annealing of PLA and PLA-CF parts.

A Fischer Scientific oven (Isotemp programmable forced draft furnace model 750-126) was heated to the annealing temperature. The specimens were laid upon a flat steel plate and put in an oven for times listed in

Table 2. After holding the temperature for mentioned times, the specimens were brought out of the oven to room temperature and allowed to cool. The final crystallinity of the annealed specimens is affected by the rate of cooling. A slower cooling rate leads to higher crystallinity in the final specimen and a faster cooling rate leads to lower crystallinity. However, in this research work, the specimens were left at room temperature to cool down.

2.3.6 Differential scanning calorimetry (DSC) of test specimens

DSC was carried out to determine the change in crystallinity of 3D printed specimens before and after the annealing process. Past research works have shown that the annealing process changes the

crystallinity of semi-crystalline polymers, and crystallinity affects the mechanical properties of the 3D printed polymers.

DSC was carried out using a TA Q2000 calorimeter. The crystallinity of the unannealed specimens and the specimens annealed for 8 hours at 120 °C was calculated. Approximately 5 mg samples were cut from the 3D printed specimens and heated from 40 °C to 210 °C at the rate of 10 °C per minute. Only one heating cycle was performed and the crystallinity calculation was based on the DSC thermographs of the first heating cycle. Nitrogen was used for all measurements to prevent polymer degradation. Three replicates were tested to ensure repeatability. Equation 2.1 was used to calculate the crystallinity of the specimens .

$$X_c = \frac{\Delta H_m - \Delta H_{cc} - \Delta H_r}{f\ \Delta H_f} \qquad (2.1)$$

where,

X_c	=	Crystallinity
ΔH_m	=	Enthalpy of melting
ΔH_{cc}	=	Enthalpy of cold crystallization
ΔH_r	=	Enthalpy of reordering of polymer chains
ΔH_f	=	Enthalpy of melting of 100% crystalline PLA (93.7 J/g) [91]
f	=	The weight fraction of PLA polymer

2.3.7 Tensile tests

An Instron 7700 servo-electric testing frame was used for tensile tests of the annealed specimens. The procedure outlined in ASTM D638-14[90] was followed during the testing. A loading rate of 5 mm/min of crosshead displacement was chosen. A 10 kN (2.2 kip) Instron load cell, with an uncertainty of 0.262 N (0.059 lb) at a full-scale load of 200 N, was used for the measurement of tensile force. An Instron extensometer (model no 2630-112) with 50.8 mm (2.00 in) gauge length with an accuracy of 0.001 mm was used to measure the displacement in the gage area.

2.4 Results and discussion

2.4.1 Fiber length distribution

Figure 6 shows the fiber length distribution of reinforcing short carbon fibers in PETG-CF and PLA-CF filaments used for this study. The average length of carbon fibers reinforcing PETG-CF filaments was 75.6 µm. The average length of carbon fibers reinforcing PLA-CF filaments was 67.0 µm.

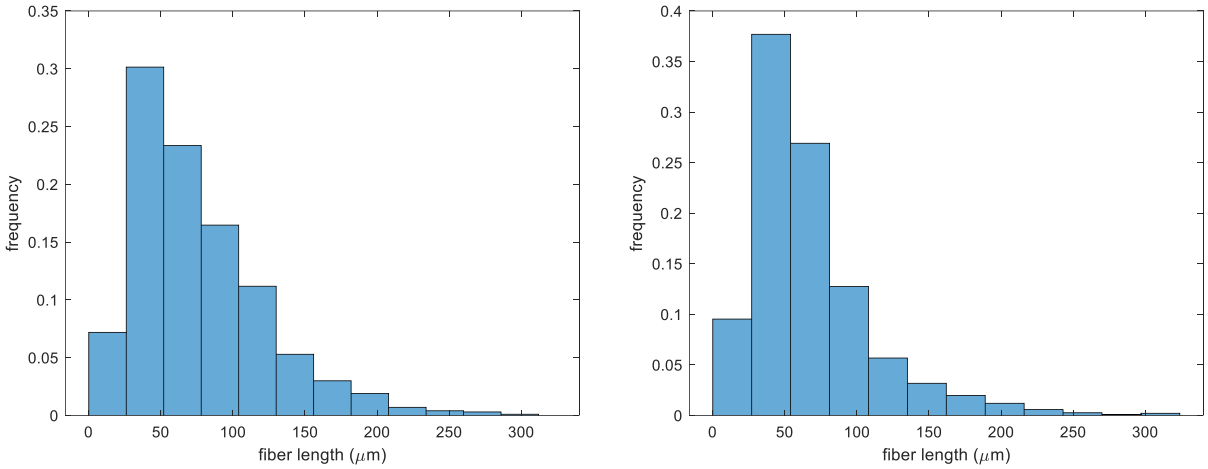

a) PETG-CF b) PLA-CF

Figure 6: Fiber length distribution of reinforcing carbon fibers in PETG-CF and PLA-CF filaments.

2.4.2 DMA results

Figure 7 shows the storage modulus vs temperature curve for PETG polymer measured using DMA. The curve shows the typical behavior of an amorphous thermoplastic polymer with a rapid decline in storage modulus after the glass transition temperature. Glass transition temperature for the PETG polymer used for this study was 80.7 °C based on the storage modulus curve. Glass transition temperature, based on the peak of tan(δ) curve, was 90.2 °C. The glass transition temperature obtained from the tan(δ) curve is close to the glass transition temperature obtained from the DSC. Glass transition temperature based on loss modulus was 82.7 °C.

Figure 7 also shows the storage modulus vs temperature curve for PLA polymer measured using DMA. The curve shows the typical behavior of a semi-crystalline thermoplastic polymer with a low degree of crystallinity marked by a rapid decline in storage modulus after the glass transition temperature. Glass transition temperature, based on storage modulus curve, was 56.3 °C for PLA polymer used for this study. Glass transition temperature, based on the peak of the tan(δ) curve, was 64.3 °C. This value of glass transition temperature is close to the value obtained from DSC. Glass transition temperature, based on loss modulus, was 57.9 °C. Cold crystallization raises the storage modulus of the polymer from 90 °C to 105 °C.

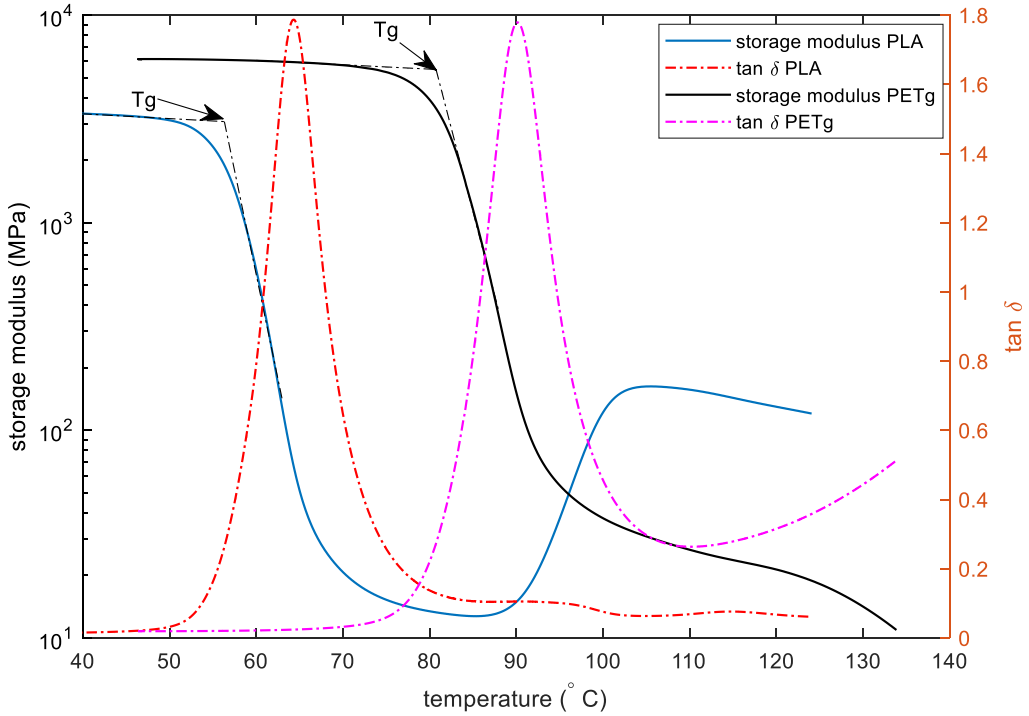

Figure 7: Storage modulus and tan δ vs temperature for PETG polymer and PLA polymers.

2.4.3 Viscosity measurement results

Figure 8 shows the viscosity of PETG and carbon fiber reinforced PETG polymers at temperatures near the extrusion temperatures used for this study. The addition of carbon fibers has significantly increased the viscosity of PETG polymer.

Similarly, the viscosity of PLA and carbon fiber reinforced PLA at temperatures near the extrusion temperature is also shown. The addition of carbon fiber increases the viscosity of PLA polymer at melt.

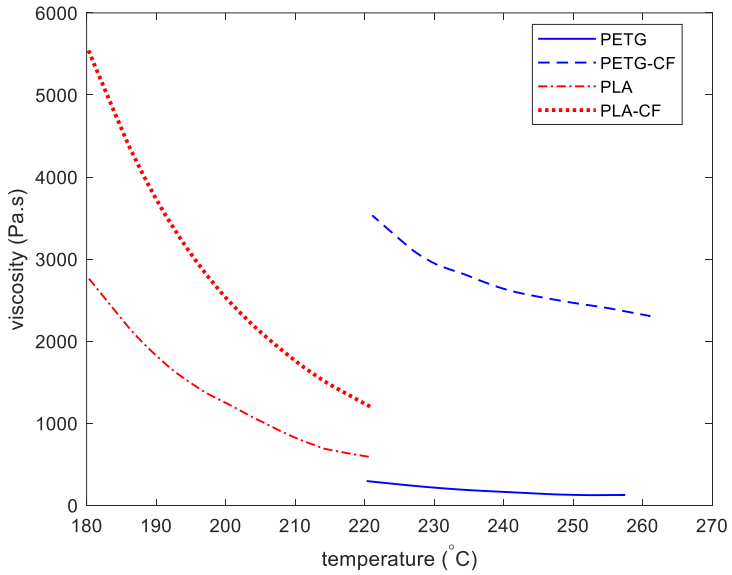

Figure 8: Viscosity of PETG, CF reinforced PETG, PLA, and CF reinforced PLA near their respective extrusion temperatures.

2.4.4 SEM micrographs

Figure 9 shows the cross-section of waterjet cut surfaces of different 3D printed polymers. Comparing Figure 9a and Figure 9b, interlayer diffusion in PETG looks better with less void between the layers. Comparing Figure 9c and Figure 9d, the interlayer bond-line in PLA looks well-diffused compared to PLA-CF. In general, the neat polymers show better bonding across the interface compared to their carbon fiber reinforced counterparts.

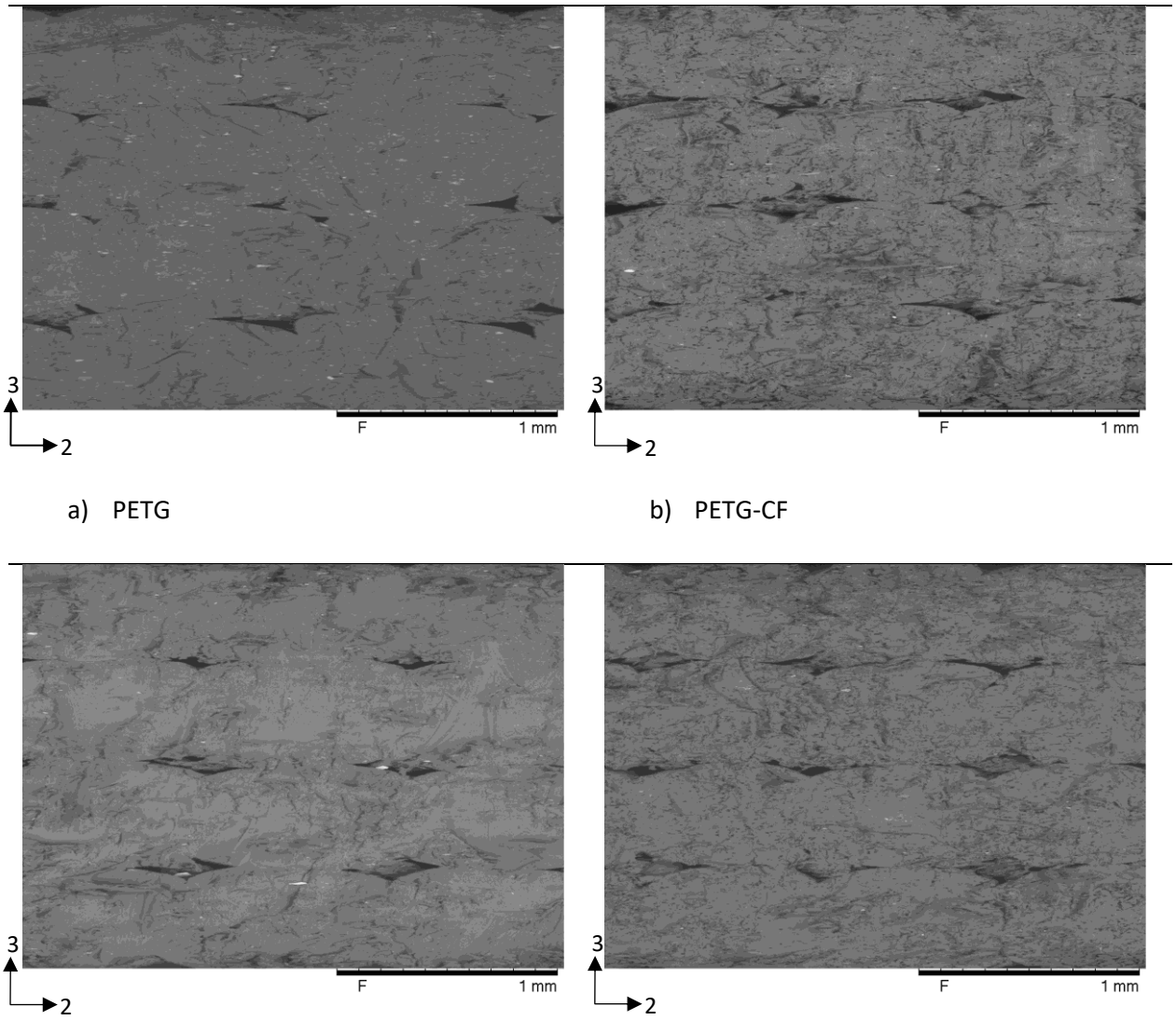

a) PETG b) PETG-CF

c) PLA d) PLA-CF

Figure 9: Waterjet cut section of unannealed specimens magnified 100x.

2.4.5 DSC results

Figure 10 shows the DSC curves for PETG specimens that underwent annealing for 8 hours and the specimens that remained unannealed. The rapid fall in heat flow at around 80 °C in the DSC curves, marks the glass transition for unannealed and annealed PETG and PETG-CF specimens. Peaks indicating

melting or other phase transitions were not observed for PETG and PETG-CF in the temperature range scanned in the DSC experiments.

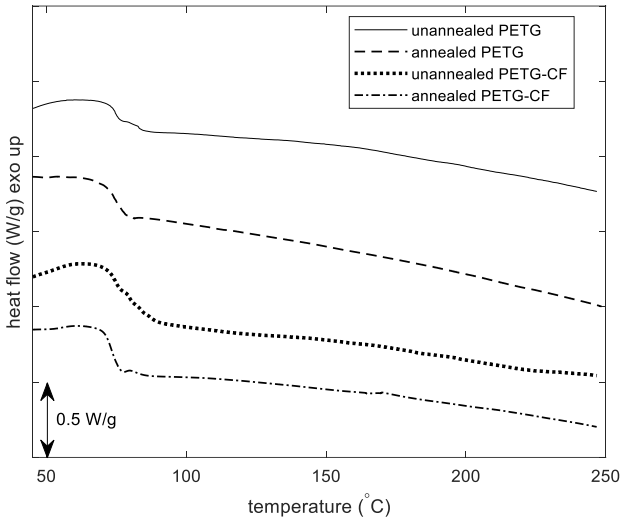

Figure 10: DSC curves of 3D printed unannealed and 8-hours annealed PETG and PETG-CF specimens.

Figure 11 shows the DSC curves for PLA specimens that underwent annealing for 8 hours and the specimens that remained unannealed. The unannealed specimens have a cold crystallization peak at 120°C. The annealed samples have the peak suppressed. Wach et al. observed similar suppression of cold crystallization peak when annealing neat PLA at 85 °C and 90 °C. The suppressed peak suggests that the annealed specimens are crystallized. The unannealed PLA specimens had a crystallinity of 4.23% whereas the PLA specimens annealed at 120 °C had a crystallinity of 29.7%. The PLA specimens annealed at 90 °C had a crystallinity of 20.0%. The specimens showed a peak around 65 °C, which marks the glass transition temperature of PLA. The glass transition temperature of PLA shifted to a slightly higher temperature after annealing. The change has been mainly attributed to the limitation of chain mobility within the polymer matrix. The presence of crystals in the polymer matrix acts as physical cross-linking sites to restrict polymer chain motion and increases glass transition temperature [93-95]. A transition was observed for annealed PLA samples before the melting peak. Similar transitions were

observed by Tábi et al for PLA annealed at 110 °C for 1 hour [96, 97]. Tábi et al. attributed this to the transition of disordered α' to ordered α crystals. This change in PLA crystals could explain the transition observed for PLA annealed at 90 °C for 8 hours. However, for PLA annealed at 120 °C for 8 hours, the peak shifts to a significantly lower temperature. Further study is necessary to understand the presence of this peak. The specimens showed another peak at around 150 °C, which marks the melting point of PLA.

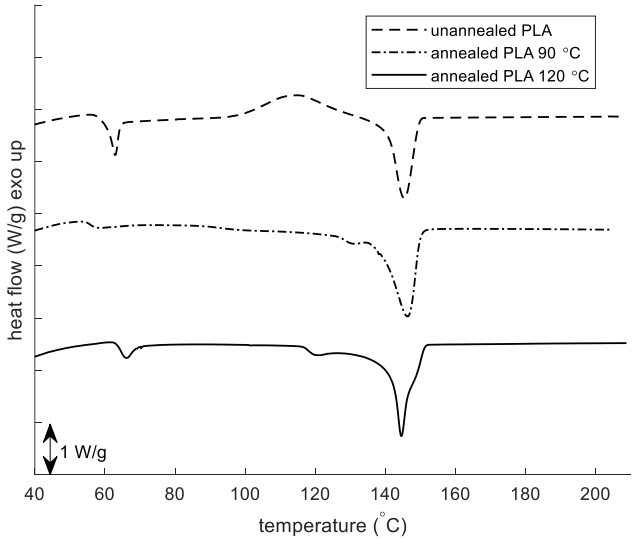

Figure 11: DSC curves of 3D printed PLA specimens unannealed and annealed for 8 hours.

Figure 12 shows the DSC curves for PLA and PLA-CF specimens that underwent annealing for 8 hours and the specimens that remained unannealed. The unannealed specimens have a cold crystallization peak at 120 °C. The specimens annealed at 90 °C have a lower and narrower cold crystallization peak. This suggests that the specimens annealed at 90 °C have partially crystallized. Similarly, the unannealed PLA-CF specimens had a crystallinity of 3.92% whereas the PLA-CF specimens annealed at 120 °C had a crystallinity of 30.2%. This suggests that the addition of carbon fiber slows down the crystallization of PLA while annealing below the cold crystallization temperature of PLA. This phenomenon was also observed by Ivey et al. when they annealed PLA-CF at 85 °C. Liu et al. found that carbon fibers act as a

nucleating agent and increase the rate of crystallization. Studies for annealing PLA-CF at 120 °C and low carbon fiber content (2%wt) show that carbon fibers act as nucleating sites and increase the rate of crystallization. However, in our research work, with high carbon fiber content and lower annealing temperature (90 °C), we found lower crystallinity in PLA-CF compared to neat PLA. Further investigation is required to understand the mechanisms that affect the crystallization of PLA-CF at temperatures lower than cold crystallization temperatures. The PLA-CF specimens annealed at 90 °C had a crystallinity of 10.2%. The specimens showed a peak around 65 °C that marks the glass transition temperature of PLA. Other studies that used PLA reinforced with other fibers showed a similar reduction in crystallinity with a greater weight ratio of reinforcing fibers. Fazita et. al[98] found that bamboo fibers (35% wt.) reinforcing PLA reduced the crystallinity of composite. The reduction in crystallinity was attributed to the limitation in crystalline growth due to the presence of scattered fibers and the subsequent hampering of the mobility of the long polymer chains. Similarly, Kurniawan[99] reported a decrease in crystallinity of PLA/ silane treated basalt fiber composite (35% wt.) whereas an increase in crystallinity of PLA/basalt fiber composite compared to pure PLA. Further investigation is needed to study the effects of carbon fiber reinforcement at high weight percentage and low annealing temperature.

Another significant peak was observed at 150 °C that marks the melting point for PLA.

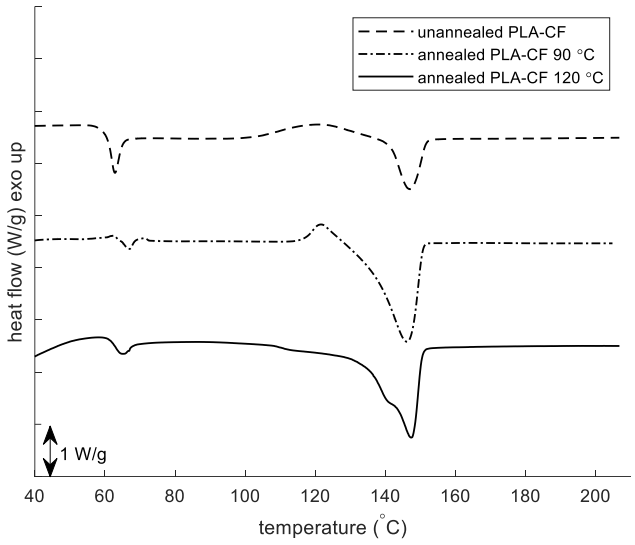

Figure 12: DSC curves of 3D printed PLA-CF specimens unannealed and annealed for 8 hours.

The crystallinity of unannealed and annealed PLA and PLA-CF specimens are listed in Table 3.

Table 3: Crystallinity of 3D printed specimens for different annealing conditions.

Polymer and processing condition	**PLA, No annealing**	**PLA-CF, No annealing**	**PLA, 90 °C, 8 hours**	**PLA-CF, 90 °C, 8 hours**	**PLA, 120 °C, 8 hours**	**PLA-CF, 120 °C, 8 hours**
Crystallinity	4.23%	3.92%	20.0%	10.2%	29.7%	30.2%

2.4.6 Tension test results

Figure 13 shows the interlayer tensile strength of 3D printed neat and reinforced PETG and PLA polymer specimens. The interlayer tensile strength of neat PETG 3D printed specimens without annealing was 36.7 MPa. Annealing did not significantly change the interlayer tensile strengths of PETG 3D printed specimens with mean interlayer tensile strength for PETG specimens annealed at 120 °C for 30 minutes, 240 minutes, and 480 minutes to be 36.2 MPa, 36.8 MPa, and 34.6 MPa respectively.

Previous research work has shown that 3D printed neat PETG shows low anisotropy compared to other polymers like ABS and PLA as discussed in the introduction section. Jiang et al. showed that the in-plane strengths of 3D printed neat PETG specimens at different orientations are comparable. The addition of carbon fibers increases the anisotropy significantly. 3D printed PETG specimens from Jiang et. al [62] paper had an in-plane tensile strength close to 45 MPa at all orientations. Although Jiang et. al used different printing parameters and measured in-plane properties, the tensile strength of 36.2 MPa observed in this research work is comparable. Annealing at higher temperatures might increase reduce the voids and increase the interlayer bonding. However, the specimen would show significant deformation under its own weight when subjected to higher temperatures.

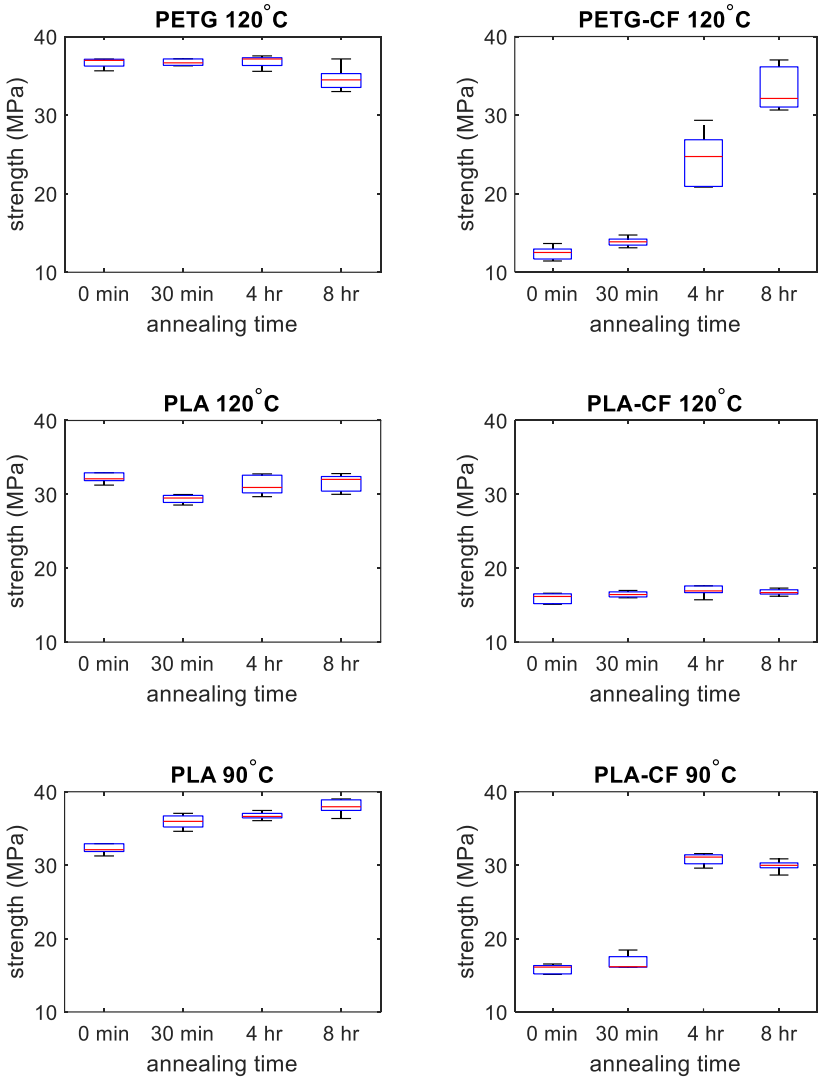

Figure 13: Interlayer tensile strength of 3D printed neat and reinforced PETG and PLA polymer specimens subjected to annealing.

The interlayer tensile strength decreased significantly with the addition of carbon fiber reinforcement to the PETG polymer. The mean interlayer tensile strength of unannealed PETG CF specimens was reduced to 12.4 MPa. Annealing the PETG-CF specimens for 30 minutes increased the strength slightly to 13.8 MPa (37 % of neat unannealed PETG strength). However, annealing the specimens for 240 minutes and 480 minutes increased the strength to 24.4 MPa (67% of neat unannealed PETG strength) and 32.4 MPa (88% of neat unannealed PETG strength).

Interlayer tensile strength in the neat PLA 3D printed specimen was 32.3 MPa. Annealing the PLA specimens at 120 °C did not significantly change the interlayer tensile strength. Specimens annealed at 120 °C for 30 minutes, 240 minutes, and 480 minutes had tensile strengths of 29.4 MPa, 31.3 MPa, and 31.5 MPa, respectively. Specimens annealed at 90 °C for 30 minutes, 240 minutes, and 480 minutes had tensile strengths of 35.9 MPa, 36.7 MPa, and 38.0 MPa respectively. Annealing PLA at 90 °C for 30 minutes, 240 minutes, and 480 minutes showed 11%, 13%, and 17% increase respectively in the interlayer tensile strength of PLA specimens.

The addition of carbon fiber to neat PLA decreased the mean interlayer tensile strength of the 3D printed specimens. Unannealed PLA-CF specimens had an interlayer tensile strength of 16.0 MPa. Specimens annealed at 120 °C for 30 minutes, 240 minutes, and 480 minutes had interlayer tensile strengths of 16.5 MPa, 16.9 MPa, and 16.8 MPa respectively. Specimens annealed at 90 °C for 30 minutes, 240 minutes, and 480 minutes had interlayer tensile strengths of had mean strengths of 16.8 MPa (50% of unannealed neat PLA strength), 30.8 MPa (95 % of unannealed neat PLA strength), and 29.9 MPa (93% of unannealed neat PLA strength), respectively. Annealing at 120 °C did not affect the interlayer tensile strength of CF-PLA specimens but annealing at 90 °C for 240 minutes and 480 minutes increased the strength significantly.

Figure 14 shows the interlayer Young's modulus of 3D printed neat and reinforced PETG and PLA polymer specimens subjected to annealing. The Young's modulus in the z-direction was 1730 MPa for unannealed neat PETG polymer specimens. The Young's modulus in 3-direction of PETG specimen annealed at 120 °C for 30 minutes, 4 hours, and 8 hours was 1700 MPa, 1750 MPa, and 1680 MPa. Annealing did not have any significant effect on the interlayer tensile modulus of PETG specimens.

The unannealed PETG-CF specimen had Young’s modulus of 1400 MPa in the 3-direction. PETG-CF specimens annealed for 30 minutes, 4 hours, and 8 hours had interlayer tensile strengths of 1630 MPa, 1930 MPa, and 2320 MPa respectively. Young’s modulus in the 3-direction for PETG-CF specimens increased with increasing annealing time.

Young's modulus of specimens that were 3D printed from neat PLA was not affected by annealing. The Young's modulus was 2970 MPa for unannealed PLA 3D printed specimens. The Young's modulus for PLA specimens annealed at 120 °C for 30 minutes, 4 hours, and 8 hours was 2890 MPa, 2860 MPa, and 2930 MPa, respectively. The Young's modulus for PLA specimens annealed at 90 °C for 30 minutes, 4 hours, and 8 hours was 2980 MPa, 3180 MPa, and 3150 MPa, respectively.

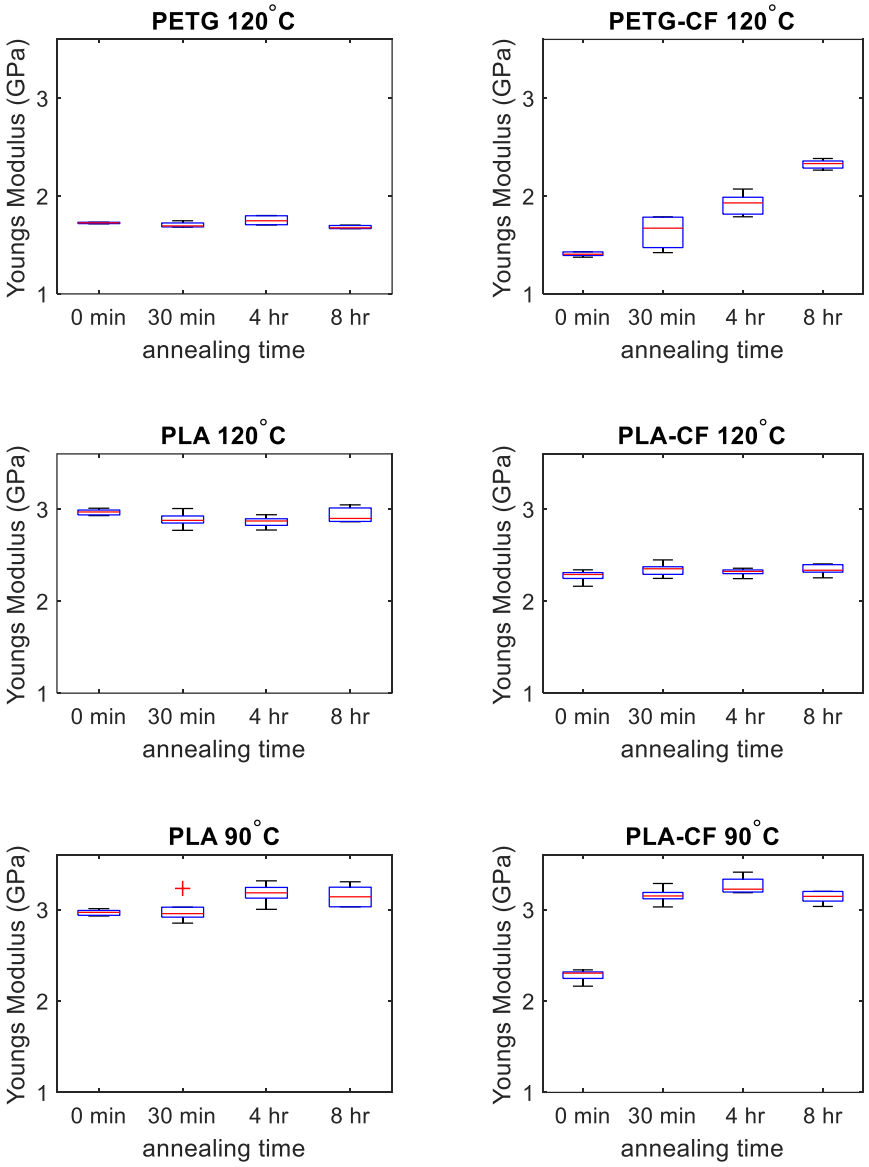

Figure 14: Interlayer Young's modulus of 3D printed neat and reinforced PETG and PLA polymer specimens subjected to annealing.

The addition of carbon fiber reinforcement reduced Young's modulus of PLA specimens in the z-direction. Annealing at 120 °C did not change the interlayer Young's modulus. The Young's modulus in the z-direction for the unannealed PLA-CF specimens was 2270 MPa. The Young's modulus for specimens annealed at 120 °C for 30 minutes, 4 hours, and 8 hours was 2340 MPa, 2310 MPa, and 2340 MPa, respectively. Annealing at 90°C, however, increased Young's modulus in the z-direction. The

Young's modulus for specimens annealed at 90 °C for 30 minutes, 4 hours, and 8 hours was 3150 MPa, 3260 MPa, and 3140 MPa, respectively.

The strain to failure values for PLA and PETG specimens annealed at different times and different temperatures are shown in Table 4.

Table 4: Strain to failure values for reinforced and neat PLA and PETG.

Polymer and annealing temperature	**Strain to failure (%), No annealing**	**Strain to failure (%), 30 minutes**	**Strain to failure (%), 240 minutes**	**Strain to failure (%), 480 minutes**
Neat PETG, 120 °C	3.49	3.31	3.27	3.18
Neat PLA, 120 °C	1.37	1.22	1.34	1.31
PETG-CF, 120 °C	1.21	1.16	1.83	1.98
PLA-CF, 120 °C	0.904	0.880	0.903	0.886
Neat PLA, 90 °C	1.37	1.62	1.57	1.70
PLA-CF, 90 °C	0.904	0.605	1.40	1.35

Strain to failure for neat polymers specimens was higher compared to reinforced polymer specimens. For neat PETG and neat PLA, annealing does not significantly affect the strain to failure values. However, annealing at 90 °C increases the strain to failure by 25%. In conjunction with other observations that showed a slight increase in strength and Young's modulus, this increase in strain to failure suggests that there was some interlayer diffusion of PLA molecules during the annealing process.

For the carbon fiber reinforced PETG, annealing at 120 °C for 8 hours increased the strain to failure by 64%. For carbon fiber reinforced PLA, annealing the specimens at 120 °C did not significantly change the strain to failure values. However, annealing the specimens at 90 °C for 8 hours increased the strain to

failure values by 49%. This suggests that, during annealing, there was an even higher degree of interlayer diffusion of PLA molecules in PLA-CF specimens compared to neat PLA specimens. The increased crystallinity of PLA molecules appears to have slowed down interlayer diffusion bonding in neat PLA specimens. The degree of crystallinity does not increase as much in PLA-CF specimens. As a result, PLA molecules are freer to move and participate in interlayer diffusion. Higher crystallinity in PLA compared to PLA-CF suggests that at a lower temperature of 90 °C, crystallinity might have a greater effect on the reptation of polymer chains across the interface than the presence of carbon fibers. However, a further study comparing the effects of crystallinity and carbon fiber on polymer chain reptation and diffusion is necessary to get a better understanding of this phenomenon.

2.4.7 Discussion of Results

The effects of annealing on the mechanical properties of 3D printed parts tested in this study are summarized in Table 5.

Table 5: Effects of annealing on the mechanical properties of 3D printed parts.

Material	Annealing temperature	Interlayer tensile strength	Interlayer Young's modulus	Interlayer strain to failure
PLA	90 °C	Minor increase	No change	Major increase
PLA-CF	90 °C	Major increase	Major increase	Major increase
PLA	120 °C	No change	No change	Minor decrease
PLA-CF	120 °C	No change	No change	No change
PETG	120 °C	No change	No change	Minor decrease
PETG-CF	120 °C	Major increase	Major increase	Major increase

2.4.7.1 Addition of short carbon fibers to the polymer

The addition of carbon-fiber reinforcement significantly decreased the interlayer tensile strength of 3D printed parts. This is true for both PLA and PETG polymers. Similar observations were made by Hwang et al. when they used copper particle-reinforced ABS polymer. Increasing the reinforcement content decreased the interlayer tensile strength.

A reason for this reduction in interlayer mechanical properties could be the increase in viscosity caused by the addition of carbon fibers [100]. Carbon fibers can be regarded as suspended solids in the fluid of molten thermoplastic polymer. The addition of such a solute increases the viscosity of the solution [101]. As a result, time for intimate contact (neck formation) and reptation time (diffusion and randomization time) increases. The polymer strands cannot diffuse effectively between the layers and result in lowered interlayer tensile strength on the addition of carbon fiber reinforcement. Micrographs in Figure 9 further show that 3D printed short carbon fiber reinforced polymers incomplete interlayer diffusion across the interface.

2.4.7.2 Annealing of PETG-CF and PLA-CF composites above the glass transition temperature

The interlayer tensile strength of 3D printed PETG-CF parts increased up to the interlayer tensile strength of 3D printed neat PETG parts by annealing at a temperature higher than the glass transition temperature of PETG. It is possible to increase the interlayer Young's modulus of PETG-CF 3D printed parts, via annealing, to a value higher than that of neat PETG 3D printed parts. Strain to failure can also be increased significantly by annealing PETG-CF 3D printed parts, but the strain to failure of PETG-CF parts does not exceed that of neat PETG parts. Annealing above glass transition temperature facilitates interlayer diffusion of polymer molecules resulting in increased entanglements and consequently increased mechanical properties as described in various research works [65, 66, 68, 102, 103]. Hence,

annealing can increase interlayer strength, Young's modulus, and strain to failure of PETG-CF 3D printed parts.

2.4.7.3 Annealing of PLA-CF composites above the cold-crystallization temperature

Annealing of neat PETG 3D printed parts and annealing of PLA 3D printed parts above cold crystallization temperature does not have any significant effect on their interlayer tensile strength, Young's modulus, or strain to failure. The PLA polymer achieved a high degree of crystallinity when it was annealed at 120 °C.

While some previous studies have shown no change in Young's modulus due to an increase in crystallinity , other previous studies have shown that an increase in crystallinity leads to an increase in the modulus [104, 105]. However, in laminated composites, if the crystals do not grow across the laminate, the modulus does not change significantly as suggested by the Halpin Tsai equations , that account for the crystal structure and aspect ratio. Further study is required to understand the effect of crystallinity on Young's modulus of 3D printed parts.

Researchers have observed that the evolution of stable molecular confirmations attributable to increasing crystallinity slows down the diffusion bonding process. Annealing neat PLA 3D printed parts at a temperature below cold crystallization temperature (90 °C) showed a modest increase in interlayer tensile strength, Young's modulus, and strain to failure. This increase was most likely attributable to the interlayer diffusion bonding of PLA polymer during the annealing process. Even though the crystallinity of neat PLA increases significantly (4.2% to 20%), the degree of the diffusion bonding process that takes place was significant enough to increase the interlayer mechanical properties.

Annealing at a temperature higher than cold crystallization temperature has no significant effect on interlayer tensile strength, Young's modulus or strain to failure of PLA-CF 3D printed parts. It has been observed in some studies that the presence of crystallinity in a semi-crystalline polymer prevents or

greatly hinders long-range molecular mobility, preventing the interdiffusion process during autohesion. Annealing of PLA specimens at 120 °C caused an increase in crystallinity. This increase in crystallinity could be the reason for the ineffectiveness of annealing on increasing interlayer tensile strength for PLA-CF parts. Annealing at a temperature lower than the cold crystallization temperature (annealing at 90 °C) significantly increased the interlayer tensile strength, Young's modulus, and strain to failure of PLA-CF 3D printed parts. The PLA-CF specimens annealed at 90 °C increased in crystallinity (3.9% to 10%) but the degree of crystallinity was significantly lower compared to the neat PLA counterparts (20%) annealed at 90 °C. This finding suggests that although the diffusion bonding process was retarded attributable to the increase in crystallinity, the diffusion bonding was fast enough to cause a significant increase in mechanical properties during 4 and 8 hours of elevated temperatures.

2.5 Conclusions

Rheological and thermal analyses of 3D printed composites were used to provide a better understanding of the interlayer adhesion strength response and, therefore, overcome a mechanical performance limitation of these materials. The following conclusions have been drawn from the study:

1. The rheological and thermal behavior of polymer affects the interlayer mechanical properties of 3D printed composites. Short carbon fiber reinforced 3D printed composites have significantly reduced interlayer tensile strength (66% for an amorphous polymer and 50% for a semi-crystalline polymer) compared to their neat polymer counterparts. The addition of carbon fibers to the polymers increases viscosity and slows the interlayer diffusion process.
2. An effective temperature window was established for post-process annealing of 3D printed composites. For amorphous polymer composites, the effective post-processing temperature is between the glass-transition temperature of the polymer and the temperature at which the 3D printed part deforms significantly during post-process annealing. For semi-crystalline polymers, the

effective post-processing temperature lies between the glass-transition temperature of the polymer and the cold-crystallization temperature. Above the cold-crystallization temperature, the formation of crystals slows down the interlayer diffusion of the polymer chains.

3. Postprocessing via annealing was found to be effective in recovering the reduced interlayer tensile strength of the 3D printed composites. Interlayer tensile strength of 3D printed PETG-CF and PLA-CF composites increased by three times and two times respectively by annealing at a suitable temperature and attained the interlayer tensile strength of their neat polymer counterparts.
4. Postprocessing via annealing increased the interlayer Young's modulus and ductility of the 3D printed composites. For the amorphous polymer composite, the interlayer Young's modulus increased by 1.65 times compared to unannealed 3D printed composite and by 1.32 times compared to annealed 3D printed neat polymer. For the semi-crystalline polymer, the interlayer Young's modulus increased by 1.48 times compared to the unannealed 3D printed composite. Similarly, a 64% increase in interlayer strain-to-failure was achieved for the 3D printed amorphous composite and a 49% increase in interlayer strain-to-failure for the 3D printed semi-crystalline composite.

CHAPTER 3
MODELING BIMODULAR BENDING BEHAVIOR USING LAMINATE ANALYSIS AND FINITE ELEMENT ANALYSIS

3.1 Chapter abstract

This research extends the existing CLT (classical laminate theory) -based finite element (FE) models to predict elasto-plastic and bimodular behavior of 3D printed composites with orthotropic material properties. Short carbon fiber (CF)-reinforced acrylonitrile butadiene styrene (ABS) was selected as the 3D printing material. Material characterization of a 3D printed unidirectional laminate was carried out using mechanical tests. A bimodular material model was implemented using explicit FE analysis to predict the tension and bending behavior of a 3D printed laminate. The results of the FE model predictions were experimentally validated. Hill's yield function was effective at predicting the elasto-plastic stress-strain behavior of the laminate in tension. In bending, bimodular material behavior along with Hill's yield function worked reasonably well in predicting the elasto-plastic bending of the laminate. The material model proposed can be used to predict the mechanical behavior of 3D printed parts with complex geometry under complex loading and boundary conditions. [2]

[2] The research work presented in this chapter has been published as:
Bhandari, S., Lopez-Anido, R.A., Wang, L. et al. Elasto-Plastic Finite Element Modeling of Short Carbon Fiber Reinforced 3D Printed Acrylonitrile Butadiene Styrene Composites. JOM 72, 475–484 (2020). https://doi.org/10.1007/s11837-019-03895-w

3.2 Introduction

The extrusion-based 3D printing process also called fused deposition modeling (FDM) and fused filament fabrication (FFF), is currently the most common 3D printing process used for additive manufacturing of polymer composite parts [7]. An extrusion-based 3D printed part is produced by depositing beads of molten thermoplastic layer by layer which results in a part with orthotropic material properties.

Researchers have used laminate analysis to model the mechanical behavior of 3D printed parts. Recent research works show that the linear elastic behavior of 3D printed parts under tension loading can be successfully modeled using CLT (classical laminate theory). Kulkarni and Dutta[3] developed an analytical model using laminate analysis to determine the elastic moduli of 3D printed laminates with layers oriented at different angles. Rodriguez et al. [4] introduced a strategy for optimizing the design of fused deposition modeling (FDM)-based 3D printed materials using laminate analysis. Li et al. [5] analyzed FDM-based 3D printed materials using laminate analysis and proposed a set of equations to determine the elastic constants of FDM prototypes based on the analysis. Alaimo et al. [6] modeled the elastic behavior of FDM-based 3D printed material using classical lamination theory and used the Tsai-Hill yielding criterion to predict the yielding of the 3d printed material in tension loading.

The difference in elastic response of some materials in compression compared to tension has been known for a long time [106, 107]. Jones discussed fiber-reinforced polymers that have a tension modulus up to 40% higher than the compression modulus. Phan-Thein discussed the bimodular behavior of short fiber-reinforced polymers and its implications regarding the use of high fiber aspect ratios for bending applications. Similar bimodular behavior has been observed in extrusion-based 3D printed parts. Ziemen et al. reported a tensile modulus of 987 MPa and a compression modulus of 402 MPa for 3D printed acrylonitrile butadiene styrene (ABS) parts at 0° orientation. At 90° orientation, the tensile modulus was found to be 738 MPa and the compression modulus was found to be 382 MPa

[108]. Song et al. reported similar bimodular behavior in 3D printed PLA parts. An elastic modulus derived from bending tests would be useful in approximating the linear-elastic bending behavior of such bimodular materials at small deflections. However, when geometry, boundary conditions, and loadings are complex or the yielding of materials is taken into account, the results from models based on bending elastic modulus deviate significantly from the experimental results .

Different numerical techniques have been proposed to address the bimodular behavior of materials. Sun et al. reviewed different approaches to model the mechanical behavior of bimodular materials [109]. The two basic approaches that are generally used to model bimodular behavior are 1) Bert's model [110] and 2) Ambartsumyan's model [111]. Bert's model uses either the tensile or compressive modulus based on whether the strains in the fiber are positive or negative. Ambartsumyan's model uses tensile or compressive modulus based on whether principal stress is positive or negative. Although not specific to 3D printed materials, Babesko et al. [112] proposed a numerical technique for analysis of the elastoplastic stress-strain state of transversely isotropic shells with different moduli in compression and tension. Zhang et al.[113] discussed different numerical techniques to create a stabilized complementarity formulation for 3D bimodular materials. Li et al. [60] discussed different analytical solutions for functionally graded beams. A suitable material model should accurately predict the bending behavior of the 3D printed laminate.

In addition to the linear elastic bimodular behavior, the elastoplastic behavior of the 3D printed parts also should be determined to accurately model the response of 3D printed material to different loadings. Hill's yield criterion and Tsai-Hill yield criterion have been used to model the yielding behavior of 3D printed materials [114, 115]. Destrade et. al.[116] showed that a simple finite element model cannot accurately predict the bending behavior of a bimodular material like bimodular rubber.

Different mechanical finite element models have been created for polymer extrusion-based 3D printed materials. Bhandari and Lopez-Anido [117, 118] used a space frame-based finite element model to generate effective homogenized properties for 3D printed cellular structures. Guessasma et al used finite element modeling to explain damage mechanisms in 3D printed polymers subject to severe compression. The finite element model used by Nouri et al. [119] predicted the transverse symmetry 3D printed ABS parts. Guessasma et al. [120] used finite element modeling to point out that the combination of local shearing and inhomogenous stretching correlated to the filament arrangement in 3D printed PETG (Polyethylene terephthalate glycol) parts within the plane of construction. Werken et al.[121] discussed different considerations for developing a suitable finite element model for 3D printed parts. Xu et al. used finite element modeling to predict the deformation of disordered lattice structures. Somireddy et al. [122] developed a constitutive material model and used classical lamination theory (CLT) and nonlinear finite element analysis (FEA) with Hill's yield criteria and first ply failure to predict the bending response of 3D printed ABS parts. While these models are quite successful in predicting the tensile and compressive behavior of the 3D printed material, CLT based finite element model that considers the bimodular linear elastic behavior and yielding would be useful in predicting yielding and bending response of 3D printed short carbon fiber reinforced polymer parts.

This research work aims to extend the existing CLT-based linear-elastic FEA used for modeling the mechanical response of 3D printed composite parts by addressing the bimodular and elasto-plastic behavior of 3D printed composite materials.

Progressive damage and ultimate strength prediction are beyond the scope of this research work. Past research work has shown that post ultimate strength behavior in short fiber-reinforced composite laminate needs to incorporate lamina strengths parameters in different directions [123], progressive

fiber/matrix debonding in short-fiber reinforced composites [124], and progressive fracture mechanisms [125].

The objectives of this research work are 1) Implement a bimodular elasto-plastic material finite element model to describe the bending behavior of a 3D printed short carbon fiber-reinforced ABS part, and 2) Validate the bimodular elasto-plastic material finite element model experimentally.

3.3 Materials and methods

3.3.1 Modeling approach for 3D printed material

The 3D printed parts were modeled as shells with stacked layers of orthotropic laminae oriented at different angles. The shell was homogenized using laminate analysis. The material behavior was divided into linear elastic and elasto-plastic regions.

3.3.1.1 Linear elastic behavior

Several material models have been discussed by researchers to efficiently implement the linear elastic bimodular behavior of the material in a finite element model [29, 126-128]. This study uses a simple 2D orthotropic material model for a lamina based on a modified Bert's constitutive equations for bimodular materials. In Bert's model [110] for fiber reinforced laminated composites, elastic constants are updated based on whether the fibers are under tensile or compressive strain. The paper states that the nonsymmetric-compliance-matrix model gave considerably improved agreement with experimental data for S21 vs θ but lowered agreement for S11 vs θ. The relatively improved agreement of nonsymmetric model over classical symmetric comes at fundamental objections related to the energy conservation and practical objection related to finite element methods. Bert [110] also suggested the use of reciprocity based Poisson's ratio can be used to generate bilinear-symmetric-compliance model.

The material model used in this study updates the elastic constants on whether the material is under tensile or compressive stress. However, unlike Bert's model, the model used for this study considers stress along the fibers as well as stress in the transverse direction. The model considers stress along the fiber for selecting the modulus along the fiber and stress transverse to the fibers for selecting the modulus in the transverse direction. This implementation was chosen because it allows for incorporation of bimodularity in longitudinal direction as well as in the transverse direction. This process might result in element stiffness matrices that are not symmetric. While the fundamental objections regarding energy considerations still apply for when using this approach, the practical objection mentioned by Bert [110] has been partially alleviated by the fact that modern FEA software allow for the use of unsymmetric matrix while maintaining the stability of the solution.

For yielding, the yield constants were based on stress in along the fiber direction as it allows for easy incorporation of elasto-plastic behavior into the finite element model through Hill's yielding function.

The user-defined material subroutine in Abaqus, VUMAT, was used to define the material behavior. Equation 3.1 shows the in-plane stress-strain relationship for the material.

$$\begin{Bmatrix}\varepsilon_1\\ \varepsilon_2\\ \gamma_6\end{Bmatrix} = \begin{bmatrix} \frac{1}{E_1} & -\frac{\nu_{21}}{E_2} & 0 \\ -\frac{\nu_{12}}{E_1} & \frac{1}{E_2} & 0 \\ 0 & 0 & \frac{1}{G_{12}} \end{bmatrix} \begin{Bmatrix}\sigma_1\\ \sigma_2\\ \sigma_6\end{Bmatrix} \tag{3.1}$$

$$\text{and, } \varepsilon_3 = -\frac{\nu_{13}}{E_1}\sigma_1 - \frac{\nu_{23}}{E_2}\sigma_2$$

where,

ε_1 = strain in the 1-direction of the material

ε_2 = strain in the 2-direction of the material

γ_6 = engineering shear strain in the 1-2 plane of the material

E_1 = Young's modulus in the 1-direction of the material

E_2 = Young's modulus in the 2-direction of the material

ν_{21} = Poisson's ratio for loading in the 2-direction of the material

ν_{12} = Poisson's ratio for loading in the 1-direction of the material

G_{12} = shear modulus in the 1-2 plane of the material

Since the material shows bimodular nature, with different modulus in compression and tension, Young's moduli and the corresponding Poisson's ratios are defined based on whether the normal stresses along material axes are positive or negative. This scheme has been implemented using equations 3.2 through 3.5.

$$E_1 = \langle \frac{\sigma_1}{|\sigma_1|} E_1^t \rangle + \langle \frac{-\sigma_1}{|\sigma_1|} E_1^c \rangle \tag{3.2}$$

$$E_2 = \langle \frac{\sigma_2}{|\sigma_2|} E_2^t \rangle + \langle \frac{-\sigma_2}{|\sigma_2|} E_2^c \rangle \tag{3.3}$$

$$\nu_{12} = \langle \frac{\sigma_2}{|\sigma_2|} \nu_{12}^t \rangle + \langle \frac{-\sigma_2}{|\sigma_2|} \nu_{12}^c \rangle \tag{3.4}$$

$$\nu_{21} = \langle \frac{\sigma_1}{|\sigma_1|} \nu_{21}^t \rangle + \langle \frac{-\sigma_1}{|\sigma_1|} \nu_{21}^c \rangle \tag{3.5}$$

where,

E_1^t = Young's modulus in the 1-direction in tension

E_1^c = Young's modulus in the 1-direction in compression

E_2^t = Young's modulus in the 2-direction in tension

E_2^c = Young's modulus in the 2-direction in compression

ν_{12}^t = Poisson's ratio for loading in the 1-direction in tension

ν_{12}^c = Poisson's ratio for loading in the 1-direction in compression

ν_{21}^t = Poisson's ratio for loading in the 2-direction in tension

ν_{21}^c = Poisson's ratio for loading in the 2-direction in compression

σ_1 = normal stress in the 1-direction

σ_2 = normal stress in the 2-direction

| | is an absolute value operator

⟨ ⟩ is a Macaulay operator, defined as:

$\langle a \rangle = a$ if a is positive

$\langle a \rangle = 0$ if a is negative

Abaqus explicit solver is used to solve for the stresses in material with each time increment. Because the material exhibits bimodular behavior, a sudden change in matrix stiffness occurs when the stress direction is changed. The Jacobian matrix of the system is necessary for implicit solvers and the Jacobian matrix is not well defined in the region of sudden stiffness change. Various implicit models have been developed to overcome the limitation [129, 130]. However, for this research work, an explicit solver is adequate as it can provide solutions in a reasonable amount of time.

The stress vector at the kth time step using indicial notation is shown by Equation 3.6.

$$\sigma_i{}^k = \sigma_i{}^{k-1} + Q_{ij}^k \, d\varepsilon e_j^k \tag{3.6}$$

where $\sigma_i{}^{k-1}$ = stress vector at (k-1)th time step

Q_{ij}^k = laminate stiffness matrix at the kth time step

$d\varepsilon e_j^k = d\varepsilon e_j^k - d\varepsilon e_j^{k-1}$ = elastic strain increment at the kth time step

3.3.1.2 Yielding Behavior

Several suitable elasto-plastic models are discussed in the literature for composite materials [131-133]. A simple elasto-plastic model for orthotropic materials was adopted. The incremental formulation with isotropic work hardening was assumed. The components of the total strain increment at the kth time step are shown by Equation 3.7.

$$d\varepsilon_j^k = d\varepsilon e_j^k + d\varepsilon p_j^k \tag{3.7}$$

where,

$d\varepsilon e_j^k$= elastic component of the total strain increment at the kth time step

$d\varepsilon p_j^k$ = plastic component of the total strain increment at the kth time step

The total stress increment at the kth time step caused by the elastic strain is shown by Equation 3.8.

$$d\sigma_i^k = Q_{ij}^k d\varepsilon e_j^k \tag{3.8}$$

where,

Q_{ij}^k= laminate stiffness matrix at the kth time step

$d\varepsilon e_j^k$= elastic portion of the total strain increment at the kth time step

The Hill's quadratic yield function adopted is shown by Equation 3.9.

$$f(\sigma) = \sqrt{F(\sigma_{22} - \sigma_{33})^2 + G(\sigma_{33} - \sigma_{11})^2 + H(\sigma_{11} - \sigma_{22})^2 + L{\sigma_{23}}^2 + M{\sigma_{31}}^2 + N{\sigma_{12}}^2} \quad (3.9)$$

where,

$$F = \frac{1}{2}\left(\frac{1}{R_{22}^2} + \frac{1}{R_{33}^2} - \frac{1}{R_{11}^2}\right)$$

$$G = \frac{1}{2}\left(\frac{1}{R_{33}^2} + \frac{1}{R_{11}^2} - \frac{1}{R_{22}^2}\right)$$

$$H = \frac{1}{2}\left(\frac{1}{R_{11}^2} + \frac{1}{R_{22}^2} - \frac{1}{R_{33}^2}\right)$$

$$L = \frac{3}{R_{23}^2}$$

$$M = \frac{3}{R_{31}^2}$$

$$N = \frac{3}{R_{12}^2}$$

σ_1 = normal stress in the 1-direction

σ_2 = normal stress in the 2-direction

σ_3 = normal stress in the 3-direction

σ_{23}= shear stress in the 2-3 plane

σ_{31}= shear stress in the 3-1 plane

σ_{12}= shear stress in the 1-2 plane

R_{11}, R_{22}, R_{33}, R_{23}, R_{31}, R_{12} are the orthotropic yield stress ratios

The Hill's yield function for plane stress conditions is reduced from Equation 3.10, as follows:

$$f(\sigma) = \sqrt{F(\sigma_{22}^2) + G(\sigma_{11}^2) + H(\sigma_{11} - \sigma_{22})^2 + N{\sigma_{12}}^2} \tag{3.10}$$

where,

R_1 = $\sigma_{y1}^2/\sigma_{y1}^2$=1.0

R_2 = $\sigma_{y1}^2/\sigma_{y2}^2$

R_6 = 3 $\sigma_{y1}^2/\sigma_{y6}^2$

σ_{y1} = yield stress determined from uniaxial tests in the 1-direction

σ_{y2}= yield stress determined from uniaxial tests in the 2-direction

σ_{y6} = yield stress determined from shear tests in the 1-2 plane

σ_1 = axial stress in the 1-direction

σ_2 = axial stress in the 2-direction

σ_6= shear stress in the 1-2 plane

The yield ratios are calculated based on whether the σ_1 for the element is positive or negative. The plastic hardening curve (stress vs plastic strain) is also used based on whether σ_1 is positive or negative. If σ_1 is positive, the plastic hardening curve from tension tests in 1-direction else the plastic hardening curve from compression test in 1-direction is used. The equivalent plastic strain is shown by Equation 3.11.

$$d\lambda^k = \frac{n_j^k \; Q_{ij}^k \; d\varepsilon_i^k}{n_j^k \; Q_{ij}^k \; n_i^k \; + \; h^k} \tag{3.11}$$

where,

$n_j^k = \frac{\partial f(\sigma)}{\partial \sigma_j^k}$

$d\varepsilon_i^k$ is the total strain increment at the kth time step

$\mathrm{h^k} = \frac{\mathrm{d}\sigma_{\mathrm{i}}^{\mathrm{k}}}{\mathrm{d}\varepsilon\mathrm{p}_{\mathrm{j}}^{\mathrm{k}}}$ is the strain hardening coefficient, the slope of the stress vs

plastic strain curve at given stress at the kth time step

The total stress increment from equation 3.8 is re-written as a function of the strain increment and the plastic multiplier, as Equation 3.12.

$$\mathrm{d}\sigma_i^k = Q_{ij}^k\left(\mathrm{d}\varepsilon_j^k - \mathrm{d}\lambda^k . n_j^k\right) \tag{3.12}$$

The algorithm proposed by Dunne and Petrinic [133] is used to calculate the stress and strain increment at each update. The algorithm evaluates the yield function and determines if the material is actively yielding. If the material is actively yielding, it calculates the plastic multiplier, stress increment, and isotropic hardening coefficient. The algorithm finally updates all the quantitates to the end of the time increment using explicit integration.

3.3.2 Experimental methods

Experiments were carried out for material characterization to generate input material properties for the finite element model. Seven elastic constants $E_{1t}, E_{2t}, \nu_{12t}, G_{12}, E_{1c}, E_{2c}, \nu_{12c}$ along with six yield stresses $S_{1yt}, S_{2yt}, S_{12y}, S_{1yc}, S_{2yc}, S_{12y}$, and two strain hardening curves for tension in the 1-direction and compression in the 1-direction were necessary for the finite element modeling the elasto-plastic behavior of the 3D-printed carbon-ABS parts.

3.3.2.1 Material characterization experiments

Material characterization tests were carried out to determine the material properties required for modeling. 3D printed unidirectional test specimens were used to determine the material properties. A Lulzbot Taz 6 printer was used for printing the specimens. CarbonX CFR-ABS filament from 3Dxtech was used. Laminates with nine layers were printed using the printing parameters listed in Table 6.

Table 6: Printing parameters for the 3D printed specimens.

Parameter	**Value**
Nozzle Diameter	0.8 mm
Retraction distance	1.5 mm
Retraction speed	90 mm/s
Layer height	0.36 mm
Outline perimeters/shells	0
Top/ bottom solid layers	0
Infill	None
Extruder Temperature	240°C
Bed Temperature	110°C
Printing speed	60 mm/s
Printing speed for the first layer	12 mm/s
Movement speed	60 mm/s
Layer cooling fan	Off

Mechanical characterization of the 3D printed laminate in tension, compression, and shear was conducted according to ASTM D638, ASTM D6641, and ASTM D7078, respectively. All specimens were prepared on a water jet and conditioned at 50% relative humidity and a temperature of 23°C before evaluation. The strain was measured during each experiment using ARAMIS, a non-contact digital image correlation (DIC) system .

All mechanical tests were carried out on a servo-hydraulic Instron testing frame. A 1kN load cell was used for tension, compression, and shear tests. A 200N load cell was used for bending tests. The crosshead displacement rate for the tension tests was 5mm/min per ASTM D638. The crosshead displacement rate for the compression tests was 1.3mm/min. The crosshead displacement rate for the shear tests was 2mm/min.

The material properties obtained from tension, compression, and shear tests were used as input properties for the model. The weakness in the interlayer bonds is incorporated in the model by Young's modulus (T2) in the 90° orientation laminates, the shear modulus (G23) across beads as shown in Table 3. The interlayer weakness is also incorporated in the model via Hill's yield constants that govern the yielding behavior of the material in the model.

An ASTM D638 tension test and an ASTM D790 bending test were simulated using finite element modeling. Abaqus 6.13 was used for finite element modeling. A user-defined material model was used to define the stress-strain behavior of the unidirectional material.

A 2D planar deformable shell part was created with dimensions corresponding to the ASTM D638 type II specimen. Another 2D planar deformable shell part was created with dimensions corresponding to ASTM D790 bending specimen. A composite layup was defined with [0/-45/45/90/0/90/45/-45/0] orientation with each layer being 0.36 mm thick. Each layer was assigned three integration points. An explicit dynamic solving step was defined. The time increment was defined automatically by Abaqus.

For tension test finite element models, a constant displacement of 5mm/minute was applied at one gripping end and another gripping end was kept fixed. Reference point 1 was used for measuring reaction force and for applying fixed boundary conditions. Reference point 2 was used to apply displacement to the gripping end of the specimen. Reference points 3 and 4 were used for measuring

the displacement of the gauge section. The reference points and the boundary conditions for the model are shown in Figure 15. S4R element, which defines a 4-node doubly curved thin or thick shell, with reduced integration, and hourglass control for finite membrane strains was used for meshing. S3R element, which is a 3-node triangular thin or thick shell, finite membrane strain element, was used if the curved geometry of the specimen did not allow for quadrilateral elements. A mesh with 2301 linear quadrilateral elements and 14 linear triangular elements was obtained. A total of 2513 nodes were created for the analysis. Mesh convergence for the tension test finite element model was verified by plotting the maximum reaction force vs the number of nodes in the model.

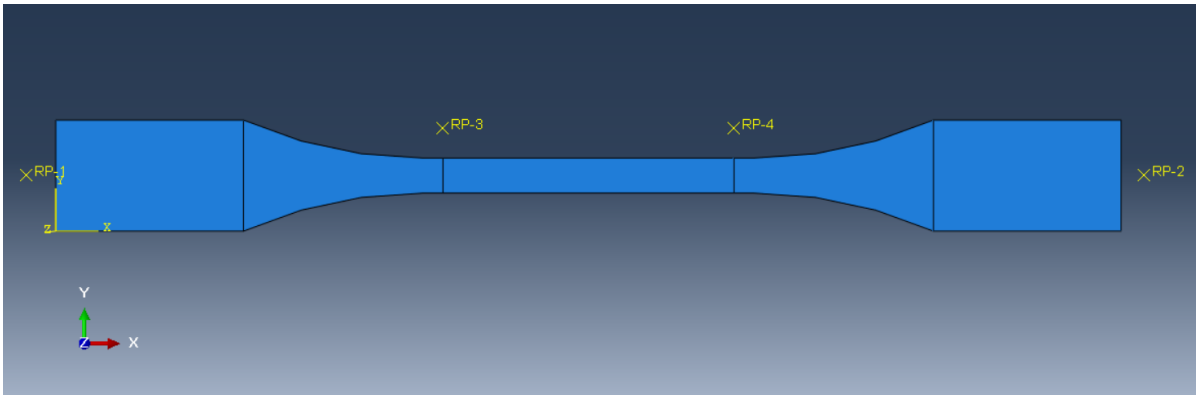

Figure 15: Finite element model of ASTM D638 type II specimen for tension.

For bending test finite element models, a constant displacement of 5 mm/minute was applied at the center, and simply supported boundary condition was applied at the support positions. Reference point 1 was used for applying the displacement. The reference points and the boundary conditions for the model are shown in

Figure 16. S4R element, which defines a 4-node doubly curved thin or thick shell, with reduced integration, and hourglass control for finite membrane strains was used for meshing. A mesh with 1378 linear quadrilaterals was obtained. A total of 1498 nodes were created for the analysis. Mesh

convergence for the bending test finite element model was verified by plotting the maximum reaction force at reference point 1 versus the degrees of freedom in the model.

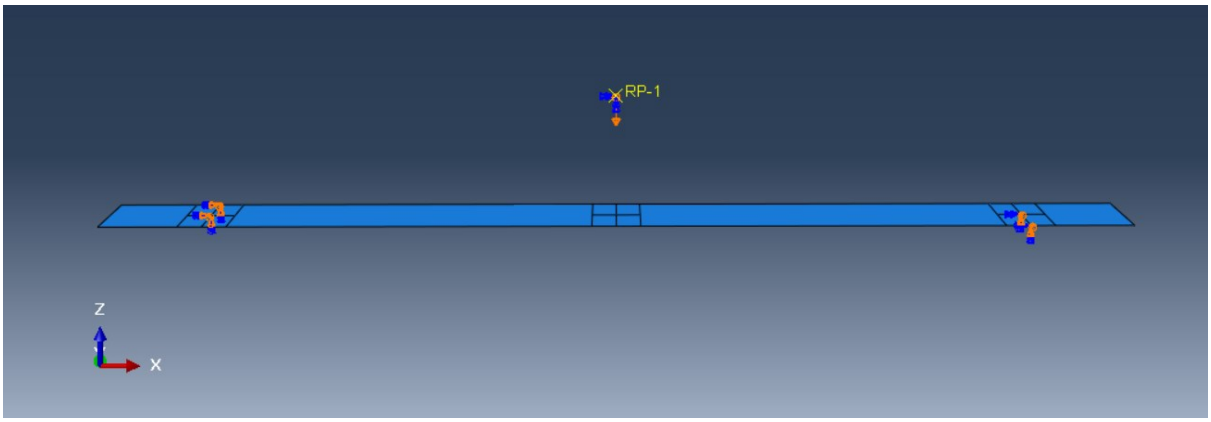

Figure 16: Finite element model of ASTM D790 specimen for bending.

3.4 Results and discussion

3.4.1 Material characterization tests

The results from the material characterization experiments are listed in Table 7.

Table 7: Mechanical properties from material characterization tests (COV values in parenthesis).

	T1 (0°)	T2(90°)	C1(0°)	C2(90°)	G13 (between beads)	G23 (across beads)
Modulus (GPa)	5.70 (1.5%)	2.17 (6.5%)	3.58 (6.7%)	2.32 (5.4%)	0.851 (3.9%)	0.909 (5.0%)
Ultimate Strength (MPa)	44.3 (0.43%)	13.74 (15%)	60.5 (1.6%)	49.3 (1.0%)	24.2 (5.7%)	25.1 (3.9%)
0.2% offset strength (MPa)	41.7 (0.56%)		57.4 (3.1%)	41.2 (8.6%)	20.0 (10%)	19.6 (15%)
Poisson ratio	0.392 (6.6%)	0.161 (18.0%)	0.391 (7.0%)	0.137 (7.7%)	-	-
0.005% offset strength (MPa)	21.5 (0.25%)	12.9 (8.3%)	23.5 (4.4%)	21.4 (3.3%)	14.4 (7.5%)	14.0 (8.2%)

It was observed that Young's modulus in tension in the 1-direction is 1.53 times the compression modulus. However, Young's modulus in tension in the 2-direction is 0.93 times the compression modulus. For tension tests in the 2-direction, the material failure was comparatively brittle and 0.2% offset strength could not be calculated. The bimodular behavior is more pronounced in the direction of fiber alignment, and the observation is consistent with the assumption made by Phan-Thein that the cause of bimodularity is related to the short carbon fiber and not the matrix. Researchers have explained that the difference in Young's modulus in compression and tension is caused by a difference in loading rate. However, in this research work, cross-head displacement for compression was 1.3mm/min for a gage length of 13 mm while that for tension specimens was 5mm/min for a gage length of 50 mm. The strain rate measured by the DIC system in the gage area was very close to each other for the linear-elastic portion of the test.

Significant yielding occurs before the material reaches 0.2% offset strength. While the 0.2% offset strength serves well for predicting yielding failure with Hill's yield criteria, the initiation of yielding occurs much earlier. A 0.005% offset strength was assumed as the initiation point of yield. Figure 17 shows the 0.005% offset strength in the stress-strain curves of specimens loaded along the 1-direction in tension and compression.Figure 18 shows the 0.005% offset strength in the stress-strain curves of specimens loaded along the 2-direction in tension and compression.

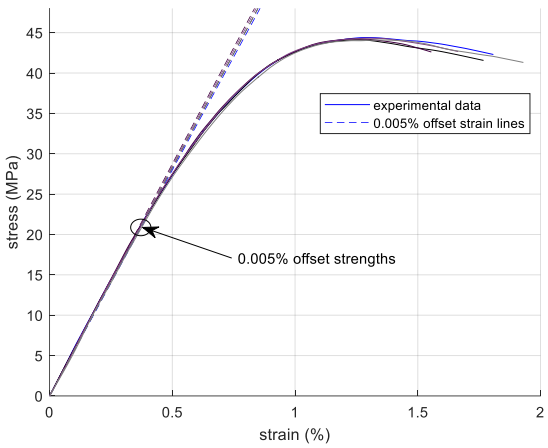

a) Tension Tests

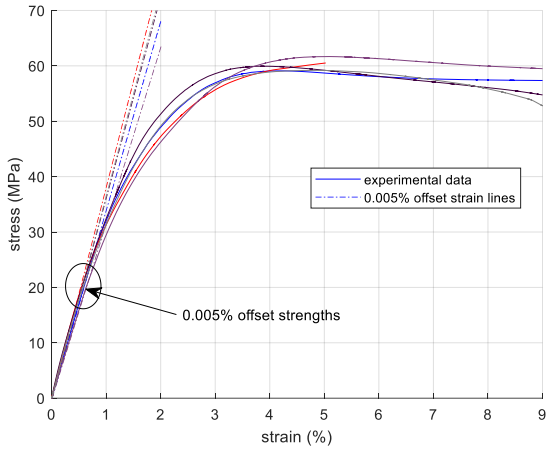

b) Compression Tests

Figure 17: Stress vs strain plots for loading in the 1-direction.

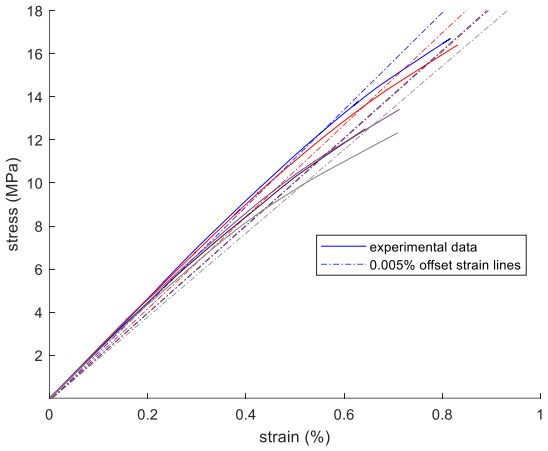

b) Tension Tests

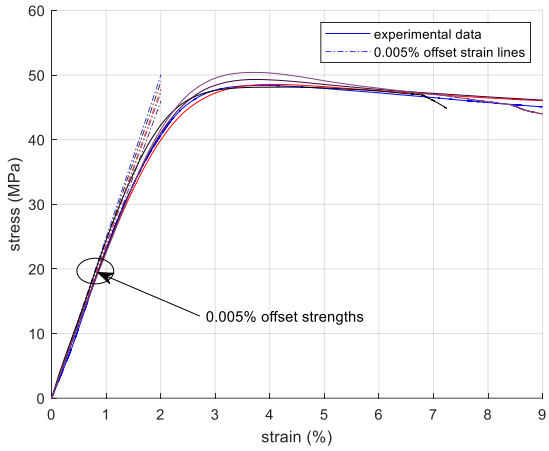

c) Compression Tests

Figure 18: Stress vs strain plots for loading in the 2-direction.

Figure 19 shows the 0.005% offset strength in the stress-strain curves of specimens loaded along the 1-2 plane in shear. Hill's yield constants were calculated based on 0.005% offset strength.

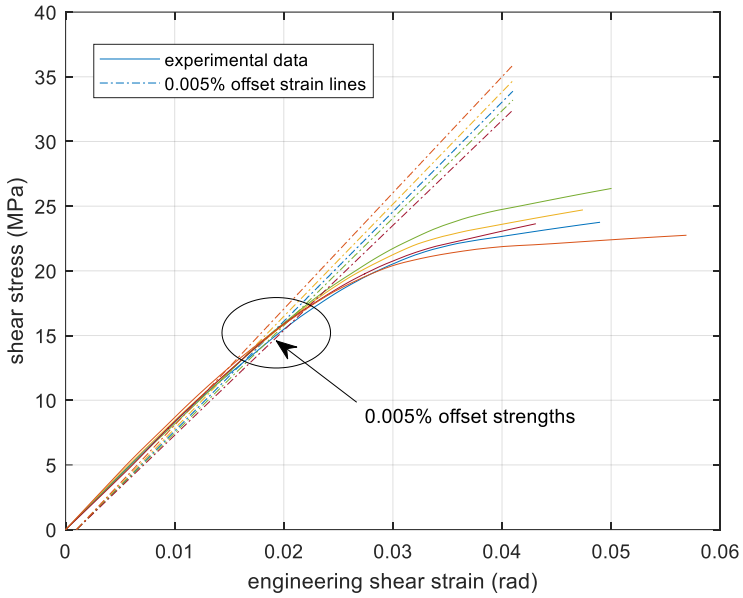

Figure 19: Shear stress vs engineering shear strain for loading in the 1-2 plane.

3.4.2 Finite element model results

Table 8 summarizes the results from the eight test cases used for the study.

Table 8: Summarized results from the finite element models.

Material behavior	Test	Results
Linear Elastic with tension modulus	Tension	The elastic modulus of the 3D printed laminate from the model (3.26 MPa) matched closely with the experimental results (3.46 MPa).
Hill's yielding with tension modulus	Tension	Elastic modulus and elasto-plastic yielding behavior matched closely with experimental results as shown in Figure 20.
Linear elastic with tension modulus	Bending	Over-predicted bending stiffness (6.94 N/mm) by 17%.
Linear elastic with compression behavior	Bending	Under-predicted bending stiffness (4.90 N/mm) by 17%.
Linear elastic with bimodular behavior	Bending	Bending stiffness from the model (5.80 N/mm) matched closely with the experimental results (5.90 N/mm).
Elasto-plastic with tension modulus and Hill's yield criterion	Bending	Over-predicted tangent bending stiffness, under-predicted ultimate load as shown in Figure 23.
Elasto-plastic with compression modulus and Hill's yield criterion	Bending	Under-predicted tangent bending stiffness, over-predicted ultimate load as shown in Figure 23.
Elasto-plastic with bimodular behavior and Hill's yield criterion	Bending	Slightly under-predicted tangent bending stiffness and ultimate load as shown in Figure 23.

Figure 20 shows the stress-strain behavior of the tension specimens. The finite element model with linear elastic behavior closely predicts the linear elastic behavior of the laminate under tension. The Young's modulus of the laminate as predicted by the finite element model is 3.27 GPa, whereas that predicted by laminate analysis is 3.26 GPa. The Young's modulus calculated from validation experiments is 3.46 GPa with a COV of 1.003 %. Elasto-plastic tensile behavior of the test laminate predicted by the finite element model that used Hill's yielding function closely matched the experimental results. In the

tension tests, all the layers experience equal tensile strain. The 0° layers reach the yield stress earlier because they have a higher modulus along the loading direction.

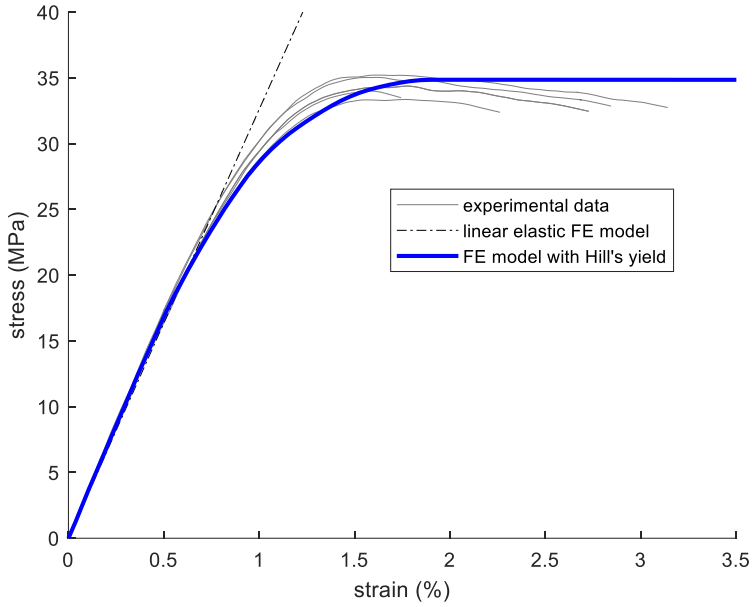

Figure 20: Stress vs strain plot from experiments and the finite element models of the tension tests.

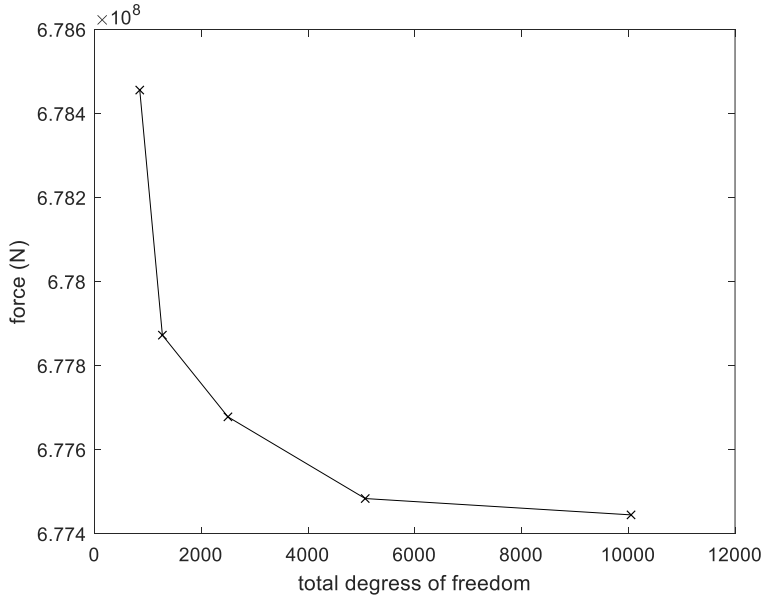

Figure 21: Mesh convergence for the tension test finite element model considering yielding.

The mesh convergence plot for the tension test finite element model is shown in Figure 21. The force required to yield the 3D printed part in tension seem to be converging with increasing total degrees of freedom.

Figure 22 shows the load vs deflection behavior of the bending specimens. In bending, the top and the bottom layers experience higher strains compared to the middle layers. It was observed that the bottom layer started yielding earlier than the top layer.

Because a specimen under a bending load experiences tension as well as compression forces, assigning the tensile Young's modulus for the entire beam over-predicts the bending stiffness whereas assigning the compression Young's modulus for the entire beam under-predicts the bending stiffness of the beam. Considering the bilinear behavior with tension modulus for regions in tension and compression modulus for regions in compression results in a load-displacement curve that tracks the experimental data closely. The bending stiffness from the model considering the tension modulus is 6.94 N/mm and that from the laminate analysis is 6.88 N/mm. The bending stiffness from the finite element model considering the compression modulus is 4.90 N/mm and that from the laminate analysis is 4.73 N/mm. The bending stiffness from the finite element model that accounts for the bimodular nature of the material is 5.80 N/mm. The bending stiffness calculated from experimental data is 5.90 N/mm.

It was observed in the experiments that the failure initiated with the specimens developing a crack at the bottom fiber at midspan below the load.

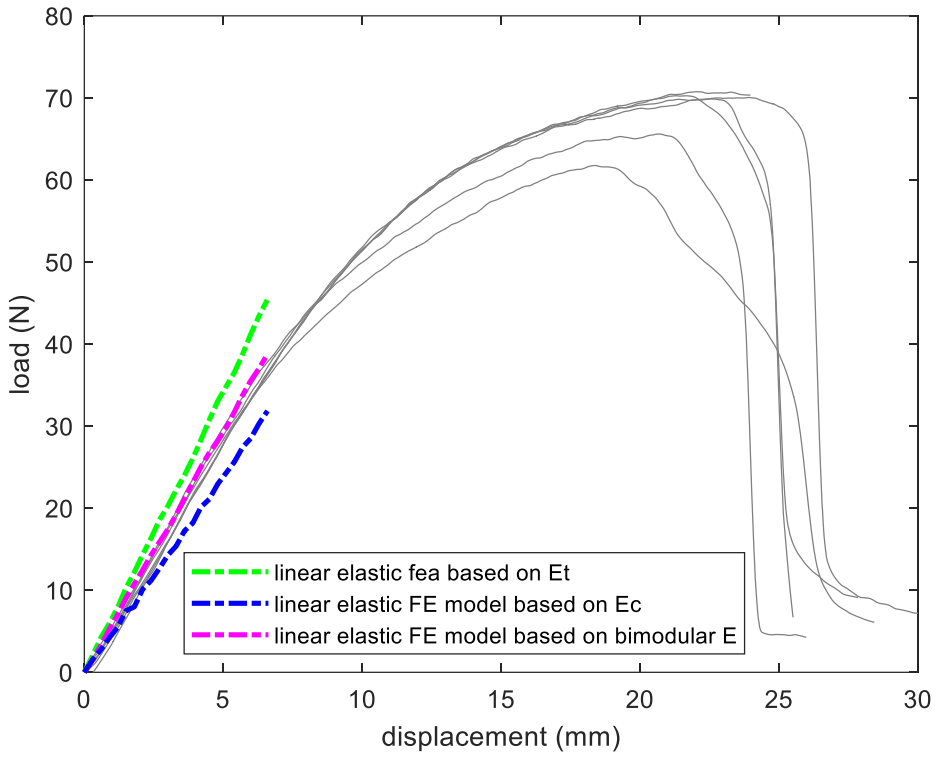

Figure 22: Load-deflection plot from the bending experiments and the bending finite element model using compression behavior, tension behavior, and bimodular behavior.

Figure 23 shows the results from the finite element analysis that accounts for Hill's yielding. The mean maximum load sustained by the beams in experimental bending tests was 69.1 N. The model that used the tension modulus, Hill's yield constants, and the plastic hardening curve derived from the tension tests over-predicted the bending stiffness by 17% in the linear-elastic range. However, the simulated beam section withstood a maximum load of 52.8 N, which was 24% lower than the loads observed during the mechanical tests.

The model that used the compression modulus, and yield parameters derived from compression tests predicted the maximum load on the beam section at a higher load of 79.4 N, which was 15% higher than the mean experimental maximum load. However, the stiffness predicted by the model was lower by 17% in the linear-elastic range compared to the experimental results. The displacement at the maximum

load was higher by 12% compared to the mean displacement at maximum loads obtained from the experimental data.

The model that accounted for the bimodular nature of the material and different yielding behavior in tension and compression predicted the maximum load of the beam section at a load of 67.3 N. The model also under-predicted the stiffness in the linear-elastic range by 1.8% compared to the experimental data. Among the three finite element models used, the load-displacement curve obtained from this model was closest to the experimental data.

A moment-curvature based method for predicting the failure load has been discussed in Appendix A1. The moment-curvature based method predicted a maximum load of 63.6 N which is 8.0% lower than the mean experimental ultimate loads of 69.1 N.The relevant MATLAB script for the moment-curvature analysis has been presented in Appendix A2.

A simple strain-based failure criteria is discussed in Appendix A1. The material is assumed to fail if it reaches a tensile strain of 1.72 % in the 1-direction. The simple strain-based failure criteria predicts first failure at 35.7 N at a displacement of 6.60 mm. The second failure is observed at 51.1 N at a displacement of 13.2 mm. The failure load and failure displacement predicted by this simple failure criteria is significantly lower than the experimental observations of mean failure loads of 69.1 N and mean failure displacements of 27.1 mm.

The early yielding and the lower maximum load are predicted by the model with material properties based on tension tests because the material input properties based on the tension tests have lower yield stresses compared to those based on the compression tests. Similarly, the higher bending stiffness at lower load is predicted by the model with material properties based on the tension tests because the tensile Young's modulus is higher compared to the compressive Young's modulus. Since the bottom

fibers of the beam are in tension and the top fibers are in compression, the results predicted by the model considering the bimodular nature of the material are closest to the experimental results.

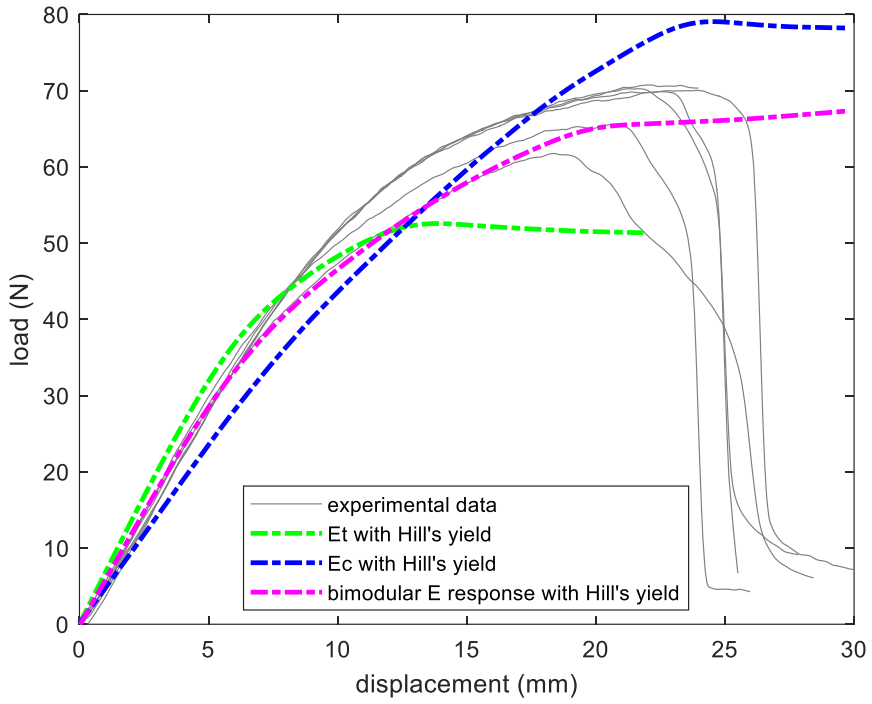

Figure 23: Load vs displacement obtained from the bending experiments and the bending finite elements model with three different material-modulus-considerations and Hill's yielding.

The mesh convergence plot for the bending test finite element model with bimodular elasticity and Hill's yielding is shown in Figure 24.

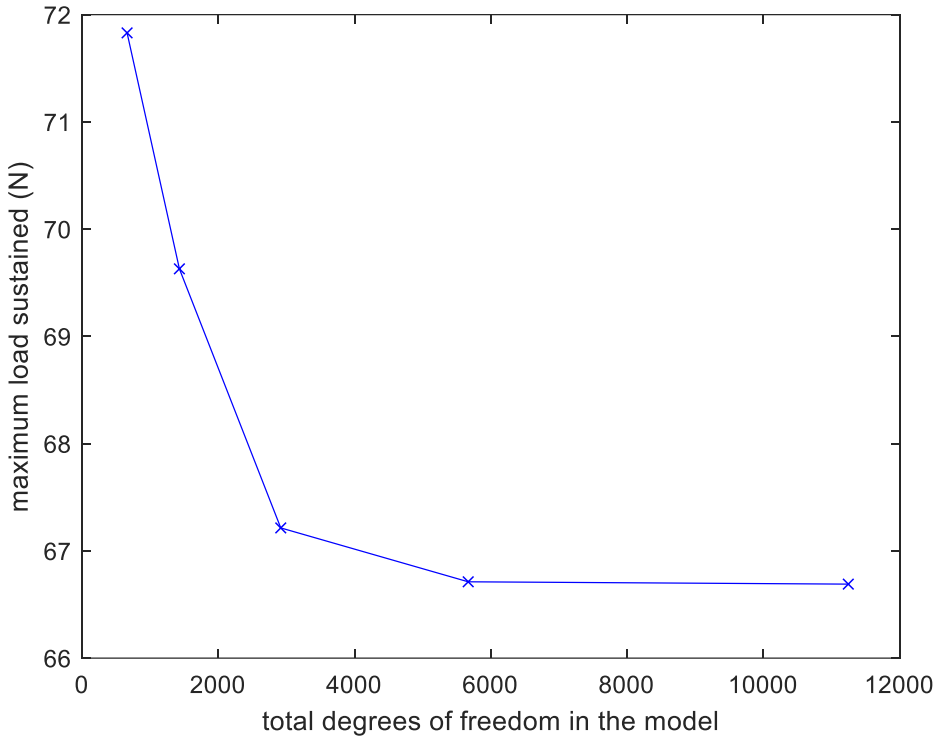

Figure 24: Mesh convergence for bending test finite element model.

3.5 Conclusions

This study extends the existing CLT-based linear-elastic finite element models to 3D printed composites to address the bimodular and elasto-plastic yielding behavior observed in these materials.

The following conclusions have been made:

1. A laminate analysis-based finite element modeling method only approximates the linear portion of the stress-strain behavior of the 3D printed composite under tensile loading.
2. An elasto-plastic finite element model with Hill's yield criterion was effective in predicting the overall stress-strain response of the 3D printed composite under tensile loading.
3. A linear elastic finite element analysis based on bimodular behavior was effective in predicting the load-displacement response under three-point bending for the laminate.

4. The bimodular behavior of the material needs to be considered to effectively predict the bending behavior of a 3D printed part.

Future work should involve reducing analysis time. The finite element analysis takes considerable time (about two hours) to complete. The main reasons for the slow analysis speed are the use of an explicit solver with time steps of about 10^{-6} seconds, and the unsymmetric stiffness matrix that arises due to the bimodularity of the material. The stress-strain relationships are calculated up to three times for each time step for each element. A model using an implicit solver should be considered. The effect of using a symmetric matrix on accuracy can be studied. Future work also should involve extending the material model to include 3D geometries. The complex geometry parts should be sub-divided into regions with different orientations. The process of experimentally generating material properties in the three mutually perpendicular material directions and transforming the material properties based on the orientation of the material can be extended to 3D geometries. The 3D geometry can be sub-divided into regions of same orientation to generate material properties for the sub-divided regions. Alternatively, the material properties for a given orientation can be generated at the mesh level for each element.

CHAPTER 4
DISCRETE-EVENT SIMULATION FOR GENERATING THERMAL HISTORY OF 3D PRINTED ABS AND PLA

4.1 Chapter abstract

Material properties of thermoplastic polymer parts manufactured by the extrusion-based additive manufacturing process are highly dependent on its thermal history. Different numerical models have been proposed to simulate the thermal history of a 3D-printed part. However, they are limited attributable to limited geometric applicability, low accuracy, or high computational demand. This paper describes the numerical implementation of a simplified discrete event simulation model that offers accuracy comparable to the finite element model but is faster by two orders of magnitude. Two polymer systems with distinct thermal properties were selected to highlight differences in the simulation of the orthotropic response and the temperature-dependent material properties. The time-temperature histories from the numerical model were compared to the time-temperature histories from a conventional finite element model and were found to match closely. The proposed highly parallel numerical model was about 300-500 times faster in simulating thermal history compared to the conventional finite element model. The model would enable designers to compare the effects of several printing parameters for specific 3D printed parts and select the most suitable parameters for the part.[3]

[3] The research work presented in this chapter has been published as:
Bhandari, S.; Lopez-Anido, R.A. Discrete-Event Simulation Thermal Model for Extrusion-Based Additive Manufacturing of PLA and ABS. Materials 2020, 13, 4985. https://doi.org/10.3390/ma13214985

4.2 Introduction

Extrusion-based additive manufacturing of thermoplastic polymers is a thermally driven process. Thermal history affects the viscoelastic deformation [89, 134, 135], the bonding [58, 68, 136-138], and the residual stresses [84, 139]. Consequently, dimensional accuracy and the strength of the manufactured part are driven by the thermal history of the part.

Wang et al. analyzed the strength and weaknesses of different polymer-based additive processes including extrusion-based additive manufacturing. Tan et al. reviewed the state of the art of commodity, engineering, and high-performance polymers used in additive manufacturing. A polymer undergoes melting, thermal transitions, and solidification during the extrusion-based additive manufacturing process. Tan et al. highlighted the different mechanical, rheological, and thermal properties that affect the additive manufacturing processability and the 3D printed part properties. A growing number of polymers have been successfully used in the extrusion-based additive manufacturing process. Initially amorphous polymers were preferred for additive manufacturing including ABS (acrylonitrile butadiene styrene) , PETG (polyethylene terephthalate glycol) [138, 140], and[138, 140], PC (polycarbonate) [141-143]. The thermal and rheological properties of semi-crystalline polymers caused difficulties in filament production and showed higher shrinkage and warping during the 3D printing process [144, 145]. PLA (polylactic acid) , despite being a semi-crystalline polymer, is widely used in extrusion-based additive manufacturing as the PLA crystallizes slowly and consequently shrinks and warps less than other typical semi-crystalline 3D printed polymer parts. Recently, however, several semi-crystalline polymers like PA (polyamides) , PEEK (polyether ether ketone) , and PP (polypropylene) have been used for extrusion-based 3D printing process. Suitable numerical models enable designers to account for the different properties of the polymers during the 3D printing process and optimize the design of 3D printed parts .

Different numerical models have been proposed by researchers to simulate the thermal history of 3D printed parts. Sun et. al. used a mathematical model to approximate the temperature of 3D printed parts to model the bond forming between ABS (acrylonitrile butadiene styrene) filaments. Wang et. al. used a simplified mathematical model to simulate the temperature and the subsequent warp deformation in extrusion-based 3D printed ABS parts. These simplified layer-by-layer models have low accuracy and the results can only be interpreted qualitatively.

Compton et. al. discussed a 1D transient thermal model to describe a build process and analyze warping and cracking in thin-walled structures. The thermal model was solved by using a finite difference method that calculated the temperature at the nodes at each timestep. Zhang et. al. used an adaptable, boundary adjusting finite difference method to simulate the thermal history of a 3D printed PLA (polylactic acid) part. Stockman et al. presented a thermal model tailored for additive manufacturing that was based on the 3D finite difference method. The researchers used coarse meshing in time and space along with simplifying assumptions about the solidification process. The finite difference scheme-based models work well for simple geometries like thin layered walls and rectangular cuboids. However, for more complex geometry parts that extrusion-based 3D printing usually produces, a method that can account for changes in geometry is necessary.

Finite element analysis (FEA) modeling has been used to simulate the thermal history of 3D printed parts with complex geometry. Ji and Zhou used a finite element model that accounted for temperature-dependent material properties. D'Amico and Peterson described an adaptable FEA model capable of simulating heat transfer in 3D and at sufficiently small time scales to capture rapid cooling. El Moumen et. al. discussed a 3D thermo-mechanical model that simulates the 3D printing process using FEA. Zhou et. al described a finite element based on element activation to model the thermal history of a 3D printed part. Zhou et. al described a voxelization-based finite element simulation to simulate the

thermal history of 3D printed parts. Brenken et al. used FEA modeling to simulate the thermal history, final deformed shape, and residual stresses in the 3D printed short carbon fiber reinforced ABS polymer. Finite difference methods and finite element methods solve systems of linear equations for each timestep during the period of simulation. Such models slow down non-linearly as the size of the part to be simulated grows.

Heat flow through a body in form of a partial differential equation is shown in Equation 4.1. The finite element methods and the finite difference methods approximate a solution to the heat equations at discrete locations by solving a system of linear equations.

$$\rho c_p \frac{\partial T}{\partial t} - \left(\frac{\partial}{\partial x} k_x \frac{\partial}{\partial x} + \frac{\partial}{\partial y} k_y \frac{\partial}{\partial y} + \frac{\partial}{\partial z} k_z \frac{\partial}{\partial z}\right) T = Q \tag{4.1}$$

where,

ρ	=	density
c_p	=	specific heat capacity
T	=	temperature
k_x, k_y, k_z	=	conductivity in the x, y, and z directions respectively
Q	=	heat flow

During 3D printing, the boundary of the part changes with each new deposition of beads. As a result, the finite element methods and the finite difference methods need to update the heat capacity matrix, conductivity matrix, and the boundary conditions at each timestep. Furthermore, nonlinearities like temperature-dependent conductivities and specific heat capacities require an iterative solution of the system of linear equations at each timestep. As a result, a system of linear equations-based solution to the heat equation is slow and computationally expensive for simulating heat transfer in the 3D printing process. Some simplifications have been proposed for speeding up the simulations. McMillian et al.

reduced the 3D model to a 1D model by using geometric simplifications to create a computationally efficient finite difference method for metal additive manufacturing. Zhang and Shapiro proposed a linear-time thermal simulation of as-manufactured fused deposition modeling components. They used the concept of "active body" to update the temperatures only in the elements that have been recently activated and using analytical equations to solve the temperature of "inactive" elements with "lazy updates". The research work considered the thermal properties of ABS as constants for the simulation.

A phenomenological approach has been adopted in this paper to develop the thermal model for extrusion-based additive manufacturing. The phenomenological observations are:

The geometry of the part changes rapidly during 3D printing. For desktop scale printing on extrusion-based 3D printing, bead deposition speed of 30-60 mm/s is commonly used [146]. It amounts to a material deposition rate of 30-60 cm^3/hr. For large-scale 3D printers, the deposition rates can reach 230 cm^3/hr [147]. The high rate of deposition continuously changes the geometry of the 3D-printed parts.

Heat flow from one region of a part to another region of the same part is not instantaneous, i.e., heat transfer takes time. Polymers have low thermal diffusivity, which is a measure of the rapidity of heat propagation through a material .

Belleheumer et. al [86] observed that the time taken by the beads to cool down to ambient temperature is short compared to the overall time taken to print the whole part. Zhang and Shapiro [148] observed that the deposition in a layer that is far away from an element has a negligible effect on the thermal history of the element. Based on the aforementioned observations, a solution to the heat transfer problem that examines the local exchange of heat between neighboring regions at small timesteps can be formulated. This research work treats the deposition of a small bead of material as a discrete event. At small timesteps, the deposited section of the bead exchanges heat with its immediate

neighbor via conduction, convection, or radiation. Temperature is considered static for the elements in a layer that are far away from the layer being actively deposited.

The objectives of the research presented herein are listed below.

1. A model that meets these objectives would allow designers to quickly compare the effects of different printing parameters on the thermal history of 3D printed parts and allow to select the most suitable printing parameter for a given part.
2. Develop an efficient numerical model for thermal discrete event simulation (DES) that generates the part geometry and mesh by interrogating the G-code, and uses parallel computation for fast analysis of extrusion-based additive manufacturing.
3. Simulate material orthotropy in 3D printed parts by using the information on the orientation of deposited beads from the G-code.
4. Capture the temperature-dependent response of the material in the simulation of the thermal behavior of 3D printed polymers.
5. Verify the accuracy of the proposed numerical model by comparing it with results from a finite element model using a commercial FEA package (Abaqus).

4.3 Materials and methods

4.3.1 Materials

PLA and ABS were selected for the study. The polymers were chosen because they are widely used polymers used in extrusion-based 3D printing processes and represent two classes of polymers used in additive manufacturing, i.e., semi-crystalline and amorphous. PLA is a semi-crystalline material with

specific heat capacity dependent on temperature, with sharp changes at melting, cold crystallization, and glass transition temperatures [149, 150]. ABS is an amorphous polymer with a fairly constant specific heat capacity [151]. Differential scanning calorimetry carried out during a previous study [138] was used for the specific heat capacity of PLA.

4.3.2 Numerical model

The following assumptions were used for the numerical model:

- Heat exchange occurs between neighboring elements only, for a small timestep.
- The effect of radiation is not considered.
- Contact resistance is not considered in calculations involving thermal conductivity.

Figure 25 shows the flowchart of the numerical model developed for this study.

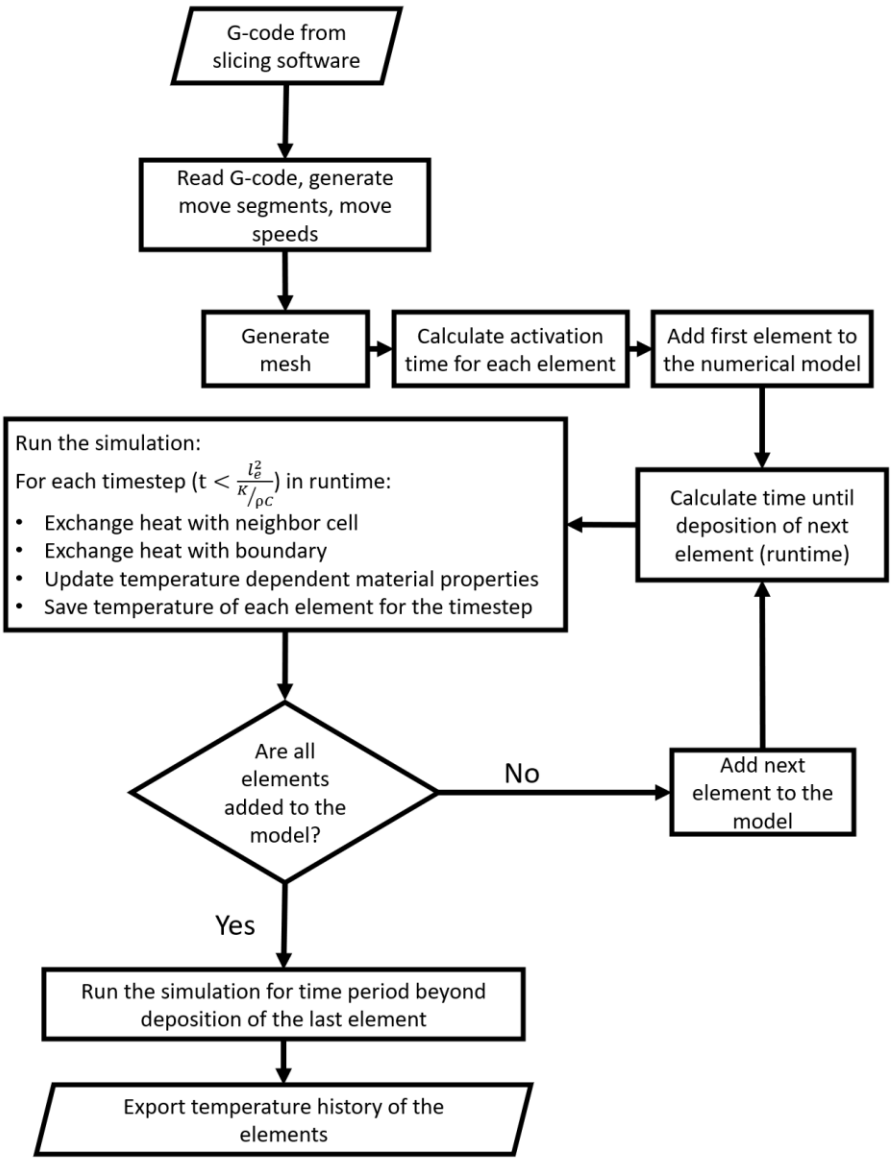

Figure 25: Flowchart of the numerical model used in the study.

The model takes the G-code from the slicing software as input. G-code is the sequence of machine instructions that directs the actions of the 3D printers. G-code is generated by slicing software using the geometrical model and the printing parameters as input. For this study, Simplify3D was used for slicing the geometrical model. Simplify3D was used because it is a widely used slicing software, it enables modification of different printing parameters, and it allows for the visualization of the printing process.

The model reads the G-code and generates the movement segments, the speed of movement for each segment, and whether the extrusion is on for each segment. Table 9 shows the conversion of a section of G-code output to a movement segment. X, Y, and Z are the G-Codes for the absolute position of the X, Y, and Z-axis. G1 is the G-Code instruction for linear interpolation. F is the G-Code for setting extruder speed [152]. Each movement segment consists of an initial point, a final point, movement speed, and information about whether extrusion occurs for the segment.

Table 9: Conversion from G-code to movement segment.

G-code	Movement segment							
	X1 (mm)	Y1 (mm)	Z1 (mm)	X2 (mm)	Y2 (mm)	Z2 (mm)	speed (mm/min)	extrusion
G1 X0 Y0 F4800								
G1 Z0.400 F1002	0.000	0.000	0.000	0.000	0.000	0.400	1002	off
G1 X89.347 Y89.347 F4800	0.000	0.000	0.400	89.347	89.347	0.400	4800	off
G1 X110.653 Y89.347 E2.8347 F1300	89.347	89.347	0.400	110.653	89.347	0.400	1300	on
G1 X110.653 Y110.653 E2.8347	110.653	89.347	0.400	110.653	110.653	0.400	1300	on

In Table 9, X1, Y1, and Z1 are the coordinates of the initial point of the movement segment. X2, Y2, and Z2 are the coordinates of the final point of the movement segment. The coordinates are absolute coordinates with reference to the machine axes of the 3D printer. Figure 26 shows the movement segment with the reference axis to the machine axes. The initial point of the segment is marked as (X1, Y1, Z1) and the final point of the segment, where the printer toolhead is located, is marked as (X2, Y2, Z2).

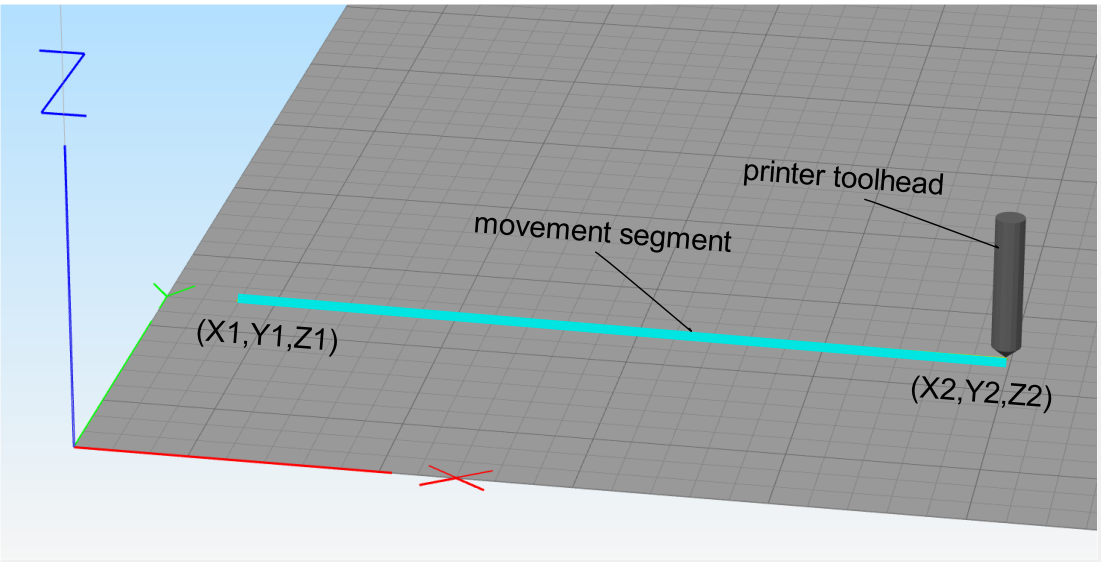

Figure 26: Movement segment coordinates with reference to machine axes.

The mesh for this model has extra information than it is not available in typical meshes used in the finite element models. In the finite element models, the mesh used has nodes defining the coordinates, and connectivity defining the elements. The mesh used for this study has, in addition to nodes and connectivity, the information about adjoining elements, called neighbor information for this study. For an element, the information about whether the faces are exposed to the boundary or connected to another element is the neighbor information for that element. For this study, hexahedral elements (brick elements) were considered with six faces. Figure 27 shows a configuration of elements in relation to their neighbors. Element 0 is hidden in Figure 27 on the left. Figure 27 on the right is an exploded view of Figure 27 on the left so that each element in the mesh can be viewed. For element 0, which is at the center, the neighbors at the front and the back are elements 1 and 2 respectively. Similarly, the neighbors at right, left, top, and bottom are 4, 3, 5, and 6 respectively. Element 0 exchanges heat with elements 1, 2, 3, 4, 5, and 6 via conduction (and radiation if radiation is considered). Element 0 does not have any face exposed to the boundary and does not exchange heat with the environment via convection. Considering element 2, its only neighbor is element 0 at the front face. Element 2 exchanges

heat with element 0 via conduction. Element 2 loses heat to the environment via convection (and radiation if radiation is considered) through the back, left, right, top, and bottom surfaces.

The neighbor information changes with each new element deposited and needs to be updated once an element is deposited.

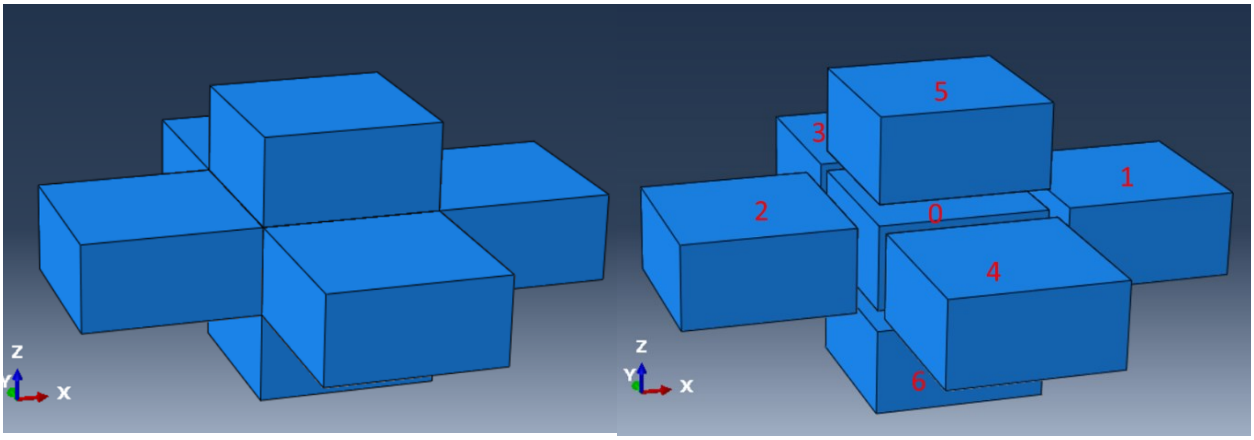

Figure 27: A configuration of elements showing neighbors.

Based on the deposition path, deposition time is generated for each element. Figure 28 shows the process for calculation of the element deposition time and the element orientation. Each movement segment is divided into points. The points mark the physical location of the deposition head during the 3D printing process. The points are created in a way that ensures that the spacing between two consecutive points is length less than the length of an element. The time at which the movement head is at each point is calculated t_p. In Figure 28 d), the red dots mark the movement of the deposition head. A square box with a width equal to the bead width, as shown in Figure 28 d, is used to find elements that are deposited. If the center of the element is inside the square box, the element is considered deposited and the deposition time for the element is t_p. The orientation of the element is calculated as the unit vector representing the movement segment. Element 0 is deposited at time t_0, and element 1 is deposited at time t_3.

The choice of the element dimensions is made such that the process of bead deposition can be simulated correctly. Each element has a length and width equal to the bead width of the 3D printed part. The height of the element equals the bead height of the 3D printed part.

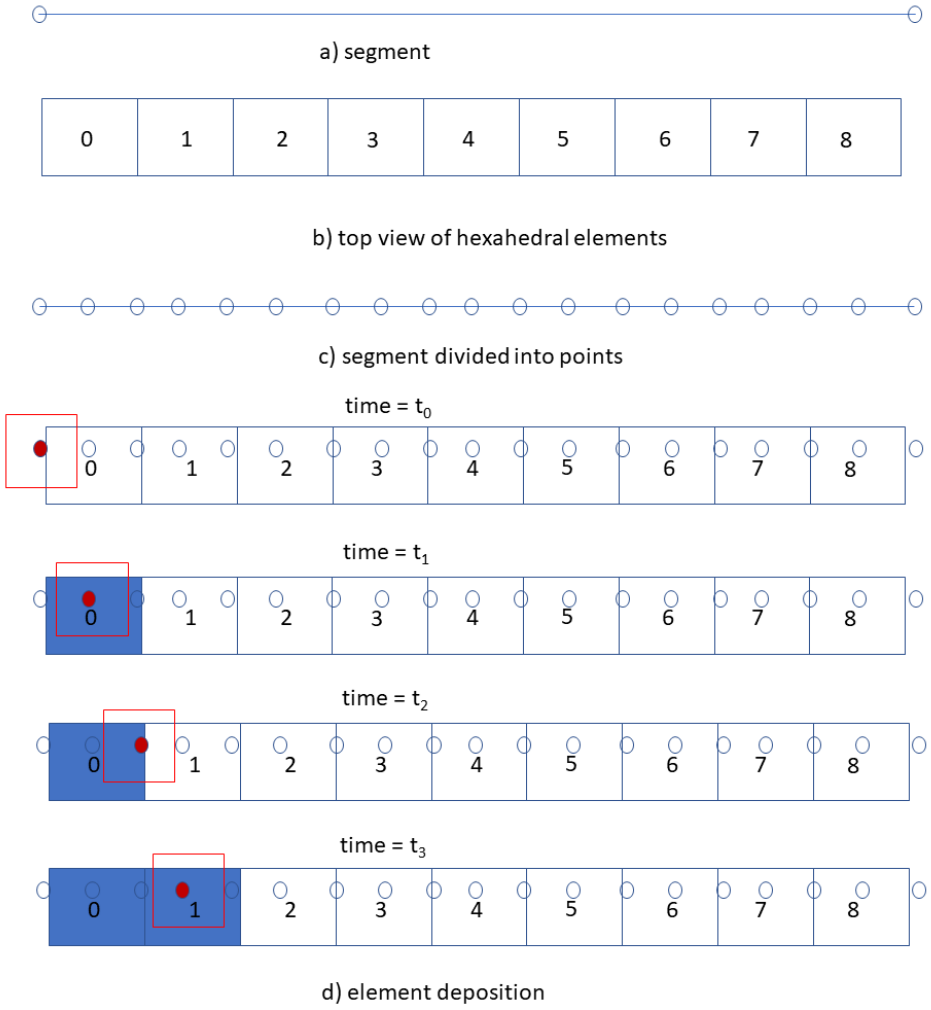

Figure 28: Calculation of element deposition time and orientation.

After the deposition time for all the elements have been calculated, the first element is added to the numerical model. The first element has a conductive boundary at the bottom face and convective boundary at the front, back, right, left, and the top faces. Until the time when the next element is deposited, for a time increment *dt*, heat losses to the environment attributable to convection are calculated using Equation 4.2.

$$dQ = h \,.\, A \,.\, (T - T_{env}) \,.\, dt \tag{4.2}$$

where,

dQ	=	heat loss to environment via convection
h	=	convective heat transfer coefficient
A	=	area of the surface exposed to the environment
T	=	temperature at the centroid of element
T_{env}	=	temperature of the environment at bordering the surface
dt	=	time increment

After adding the next element to the model, the neighbor information is updated for all the elements in the model. Conduction of heat from one element to the other is calculated using Equation 4.3.

$$dQ = k.A.\frac{(T_1 - T_2)}{dx}.dt \tag{4.3}$$

where,

dQ	=	heat conducted to another element
k	=	conductivity
A	=	area of the conducting surface
T	=	temperature at the centroid of element
T_{env}	=	temperature of the environment at bordering the surface
dt	=	time increment

Sum of heat exchanges through all surfaces and the new temperature of the element is calculated using Equations 4.4-4.8.

$$dQ_{total} = \sum dQ \tag{4.4}$$

$$Q_{old} = T_{old}.\rho.C_{old.}V \tag{4.5}$$

$$Q_{new} = Q_{old} - dQ_{total} \tag{4.6}$$

$$T_{new} = \frac{Q_{new}}{\rho.C_{new}.V} \tag{4.7}$$

Assuming $C_{new} \approx C_{old}$

$$T_{new} = \frac{Q_{new}}{\rho.C_{old}.V} \tag{4.8}$$

where,

dQ_{total}	=	total heat change from all surfaces
Q_{old}	=	total heat in the element during previous timestep
T_{old}	=	temperature at the centroid of the element during the previous timestep
ρ	=	density of the element material
C	=	specific heat capacity of the element material at the old temperature
V	=	volume of the element
dt	=	time increment
Q_{new}	=	total heat in the element during this timestep
T_{new}	=	temperature at the centroid of the element after current timestep
C_{new}	=	specific heat capacity of the element after this timestep

Equation 4.7 is iterative and uses specific heat capacity versus temperature data for the element. Mass (volume times density) is assumed to be constant during the process. Assuming small time steps and to get the non-iterative Equation 4.8.

Equation 8 shows the heat transferred through six different faces. The heat exchanged by an element with its neighbors is calculated using Equation 4.8. Equation 4.8 accounts for heat transferred via conduction. If any of the faces of the element is exposed to the environment, Equation 4.2 is used to account for heat exchange with the environment via convection for that face.

$$\begin{Bmatrix} dQ_f \\ dQ_l \\ dQ_b \\ dQ_r \\ dQ_t \\ dQ_d \end{Bmatrix} = \begin{bmatrix} k_{xx} & 0 & 0 & 0 & 0 & 0 \\ 0 & k_{yy} & 0 & 0 & 0 & 0 \\ 0 & 0 & k_{xx} & 0 & 0 & 0 \\ 0 & 0 & 0 & k_{yy} & 0 & 0 \\ 0 & 0 & 0 & 0 & k_{zz} & 0 \\ 0 & 0 & 0 & 0 & 0 & k_{zz} \end{bmatrix} \begin{Bmatrix} \frac{T - T_f}{dx} A_f \\ \frac{T - T_l}{dy} A_l \\ \frac{T - T_b}{dx} A_b \\ \frac{T - T_r}{dy} A_r \\ \frac{T - T_t}{dz} A_t \\ \frac{T - T_d}{dz} A_d \end{Bmatrix} dt \tag{4.8}$$

where,

$dQ_f, dQ_l, dQ_b, dQ_r, dQ_t, and\ dQ_d$ = heat exchange with the element connected to the front, left, back, right, top, and down faces respectively

$T_f, T_l, T_b, T_r, T_t, and\ T_d$ = the temperature of elements connected to the front, left, back, right, top, and down faces respectively

dx, dy, and dz	=	distance between the centroids of connected elements in the x, y, and z directions
$A_f, A_l, A_b, A_r, A_t, A_d$	=	contact area with the element connected to the front, left, back, right, top, and down faces respectively
dt	=	timestep

Considering front and back faces, the faces in the global x-direction, and $A_b = A_f = A_x$, $A_l = A_r = A_y$, $A_t = A_d = A_z$ for hexahedral elements used in this study, Equation 4.9 can be formed.

$$dQ = dQ_f + dQ_b + dQ_r + dQ_l + dQ_t + dQ_d$$

$$dQ = \left(k_{xx}\frac{T - T_f}{dx}.A_x + k_{xx}\frac{T - T_b}{dx}A_x + k_{yy}\frac{T - T_l}{dy}y + k_{yy}\frac{T - T_r}{dy}A_y + k_{zz}\frac{T - T_t}{dz}A_z + k_{zz}\frac{T - T_d}{dx}A_z\right)dt$$

$$dQ = \left(k_{xx}(\frac{-T_b + 2T - T_f}{dx})A_x + k_{yy}(\frac{-T_l + 2T - T_r}{dy})A_y + k_{zz}(\frac{-T_t + 2T - T_d}{dz})A_z\right)\ dt \qquad (4.9)$$

Substituting Equation 9 in Equation 7, Equation 4.10 can be formed and reduced to Equation 4.11 which is equivalent to the forward time center space (FTCS) finite difference scheme for heat equation .

$$\rho.C_{new}.V.T_{new} = \rho.C_{old}.V.T_{old} - \left(k_{xx}\left(\frac{-T_b + 2T - T_f}{dx}\right)A_x + k_{yy}\left(\frac{-T_l + 2T - T_r}{dy}\right)A_y + k_{zz}\left(\frac{-T_t + 2T - T_d}{dz}\right)A_z\right)\ dt \qquad (4.10)$$

$$T_{new} = \frac{C_{old}}{C_{new}}.T_{old} + \frac{1}{\rho.C_{new}}\left(k_{xx}\left(\frac{T_b - 2T + T_f}{dx^2}\right) + k_{yy}\left(\frac{T_l - 2T + T_r}{dy^2}\right) + k_{zz}\left(\frac{T_t - 2T + T_d}{dz^2}\right)\right)dt \qquad (4.11)$$

The temperature of each active element in the model is updated using the procedure described in Equations 2-7. When an element is added to the model, the neighbor information is updated to define the new boundary conditions. If an element is in a layer far away from the element just deposited, the far away element is made inactive. Temperature is not updated for inactive elements in the model. For this study, a 30-layer distance was considered far, and elements more than 30 layers away from the element currently being deposited were made inactive. Figure 29 shows the changing neighbors with the addition of elements to the model. At time t = t_1, element 1 has all faces exposed to the environment. At time t = t_2, element 2 is added with neighbor element 1 at its back. The neighbor information of element 1 is also updated to such that element 2 is at the front of the element 1.

A stable time increment for a uniform grid in finite difference methods with forward Euler integration is given by Equation 4.11 [153].

$$\Delta t < \left(\frac{\Delta x^2}{2\alpha}\right) \tag{4.11}$$

where,

α = $\frac{K}{\rho . C}$

Δx = distance between the nodes

Orthotropy in conductivity of the 3D printed material due to different conductivities along the bead and across the beads is considered. The conductivity matrix transformation from local system to global system is shown by Equation 4.12.

$$[K]_G = [T]^T[K]_l[T] = \begin{bmatrix} c & -s & 0 \\ s & c & 0 \\ 0 & 0 & 1 \end{bmatrix} \begin{bmatrix} k_{xx} & 0 & 0 \\ 0 & k_{yy} & 0 \\ 0 & 0 & k_{zz} \end{bmatrix} \begin{bmatrix} c & s & 0 \\ -s & c & 0 \\ 0 & 0 & 1 \end{bmatrix} = \begin{bmatrix} k_{xx}c^2+k_{yy}s^2 & cs(k_x - k_y) & 0 \\ cs(k_x - k_y) & k_{yy}c^2+k_{xx}s^2 & 0 \\ 0 & 0 & 1 \end{bmatrix} \quad (4.12)$$

where,

$[K]_G$	=	conductivity matrix in global system (machine axes)
$[K]_l$	=	conductivity matrix in local system
$[T]$	=	transformation matrix
c	=	cosine of bead deposition orientation to machine X-axis
s	=	sine of bead deposition orientation to machine X-axis
k_{xx}	=	in-plane conductivity along the deposition of the bead
k_{yy}	=	in-plane conductivity perpendicular to the deposition of the bead
k_{zz}	=	out-of-plane conductivity in the machine Z-axis

Equation 4.13 shows the heat transferred from the faces of an element via conduction for an orthotropic material.

$$\begin{Bmatrix} dQ_f \\ dQ_l \\ dQ_b \\ dQ_r \\ dQ_t \\ dQ_d \end{Bmatrix} = \begin{bmatrix} k_{xx}c^2+k_{yy}s^2 & \frac{1}{2}cs(k_x - k_y) & 0 & \frac{1}{2}cs(k_x - k_y) & 0 & 0 \\ \frac{1}{2}cs(k_x - k_y) & k_{yy}c^2+k_{xx}s^2 & \frac{1}{2}cs(k_x - k_y) & 0 & 0 & 0 \\ 0 & \frac{1}{2}cs(k_x - k_y) & k_{xx}c^2+k_{yy}s^2 & \frac{1}{2}cs(k_x - k_y) & 0 & 0 \\ \frac{1}{2}cs(k_x - k_y) & 0 & \frac{1}{2}cs(k_x - k_y) & k_{yy}c^2+k_{xx}s^2 & 0 & 0 \\ 0 & 0 & 0 & 0 & k_{zz} & 0 \\ 0 & 0 & 0 & 0 & 0 & k_{zz} \end{bmatrix} \begin{Bmatrix} \frac{T - T_f}{dx} A_f \\ \frac{T - T_l}{dy} A_l \\ \frac{T - T_b}{dx} A_b \\ \frac{T - T_r}{dy} A_r \\ \frac{T - T_t}{dz} A_t \\ \frac{T - T_d}{dz} A_d \end{Bmatrix} dt \quad (4.13)$$

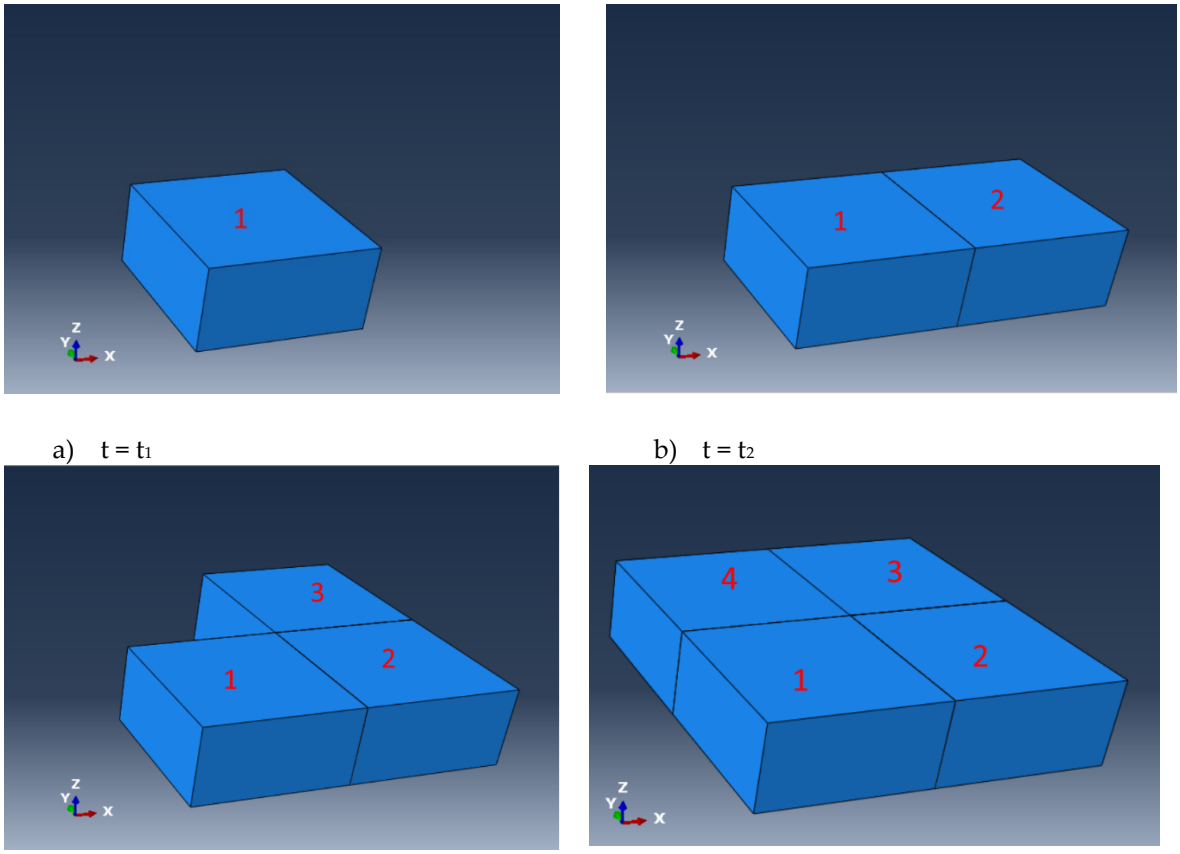

a) $t = t_1$ b) $t = t_2$

c) $t = t_3$ d) $t = t_4$

Figure 29: Changing neighbor information with the addition of elements to the model.

The neighbor information is updated similarly for the addition of element 3 and element 4 as shown in Table 10. In Table 10, the term env denotes that the face under consideration does not have any neighbor and is exposed to the ambient conditions of the environment.

Table 10: Neighbor information for cells with the addition of new elements at each timestep.

Timestep	Elements	Front	Back	Right	Left	Top	Bottom
$t = t_1$	1	env	env	env	env	env	env
$t = t_2$	1	2	env	env	env	env	env
	2	env	1	env	env	env	env
$t = t_3$	1	2	env	env	env	env	env
	2	env	1	env	3	env	env
	3	env	env	2	env	env	env

$t = t_4$	1	2	env	env	4	env	env
	2	env	1	env	3	env	env
	3	env	4	2	env	env	env
	4	3	env	1	env	env	env

Once all the elements have been deposited, the model is allowed to run for a specified period of time to simulate the cooling down of the 3D printed part. The time-temperature data for each element is exported to a file. Rust programming language was used for discrete event simulation due to its speed, automatic memory management without use of garbage collector, and safe concurrency. Abaqus 2020 and its 3D printing module was used for thermal finite element modeling.

4.3.3 Part geometry, printing parameters, G-code generation, and inputs for DES model

A solid modeling computer-aided design software (SolidWorks) was used for generating the geometry of the 3D printed part. A miniature geometry ashtray model as used by Zhou et. al [154] was used for the study. The geometry was considered complex enough to showcase the effects of 3D printing. The STL file was created using SolidWorks. Simplify3D software was used for slicing and generating the G-code toolpath. Figure 30a shows the 3D model of the STL file imported into simplify3D software. The part has a diameter of 48.8 mm and a height of 12.7 mm. Figure 30b shows the deposition path for the 3D printed part.

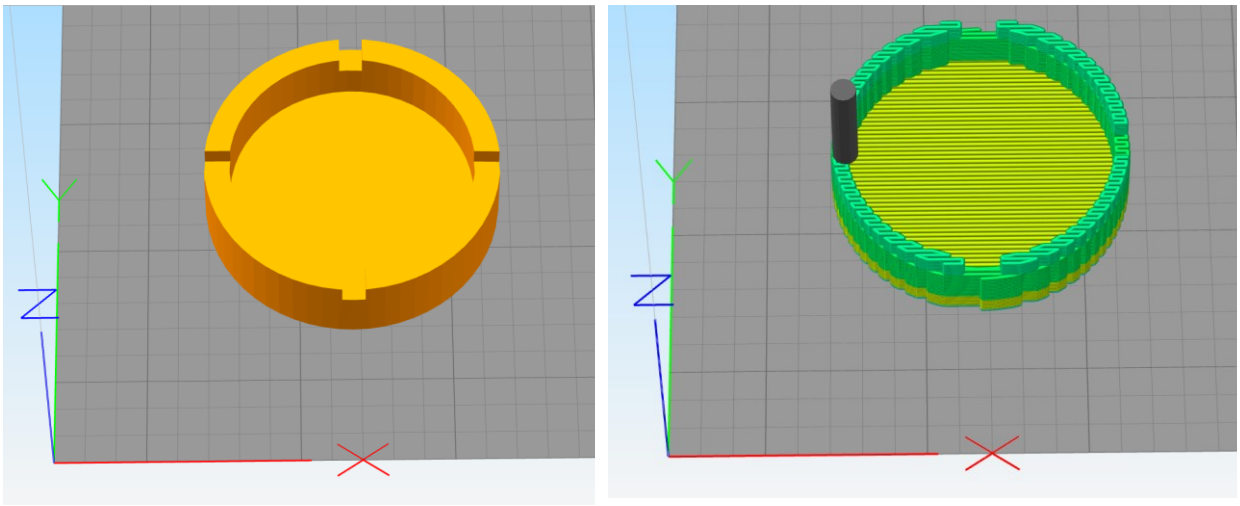

a) 3D model of the part. *b) Printing path for the part.*

Figure 30: 3D model and printing path for the 3D printed part.

The printing parameters used for this study are listed in Table 11.

Table 11: Printing parameters used for the study.

Parameter	Value
Beadwidth	0.8 mm
Beadheight	0.4 mm
Movespeed	90 mm/s
Deposition speed	60 mm/s
Infill angle	0°
Deposition temperature	200°C for PLA, 210°C for ABS
Infill percentage	100 %
First layer speed	12 mm/s

A temperature of 25°C was used as environmental temperature. A convective heat transfer coefficient of 100 $W \cdot m^{-2} \cdot K^{-1}$ was assumed for this study.

Table 12: Thermal properties used for the PLA material during finite element analysis.

Property	Value
Density, ρ	1240 kg/m^3 [155]
conductivity in the x-direction, k_{xx}	0.25 W·m^{-1}·K^{-1} [156]
conductivity in the y-direction, k_{yy}	0.2 W·m^{-1}·K^{-1}
conductivity in the z-direction, k_{zz}	0.2 W·m^{-1}·K^{-1}

Specific heat capacities for PLA as a function of temperature is shown by the peaks and valleys in Figure 31. Specific heat capacity of PLA changes rapidly at glass transition temperature at around 55°C, at cold crystallization temperature around 120°C, and at melting point around 150°C.

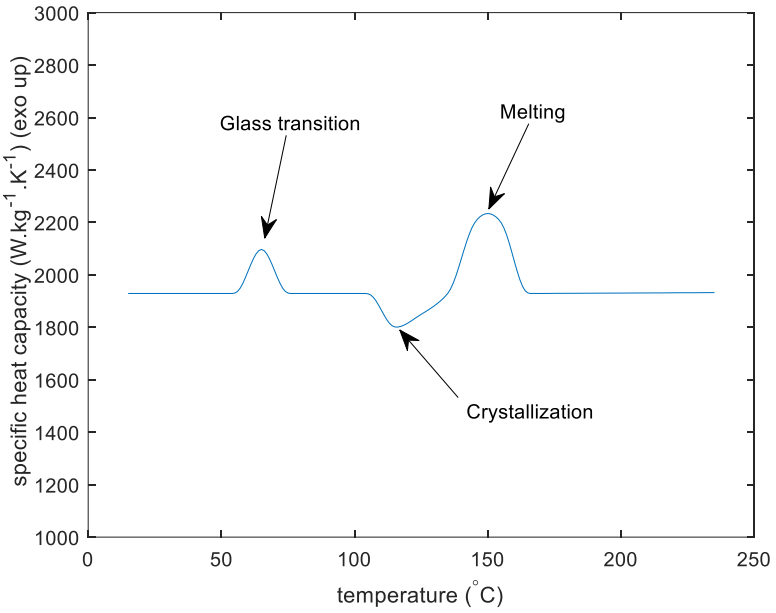

Figure 31: Specific heat capacity of PLA vs temperature.

Table 13 shows the thermal properties used for ABS material during finite element analysis. The thermal properties are taken from publication by Zhou et al.

Table 13: Thermal properties used for ABS material during finite element analysis [154].

Temperature (°C)	**Thermal conductivity** (W·m^{-1}·K^{-1})	**Specific heat capacity** (J·kg^{-1}·K^{-1})	**Density** (kg·m^{-3})
0	0.23	780	1050
50	0.25	1040	1050
100	0.28	1490	1050
150	0.29	1710	1050
200	0.31	1865	1050
250	0.33	2020	1050

For a grid of 0.8mm x 0.8mm x 0.4mm, with K = 0.20 W·m^{-1}·K^{-1}, $\rho = 1240$ kg·m^{-3}, and $C = 1400$ J·kg^{-1}·K^{-1}, a stable time increment for PLA was calculated as 0.6944 seconds.

For a grid of 0.8mm x 0.8mm x 0.4mm, with K = 0.33 W·m^{-1}·K^{-1}, $\rho = 1050$ kg·m^{-3}, and $C = 780$ J·kg^{-1}·K^{-1}, a stable time increment for ABS was calculated as 0.1985 seconds.

For both cases, a timestep of 0.01 seconds was chosen for the DES model. The maximum time increment that can be used for the DES model is the time required to deposit an element. The effect of smaller time increments on the results was studied by using four different timesteps of 0.01 seconds, 0.005 seconds, 0.0025 seconds, and 0.00125 seconds.

4.3.4 Finite element modeling using Abaqus with AM modeler plugin

Abaqus 2020 with AM modeler plugin was used for the finite element analysis of the part. A cuboid with a length of 50.4 mm, a width of 50.4 mm, and a height of 13.2 mm was created. An 8-node hexahedral mesh (DC3D8) was created, where each element had a length and a width of 0.8 mm and a height of 0.4 mm. The width and height of the elements matched the width and height of the deposited beads. A total of 34071 elements were deposited in the final part during the analysis. Homogenous solid with orientation matching the print direction was assigned to the part. The material properties used for the

finite element analysis of PLA are listed in Table 12. A temperature of 25°C was used as environmental temperature. A convective heat transfer coefficient of 100 $W \cdot m^{-2} \cdot K^{-1}$ was assumed for this study.

A transient thermal analysis was carried out with a timestep of 1 second. Using a small timestep would give a better resolution of temperature, capturing the peak temperatures better. However, the time required to complete the finite element simulation, and the space required to store the output results increases with decreasing timestep. Increasing the timestep would improve the speed of the simulation but miss capturing the peak and valley temperatures. A timestep of 1 second was used as a compromise to get a good time-temperature resolution within a reasonable time period. A predefined temperature of 200°C was used for PLA and a predefined temperature of 210°C was used for ABS.

The AM modeler plugin was used to define the progressive element activation and cooling interactions. A G-code to event series converter was written in Rust programming language. The event series file generated was used as an input to the AM modeler plugin. An analysis job was set up with 6 processors enabled.

Two elements, one deposited at the beginning of the simulation and another mid-way of the simulation were chosen to compare the results from the FEA model to the results from the discrete event simulation model.

4.4 Results and discussion

Figure 32 shows the nodal temperature distribution in the part at 766 seconds from the beginning of the print for the finite element simulation. The finite element simulation ran until 778 seconds from the beginning of the print. The elements that are deposited later are hotter compared to the elements that were deposited earlier.

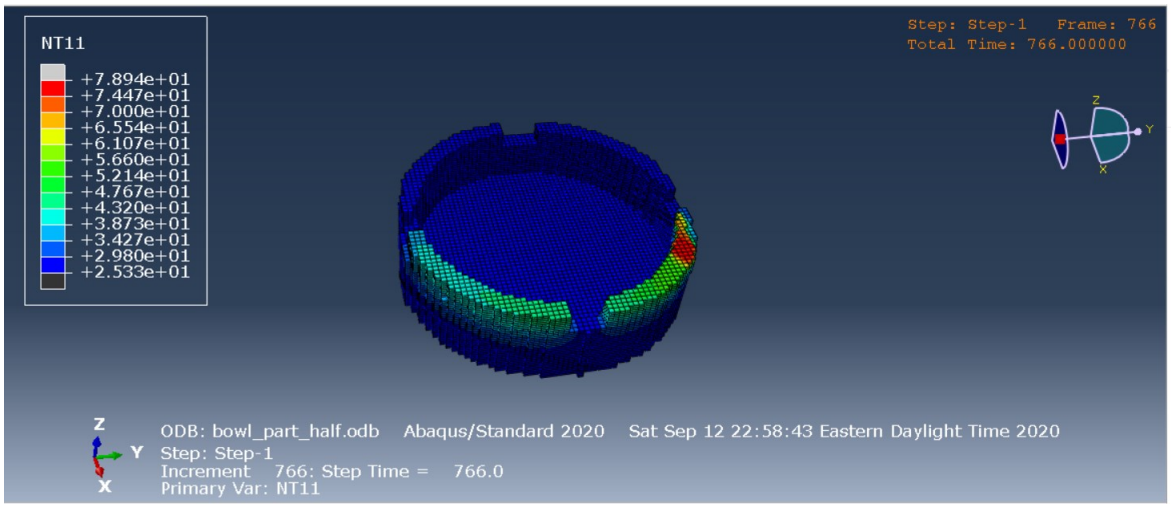

Figure 32: Temperature distribution in the model from FEA results.

Figure 33 shows the temperature versus time history of the 3D printed part at two different locations for the PLA material. The thermal history obtained from the DES model closely matches that obtained from the FEA model. The DES model has a better resolution as it shows results from every 0.01 second. Hence it can record the sharp peaks that arise when a new element is deposited next to another element.

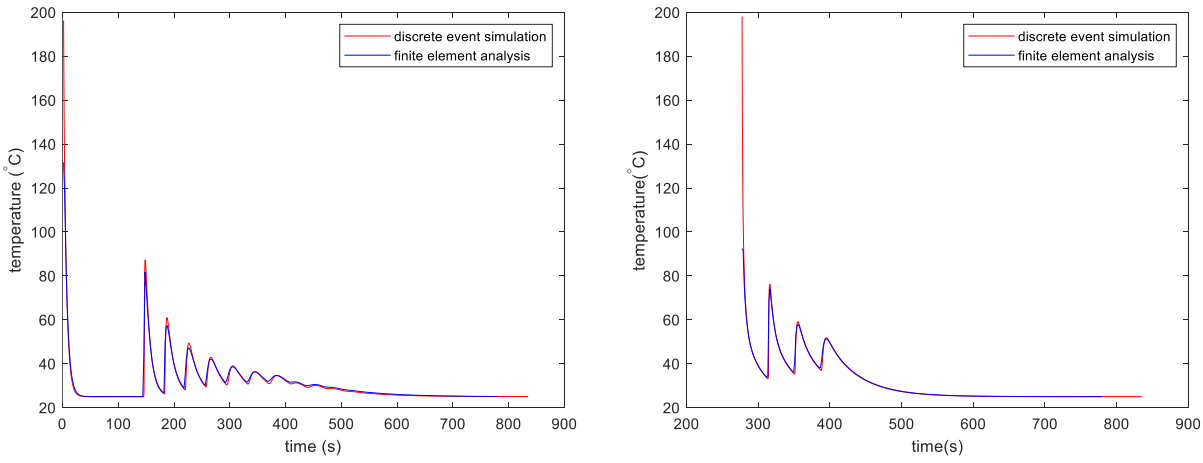

a) thermal history of 34th deposited element with centroid at (x = 26.0, y = 3.4, z = 0.2) mm.

b) thermal history of 12473th deposited element with centroid at (x = 31.6, y = 28.2, z = 1.8) mm.

Figure 33: Comparison of time temperature history calculated using discrete element simulation and FEM for PLA.

Figure 34 shows the temperature vs time history of the 3D printed part at two different locations for the ABS material. The thermal history obtained from the DES model closely matches the thermal history obtained from the FEA model.

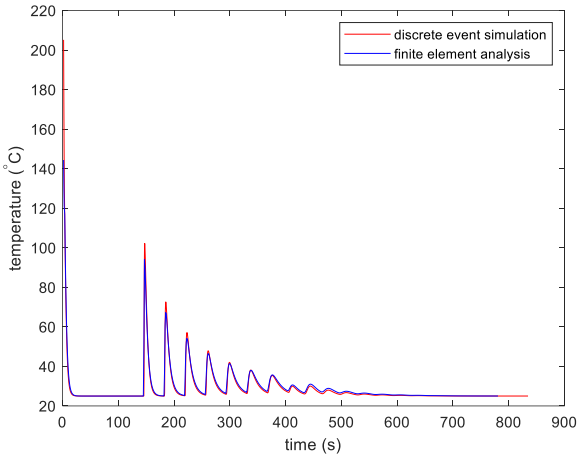

a) thermal history of 34th deposited element with centroid at (x = 26.0, y = 3.4, z = 0.2) mm.

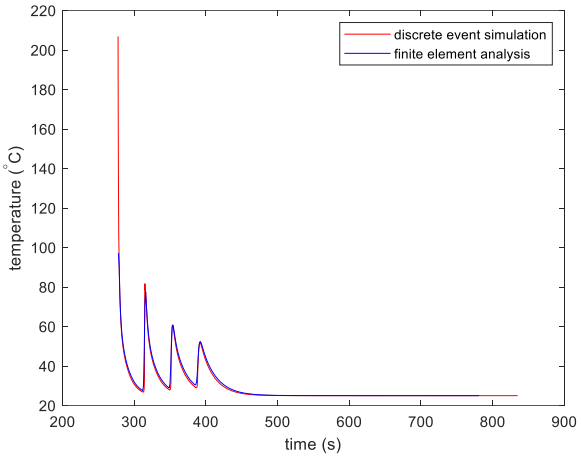

b) thermal history of 12473th deposited element with centroid at (x = 31.6, y = 28.2, z = 1.8) mm.

Figure 34: Comparison of time temperature history calculated using discrete element simulation and FEM for ABS .

For both PLA and ABS, the time-temperature history starts recording after the first timestep, which is 1s for the Abaqus FEA model and 0.01 second for the DES model. As a result, the initial temperature shown in the graphs is lower than the initial temperature of 200°C for PLA and 210°C for ABS. Figure 35 shows the effect of decreasing timestep on the results of the DES model. Figure 35a shows the thermal history of the 34th deposited element for the 3D printed part with ABS material. Four different timesteps of 0.01 seconds, 0.005 seconds, 0.0025 seconds, and 0.00125 seconds are shown. However, the thermal histories obtained by using the four timesteps are too close to see any difference in the line plots. The first reheating peak is marked with a red ellipse. The marked area is zoomed in and shown in Figure 35b to view the difference in results for models using the different timesteps. The peak values seem to be converging with smaller timestep. With each halving of the timestep, the difference in peak temperature becomes smaller. However, the difference between the peaks for models using 0.00125-

seconds timestep and 0.01-seconds timestep is about 0.3°C, which is very small compared to the temperature of the elements in the model.

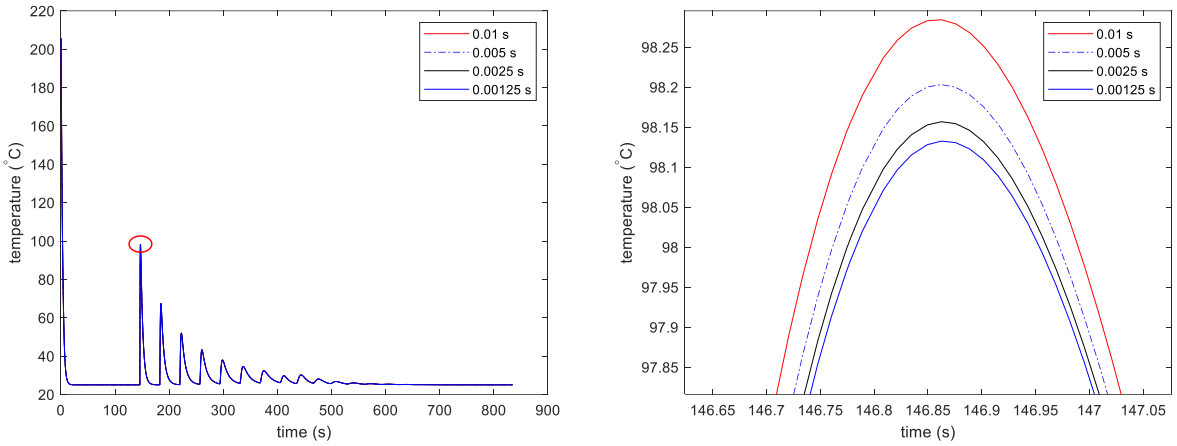

a) thermal history of 34th deposited element with centroid at (x = 26.0, y = 3.4, z = 0.2) mm.

b) thermal history of 34th deposited element zoomed in at the first reheating peak.

Figure 35: Effect of decreasing timestep on the DES model results for ABS.

Figure 36 shows the effect of making the 34th deposited element inactive when it is 10, 15, 20, 25, and 30 layers away from the most currently deposited layer. Figure 36 also shows the thermal history of the 34th deposited element when it is active throughout the analysis. The reheating peaks are about 4°C high after 10 layers of deposition. If the element is made inactive after 10 layers of deposition, the reheating peaks that are lower than 4°C will not be recorded by the model. Similarly, the reheating peaks after 15, 20, 25, and 30 layers of deposition are 0.6°C, 0.3°C, 0.08°C, and 0.01°C high. The choice for distance to the currently deposited layer should be based on the accuracy desired for the model. Bonding between thermoplastic beads only happens at a temperature higher than the glass transition temperature [68, 86]. Thermal models used to predict such bonding can use a 10-layer distance or lower for inactive elements. Young's modulus for thermoplastic materials increases rapidly at glass transition temperature with decreasing temperature. Models predicting residual stress are more sensitive to temperature changes at a lower temperature as Young's modulus for materials increases with decreasing temperature [157].

For such models that predict residual stresses, inactive elements that are 20 layers away might be necessary.

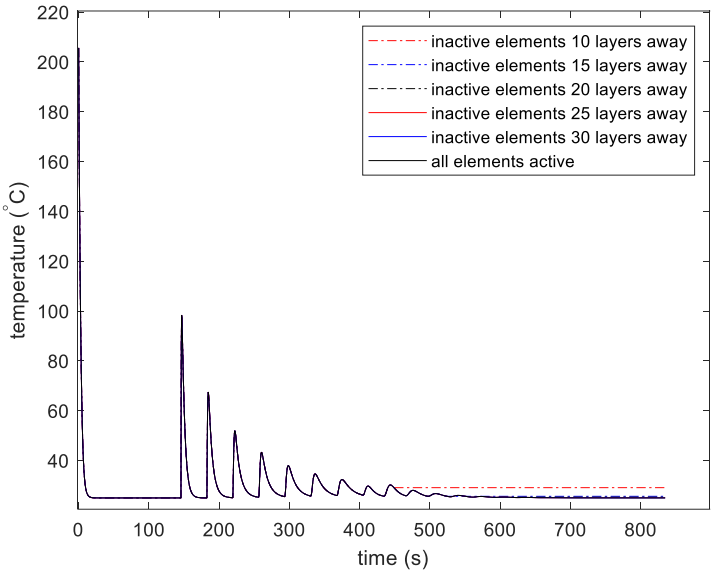

Figure 36: Effect of the distance of inactive element from most recently deposited layer.

The FEA modeling-based simulation for PLA material was completed in 1 hour 36 minutes (5766 seconds) with 6 cores. The simulation using the DES model was completed in 11.3 seconds with 6 cores. A speedup of 510 times was obtained using discrete event simulation in this case.

The FEA modeling-based simulation for ABS material was completed in 1 hour 30 minutes (5420 seconds) with 6 cores. The simulation using the DES model was completed in 11.1 seconds with 6 cores. A speedup of 488 times was obtained using discrete event simulation in this case.

Figure 37 shows the speedups in the DES model by using a higher number of cores. The core of the algorithm used for calculating the temperatures is highly parallel. The temperature of an element is dependent only on its own properties and the properties of its immediate neighbors. The simulation can be sped up by using a higher number of CPU cores.

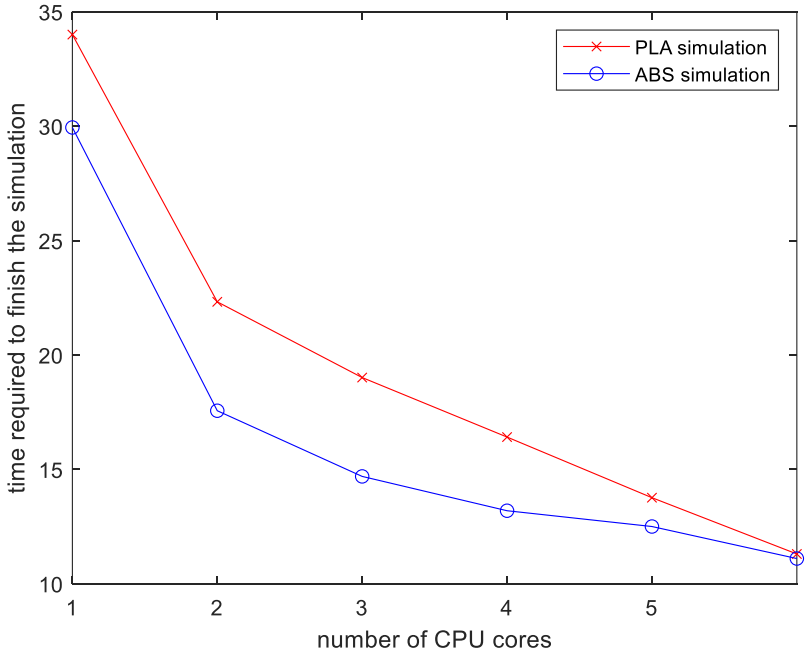

Figure 37: Time to finish the simulation vs the number of CPU cores used.

The experimental observations from different research works show certain features in the thermal history that could also be found in the thermal history presented by this model. It has been observed in various research works that the temperature of the deposited bead decreases rapidly after deposition [68, 86]. The rapid cooldown of the deposited element is attributable to the loss of heat to the neighboring bead via conduction and to the environment via convection. The heat loss is characterized by an exponentially decreasing temperature with time. The time-temperature history predicted by the model shows similar temperature loss in deposited elements. Another characteristic of the time-temperature history of the deposited beads in 3D printing is the rapid reheating by conduction of heat from the beads deposited above it [146, 158-160]. The reheating of the elements is even more rapid than the cooling down of the element with an almost instantaneous rise to the peak. The model presented in this manuscript shows similar reheating of deposited elements due to freshly deposited beads above it. A common observation in 3D printed model is the exponential decrease in reheating

peaks with an increase in the distance to the newest layer deposited [86, 148, 159]. The model presented here shows a similar decrease in the reheating peaks, with depositions in layers 20 depositions away having minimal effect on the thermal history of the 3D printed part.

The DES model has a better resolution as it stores results from every 0.01 second. Hence it can record the sharp peaks that arise when a new element is deposited next to another element. The difference in peaks between the FEA model and the DES model is higher for the PLA part than that for the ABS part. PLA exhibits much sharper changes in specific heat capacity compared to ABS and the FEA model with higher timestep can only capture the changes at a coarser resolution.

The speedups result mainly because of two reasons. Firstly, the discrete element model only considers immediate neighbors for heat transfer for a small timestep since it uses an explicit scheme for solving the heat transfer problem. As a result, solving a large system of linear equations is avoided. There is a huge difference in solution times is that the model used in the study uses explicit solution scheme to generate the thermal history and Abaqus standard uses an implicit solution scheme. Since only information about immediate neighbors is used for each element in a given timestep, each element can be updated individually independent of other elements that are not its immediate neighbors. As a result of this locality, parallel threads running on different cores can be used to update the temperature of each element for a given timestep. Secondly, the model considers the elements in far-away layers (at least 20 layers away from the layer being currently deposited for this study) to be inactive and does not update the temperature of such elements. Consequently, the number of elements that need to be updated at each timestep is limited. As a result, the model can simulate the thermal history of 3D printed material in linear time, i.e., increasing the model size increases the simulation time proportionally. In contrast, in the conventional finite element models, increasing the size of the model

increases the simulation time non-linearly, making the thermal simulation of 3D printed large parts prohibitively long.

The numerical model presented is significantly faster than the equivalent finite element model. The model would allow designers to quickly compare the effects of different printing parameters on the thermal history of 3D printed part and allow to select the most suitable printing parameters for a given part.

The DES model implemented currently works with hexahedral elements only. Figure 38 a) shows the toolpath for manufacturing a hollow box. The hollow box has its sides aligned with the principal axes. The mesh shown in Figure 38 b) is generated by dividing the volume into small cells (elements) and activating the cells as the toolpath passes through the cells. The mesh generated using such a technique generates a good representation of the surface 3D printed geometry that has flat surfaces and aligned along the principal axes. However, for geometries with curved surfaces or flat surfaces that do not align with principal axes, this method of mesh generation produces a mesh that deviates from the actual geometry of the 3D-printed part. As a consequence of such a method of mesh generation, a smooth curved surface geometry is represented as a collection of blocks. A flat surface that is not aligned with the principal axes also produces blocks that deviate from the original geometry of the 3D-printed part.

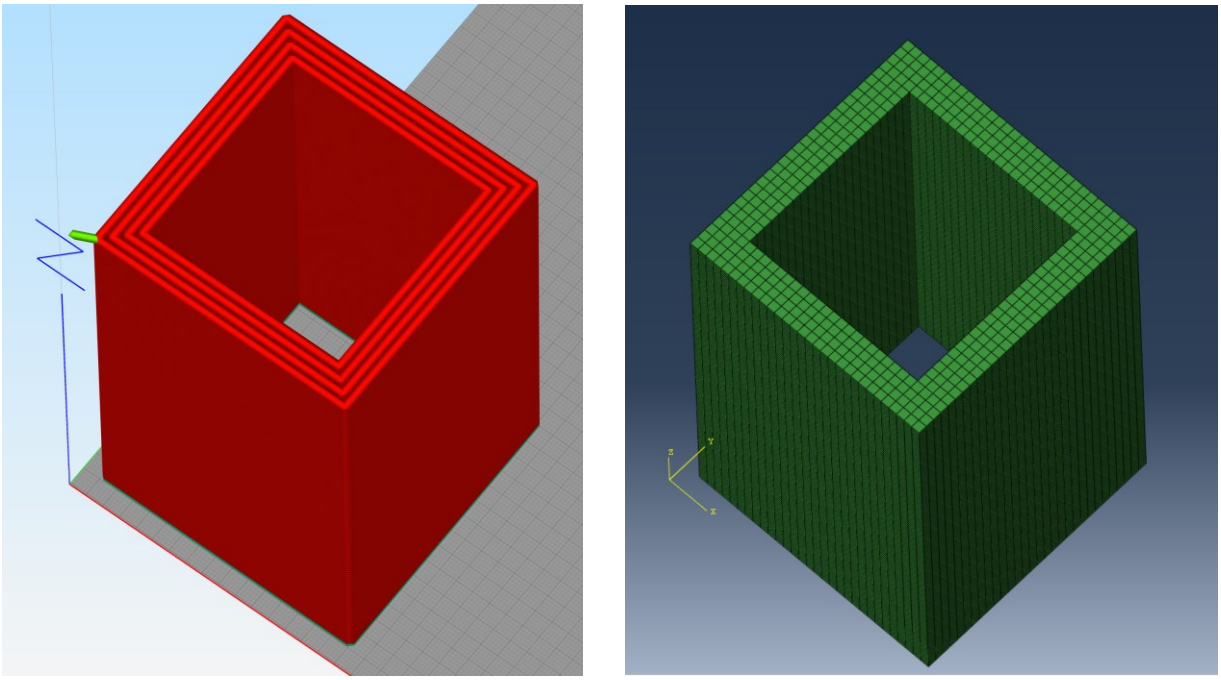

a) Toolpath for a hollow box. b) Mesh generated for hollow box toolpath.

Figure 38: Printing toolpath and mesh generated for geometries with flat surface aligning with principal planes.

Figure 39 a) and Figure 39 c) show the toolpath for a hollow cylinder and a hollow tapered geometry respectively. Figure 39 b) and Figure 39 d) show the mesh generated for the hollow cylinder and the hollow taped geometry part. The meshes have stepping effects with jagged edges instead of smooth surfaces. The surface area of the mesh is higher than the actual surface area of the part. As a result, the model overestimates heat losses through the surface via convection. The volume, however, remains comparable to the original geometry.

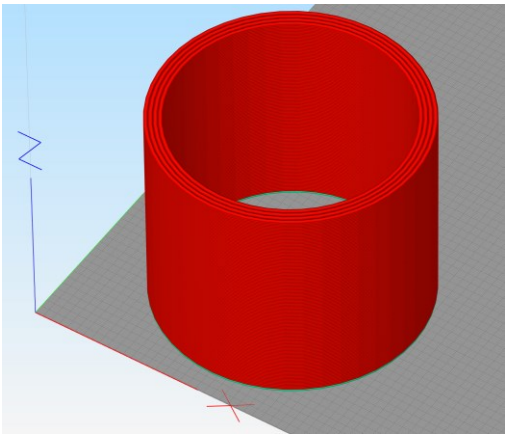

a) Toolpath for hollow cylinder.

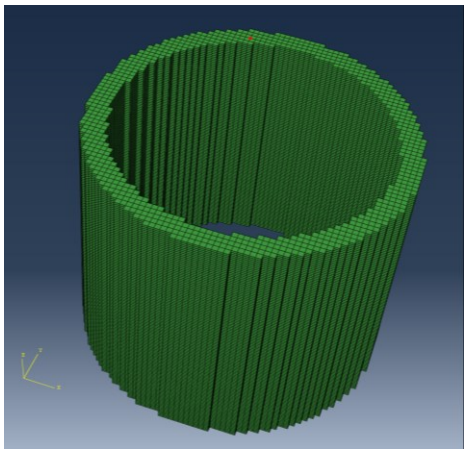

b) Mesh generated for hollow cylinder toolpath.

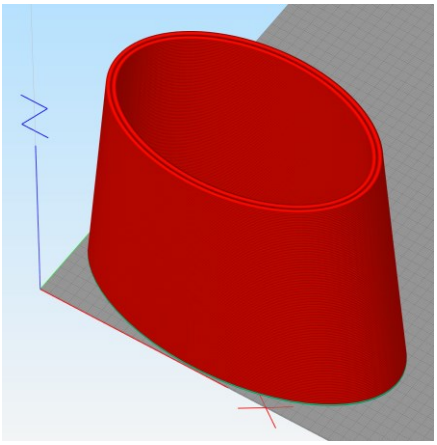

c) Toolpath for hollow tapered geometry.

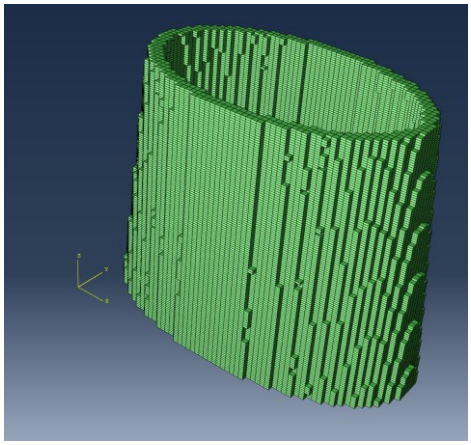

d) Mesh generated for hollow tapered geometry toolpath.

Figure 39: Printing toolpath and mesh generated for geometries with curved surfaces.

Future work should explore the possibility of a better mesh generation method. The possibility of using distorted hexahedral elements could be explored. Another promising venue that could be explored is the incorporation of tetrahedral elements into the model and generation of combined tetrahedral and hexahedral elements to represent the mesh.

4.5 Conclusions

The following conclusions were drawn from the research work presented:

1) A fast and accurate numerical model can be formulated based on heat exchange between deposited elements to generate the thermal history of polymer extrusion-based 3D printed parts. The formulated DES numerical model was shown to be fast and accurate for thermal simulation of extrusion-based additive manufacturing.

2) Orthotropy in 3D printed parts can be accounted for in the simplified numerical model by using the information on the orientation of deposited beads from the G-code. The effect of orthotropic conductivity in the 3D printed PLA part was simulated using the DES model. The DES model was able to account for the orthotropic conductivity of the 3D printed PLA part used for the study.

3) The temperature-dependent material response can be captured in the DES model simulation of the thermal behavior of 3D printed polymers. Temperature-dependent specific heat capacity was used for PLA and ABS. Temperature-dependent conductivities were used for ABS. The DES model can incorporate the effects of temperature-dependent material properties of the 3D printing polymers.

4) The DES model has accuracy comparable to the accuracy offered by finite element models. The results from the DES model were found to be comparable with the results from the FEA model.

CHAPTER 5
COUPLED THERMO-MECHANICAL NUMERICAL MODEL TO PREVENT LAYER COLLAPSE IN LARGE-SCALE ADDITIVE MANUFACTURING OF BIO-BASED THERMOPLASTIC COMPOSITE

5.1 Chapter Abstract

A challenge in large-scale thermoplastic polymer extrusion-based additive manufacturing of renewable bio-based wood-flour/PLA thermoplastic composite is to determine a combination of extrusion rate and extrusion temperature such that the deposited material is hot enough to ensure bonding but cold enough to avoid collapse under self-weight. Currently, such a combination is determined via a trial-and-error approach. This research work determines a suitable combination for a given deposition toolpath by using numerical simulations. The presented simplified low-fidelity method aids manufacturing by quickly determining if a part will collapse under its self-weight during manufacturing based on the maximum viscous strains calculated by a sequentially coupled thermo-mechanical numerical model. It was found that layers farther from the bed cool slower and consequently have greater viscous strains. The presented model can quickly check if a combination of temperature and extrusion rate causes layer collapse due to self-weight and hence be used to identify suitable processing parameters.

5.2 Introduction

Large-scale extrusion-based additive manufacturing has become increasingly widespread in research and development and is headed towards industrial use. The size of the parts that can be manufactured using large-scale 3D equipment has increased consistently over the years. BAAM (Big area additive manufacturing), one of the first large-scale 3D printers, was completed in January 2015. BAAM increased the size of parts by over 10 times, increased manufacturing speed by over 1000 times, and reduced the cost by over 100 times compared to the next largest 3D printer available at the time [161]. Polymer extrusion-based large-scale additive manufacturing process has since been used in a variety of applications including tooling for automotive [162], automotive body [163], boat hull molds [164], precast concrete formwork [165, 166], and rotor blade trim tools.

While scaling up enables extrusion-based additive manufacturing to produce larger parts at faster speed and reduced costs, scaling up also introduces a new set of challenges to extrusion-based additive manufacturing. The challenges include the design of large stiff frames, controlling the temperature of the surrounding environment, maintaining effective melting of the printing material for extrusion, supplying mass of material for print [34]. Roschili et al. discussed the design problems encountered in large-scale additive manufacturing including challenges during the preparation of a print, bead width constraints, layer time limitations, and the challenge of maximizing throughput.

One of the major challenges in large-scale additive manufacturing is the selection of a suitable layer time. Roschli et al. discussed the concepts of minimum layer time and maximum layer time in polymer extrusion-based large-scale additive manufacturing. If a layer does not cool down sufficiently, it does not become rigid enough to support another layer above it. The layer time required for the layer to cool down enough to be able to support the layer above it is called minimum layer time. If the layer is cooled down too much, the bonding with the layer above it is hindered and the layer does not adhere properly.

The layer time for which the bonding between the layers remains at acceptable levels is called maximum layer time. A suitable layer time is bounded by the minimum layer time and the maximum layer time .

With the increase in the use of polymer extrusion-based additive manufacturing, concerns about environmental issues regarding the disposal of massive waste and possible toxic byproducts have been raised [167, 168]. Several renewable bio-based thermoplastic composites have been developed to reduce the consumption of petrochemical-based polymers and reduce waste [169, 170]. PLA (polylactic acid) thermoplastic composites are the most commonly used bio-based thermoplastic composites used in additive manufacturing [38, 42, 49, 165, 171, 172]. PLA is a semi-crystalline thermoplastic polymer and its degree of crystallization depends on the cooling rate during its processing as well as the reinforcement in its composites [173]. In large-scale additive manufacturing, the cooling rate is slower compared to small-scale additive manufacturing [34, 174-176] due to the comparatively smaller surface area to volume ratio. As a result of the slower cooling, PLA composites crystallize significantly more in large-scale 3D printing and the mechanical behavior of the polymer composites depends on the thermal history during manufacturing [177].

The concept of layer time is based on the change in mechanical properties of polymers with temperature. The mechanical properties of the polymers used in extrusion-based additive manufacturing change with temperature. The polymers undergo several transitions when cooled down from high extrusion temperatures to low room temperatures [178, 179]. Two notable transitions that affect the 3D printing process are melting and glass transition. The polymers used in polymer-based additive manufacturing are broadly divided into two categories, namely, semi-crystalline and amorphous polymers [39, 46, 180, 181] . Glass transition is marked by a sharp change in stiffness of the polymer for both semi-crystalline and amorphous polymers. Melting transition is prominent in semi-crystalline polymers where the crystalline region in the polymer melts and the polymer becomes starts flowing.

Since there are no crystalline regions in amorphous polymers, melting transition is not observed in amorphous polymers. Amorphous polymers are more amenable to additive manufacturing since the amorphous polymers do not undergo significant dimensional contraction associated with polymer crystallization as in semi-crystalline polymers [182]. Rather a steady decrease in storage modulus and viscosity is noted with increasing temperature. When the molten polymer is deposited during the additive manufacturing process, it cools down and becomes rigid with decreasing temperature. Duty et al [183] identified the four stages that a polymer undergoes during the cooldown after extrusion during additive manufacturing, namely, viscous liquid, viscoelastic liquid, viscoelastic solid, and elastic solid.

i. Viscous Liquid: At near extrusion temperature, the fluid-like nature of the polymer is dominant and is characterized by high values for tan δ, which is the ratio of loss modulus to storage modulus during DMA. For the viscous liquid behavior, strain can be calculated using Equation 5.1.

$$\varepsilon = \int \dot{\varepsilon}\, dt = \int \frac{\sigma}{\eta_0} dt \tag{5.1}$$

where,

ε = strain

$\dot{\varepsilon}$ = strain rate

σ = applied stress

η_0 = the viscosity of the material

ii. Viscoelastic Liquid: As the polymer cools down, the elastic nature of the polymer becomes significant and is categorized as a viscoelastic liquid. Maxwell model can be used to calculate the strain in the material using Equation 5.2.

$$\varepsilon = \int \dot{\varepsilon}\, dt + \frac{\sigma}{G_0'} = \int \frac{\sigma}{\eta} dt + \frac{\sigma}{G_0'} \tag{5.2}$$

where,

G_0' = shear modulus at a low shear rate

iii. Viscoelastic solid: As the polymer cools down even further, the elastic behavior of the polymer is more prominent than the viscous behavior. Kelvin-Voigt model can be used to model this behavior using Equation 5.3.

$$\varepsilon = \frac{\sigma}{G_0'}\left(1 + \frac{1}{\tau}\int e^{-\frac{t}{\tau}} dt\right) \tag{5.3}$$

where,

τ = characteristic processing time, G_0'/η_0

iv. Elastic Solid: When the polymer cools down below its glass transition temperature, the viscous behavior is insignificant for short-term strain and elastic behavior dominates the overall short-term deformation of the polymer. The strain can be written as Equation 5.4.

$$\varepsilon = \frac{\sigma}{G_0'} \tag{5.4}$$

Duty et al. chose a value of tan δ greater than 10 to mark the viscous liquid behavior region, between 1 and 10 for the viscoelastic liquid region, between 0.1 and 1 for the viscoelastic solid behavior region, and less than 0.1 for the solid behavior region for 3D printing polymers.

Different methods have been used to monitor the time-temperature data of the polymers and the effects of corresponding changes in mechanical properties during the additive manufacturing process. Yin et al. inserted thermocouples into 3D printing specimens to measure temperature at the interface between layers to predict interlayer diffusion in the specimens. Borish et al. used thermal imaging to monitor the single-layer time alteration in large-scale additive manufacturing. Fathizadan et al. used a set of thermal images to generate temperature data on the surface and used a control model to predict the best time for printing the next layers. Wang et al. used temperature data from thermal images to enable real-time control of large-scale 3D printing.

Numerical models have also been used to determine the temperature changes of the additively manufactured parts during the printing process. The thermal models solve the heat equation, as shown in equation 4.1, in combination with the changing geometry of the part during printing to generate the thermal history of the additively manufactured part.

The temperature-time history can be used in conjunction with the temperature-dependent material properties can be used to determine the viscoelastic deformation during the thermoplastic polymer extrusion-based additive manufacturing process. Sun et. al. described a mathematical model and used the model to numerically calculate the temperature of 3D printed parts and to model bond forming between ABS (acrylonitrile butadiene styrene) filaments. Wang et. al. used a simplified mathematical model to calculate the temperature and the resulting warp deformation in 3D printed ABS parts. Zhang et. al. used an adaptable, boundary adjusting finite difference method to numerically generate the thermal history of a 3D printed PLA (polylactic acid) part. Stockman et al. used the finite difference method to create a thermal model tailored for additive manufacturing. Ji and Zhou described the use of a finite element model with temperature-dependent material properties. The finite element method has been used recently to simulate the thermal history of polymer extrusion-based 3D printed materials.

Some of the models are layer-by-layer simulations that use simplified assumptions about the thermal behavior of materials [157, 184]. The more recent finite element modeling approach uses the concept of element activation, whereby an activation variable is multiplied with the constitutive equations to simulate material deposition. The activation variable can vary from zero to one depending on whether the region defined by finite element mesh is empty, partially filled, or completely filled with the deposited material at a given time [135, 154, 185]. Bhandari and Lopez-Anido presented a discrete-event simulation-based thermal model to predict the thermal history of a 3D printed part and compared it with the results from the finite element model. The discrete-event simulation results were found to be comparable in accuracy with the finite element model results. The discrete-event simulation was faster in generating the thermal history by two orders of magnitude compared to the finite element model.

A low-fidelity numerical model with fast solution times enables the generation of viscoelastic deformation of the extruded material layers due to the weight of the layers above it. A high deformation would cause the deposited layers to collapse under self-weight. Based on the viscoelastic deformation calculated by the numerical model, it can be determined whether the layer time for a particular set of printing parameters and toolpath is shorter than the minimum layer time. The objectives of this research work are to:

1. Prevent the collapse of an extruded layer of bio-based PLA/wood composite material in the extrusion-based large-scale additive manufacturing process by identifying a suitable combination of an extrusion temperature and a deposition rate (layer time).
2. Check for excessive viscous deformations in the layer to determine if collapse would occur using a discrete-event thermal model sequentially coupled with a finite element structural model.
3. Use the coupled thermo-mechanical model can be used to determine a suitable layer time (deposition rate) and extrusion temperature for a part with a given deposition toolpath.

5.3 Materials and Methods

5.3.1 Materials and Material property characterization

HiFill® PLA 1816 3DP from TECHMER PM was used as the feedstock material for additive manufacturing. The natural fiber-reinforced polylactic acid (PLA) thermoplastic composite is biobased and consists of 30% wood flour filler by weight.

The thermal and mechanical properties required as input by the numerical model were characterized experimentally. The specific heat capacity of the polymer composite was characterized using differential scanning calorimetry (DSC). The shear modulus and viscosity of the material were characterized using dynamic mechanical analysis (DMA) in shear mode using a parallel plate rheometer. The thermal conductivity of the material was characterized using a heat flow meter (HFM).

5.3.1.1 Differential scanning calorimetry

DSC was used to determine the specific heat capacity of the material at different temperatures. DSC was carried out using a TA Q2000 calorimeter. Approximately 5 mg samples were prepared from the feedstock material. A cooling cycle followed by a cooling cycle from 220°C to 25°C was carried out at a rate of 5°C/min. Three replicated were tested. The specific heat capacities obtained from the heating cycle were used. Hence, the crystallinity of the material resulting due to the 3D printing thermal history is included by the model.

5.3.1.2 Dynamic mechanical analysis

DMA was carried out to determine the storage modulus and viscosity of the PLA/wood thermoplastic composite at different temperatures. DMA of the feedstock material was performed using a Discovery HR 30 from TA instruments. A 25 mm diameter parallel plate set was used. A specimen of 25 mm diameter and 1 mm thickness was prepared. placed in between the parallel plates. The specimen was

heated from 75°C to 220°C and at a rate of 5°C/min with cyclical strain rates of 10Hz, 1.0 Hz, and 0.1 Hz were applied to the material.

5.3.1.3 Thermal conductivity measurement

A NETZCH 446 Lambda Series heat flow meter was used to measure the thermal conductivity of the PLA/wood thermoplastic composite. Three specimens with approximately 150 mm x 150 mm width and 16.0 mm height were tested. ASTM C518 test standard was followed for the measurement of thermal conductivity. Thermal conductivity was measured at seven different temperatures, 25°C, 35°C, 45°C, 55°C, 65°C, 75°C, and 85°C, and an average was taken as input for the numerical model. The top plate was maintained at a temperature 5°C higher than the mean temperature and the bottom plate was maintained at a temperature 5°C lower than the mean temperature.

5.3.2 Discrete event simulation (DES) model

DES model was used to generate thermal history and the layer deformation in the z-direction due to viscoelastic deformation of the 3D printed material based on the toolpath and the print parameters. DES model was previously used to generate thermal history for desktop scale 3D printed parts and compared with finite element model results .

The DES model is based on solving finite difference equations for the heat equation mentioned in Equation 1 using a forward Euler method. The model discretizes the 3D printed part into hexahedral (brick) elements and simulates the deposition of material as discrete events that activate the elements. The model updates the temperature of the activated element by accounting for heat exchange between adjacent material and the environment in small time increments.

The DES thermal model presented in Chapter 4 is extended to account for the heat losses due to thermal radition using equation 5.5.

$$dQ_r = \sigma \,.\, \varepsilon \,.\, (T^4 - {T_{env}}^4) \,.\, A.\, dt \qquad (5.5)$$

where,

dQ_r	=	heat loss to environment via radiation
σ	=	Setfan Boltzmann constant ($5.670374 \times 10^{-8}\ \mathrm{W \cdot m^{-2} \cdot K^{-4}}$)
ε	=	emissivity of the material
A	=	area of the surface radiating surface
T	=	absolute temperature at the centroid of element
T_{env}	=	absolute temperature of the environemnt
dt	=	time increment

This research work extends the DES thermal model to evaluate the local viscoelastic deformation in each layer due to the self-weight and the weight of layers above it. Figure 40 shows the flowchart of the DES model with local viscoelastic strain calculation. The rectangle with the green outline in the flowchart shows the process of calculating the viscous strains in each of the elements.

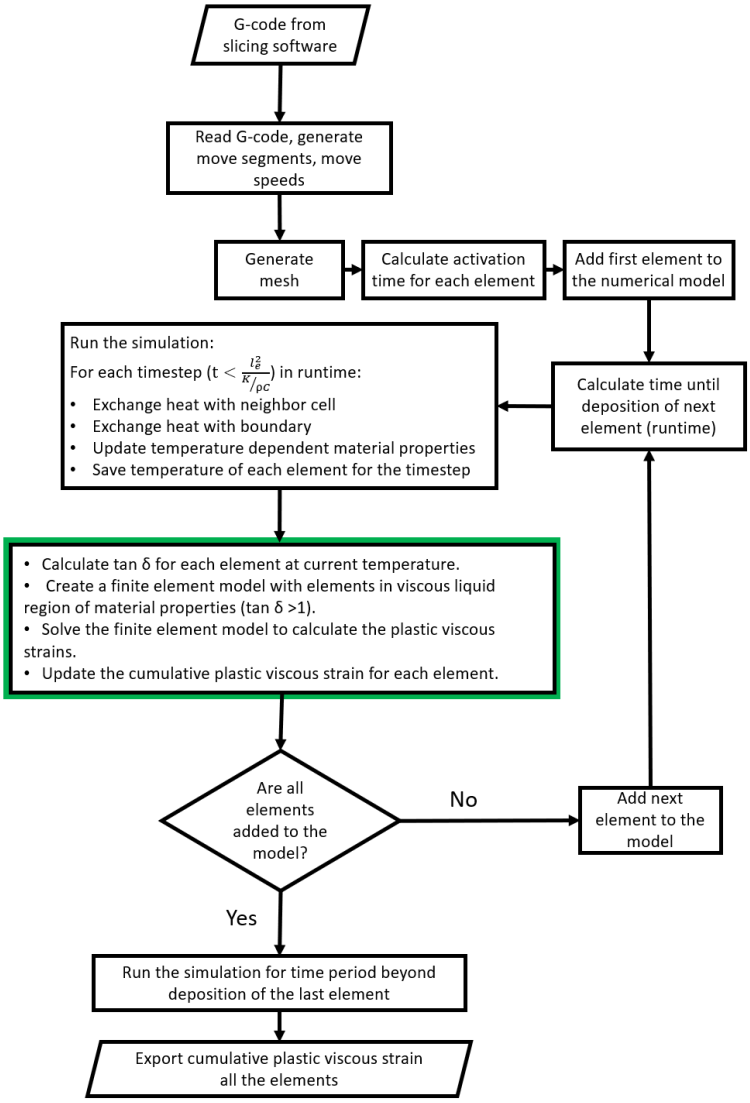

Figure 40: Flowchart of DES model with elemental viscous strain calculation.

The temperature of each element is calculated at every time step. Based on the temperature, tan δ is calculated for the element. Shear modulus, viscosity, and conductivity at the temperature are interpolated from the experimental values.

A finite element mechanical model is used to determine the viscous strains in the elements. 8-noded hexahedral (brick elements) were used. The finite element model was implemented in the Rust

programming language. An isotropic material model with temperature-dependent Young's modulus and viscosity. A Poisson's ratio of 0.33 [186, 187] was used for the model. Only self-weight loads were considered in this analysis. The bottom nodes, that contact the bed, were assigned fixed boundary conditions. Since the viscoelastic liquid region of the material behavior affects the stability of the layer, the element was considered active if the tan δ was greater than 1. Once tan δ dropped below 1, the element was considered inactive, and all the nodes associated with the element are assigned a fixed boundary condition. On reheating, if the temperature increases so that tan δ increases above a value of 1, the element is considered active again, and the boundary conditions to the node are removed. Such activating and deactivating of the elements limits the degrees of freedom in the finite element model and allows the simulation to complete in a reasonable amount of time.

The viscoelastic strain can be divided into two components, viscous strain that increases and accumulates over time, and elastic strain that does not accumulate over time. Since the elastic strain is dependent on the Youngs modulus, which is a function of temperature that is changing with time, elastic strain changes with time. However, the elastic strain does not accumulate over time with each time step. The total strain is the sum of the viscous strain and the elastic strain as expressed in equation 5.6.

$$\varepsilon = \varepsilon_e + \varepsilon_v \tag{5.6}$$

where,

ε_e = elastic strain

ε_p = viscous strain

An 8-noded hexahedral element has a shape function of the form shown in Equation 5.7 and Equation 5.8.

$$N1 = \frac{(1-\xi)(1-\eta)(1-\zeta)}{8}$$

$$N2 = \frac{(1-\xi)(1-\eta)(1-\zeta)}{8}$$

$$N3 = \frac{(1-\xi)(1-\eta)(1-\zeta)}{8}$$

$$N4 = \frac{(1-\xi)(1-\eta)(1-\zeta)}{8}$$

$$N5 = \frac{(1-\xi)(1-\eta)(1-\zeta)}{8} \quad (5.7)$$

$$N6 = \frac{(1-\xi)(1-\eta)(1-\zeta)}{8}$$

$$N7 = \frac{(1-\xi)(1-\eta)(1-\zeta)}{8}$$

$$N8 = \frac{(1-\xi)(1-\eta)(1-\zeta)}{8}$$

$$\{N\}_{1x8} = \{N1, N2, N3, N4, N5, N6, N7, N8\} \quad (5.8)$$

where,

ξ, η, ζ = length along the local coordinates

N1,N2,N3,N4, N5,N6,N7,N8 = Shape functions

$\{N\}_{1x8}$ = shape functions vector

The derivatives of shape functions are calculated as shown in eq (5.9).

$$[dN]_{3x8} = \begin{bmatrix} \frac{\partial N}{\partial \xi} \\ \frac{\partial N}{\partial \eta} \\ \frac{\partial N}{\partial \zeta} \end{bmatrix} \quad (5.9)$$

where,

$[dN]_{3x8}$ = derivative of shape function

Material coordinates derivative is calculated in two steps as shown in equations 5.10-5.11.

$$[J]_{3x3} = [dN]_{3x8}[n]_{8x3} \tag{5.10}$$

$$[dM]_{3x8} = [J]^{-1}{}_{3x3}[dN]_{3x8} \tag{5.11}$$

where,

$[n]_{8x3}$ = coordinates of the nodes of the element

$[J]_{3x3}$ = Jacobian matrix

$[dM]_{3x8}$ = material coordinates derivative

The displacement to strain matrix, $[B]_{6x24}$, for the element is calculated as shown in equation 5.12.

$$[B]_{6x24} = \begin{bmatrix} dM(1,1) & 0 & 0 & dM(1,2) & 0 & 0 & \dots & dM(1,8) & 0 & 0 \\ 0 & dM(2,1) & 0 & 0 & dM(2,2) & 0 & \dots & 0 & dM(2,8) & 0 \\ 0 & 0 & dM(3,1) & 0 & 0 & dM(3,2) & \dots & 0 & 0 & dM(3,8) \\ dM(2,1) & dM(1,1) & 0 & dM(2,2) & dM(1,2) & 0 & \dots & dM(2,8) & dM(1,8) & 0 \\ 0 & dM(3,1) & dM(2,1) & 0 & dM(3,2) & dM(2,2) & \dots & 0 & dM(3,8) & dM(2,8) \\ dM(3,1) & 0 & dM(1,1) & dM(3,2) & 0 & dM(1,2) & \dots & dM(3,8) & 0 & dM(1,8) \end{bmatrix} \tag{5.12}$$

The local stiffness matrix, $[K_{loc}]_{24x24}$, for the 8-noded hexahedral element is calculated by using eight-point Gauss integration, as shown in equation 5.13.

$$[K_{loc}]_{24x24} = \sum_{i=1}^{8} [B]_i^T [C][B]_i \, |[J]_i| \tag{5.13}$$

where,

$[B]_i^T$ = displacement to strain matrix at ith Gauss integration point

$|[J]_i|$ = determinant of the Jacobian at ith Gauss integration point

$[C]$ = material stiffness matrix

The material stiffness matrix, [C], is shown in equation 5.14.

$$[C] = \frac{E}{(1-2\nu)(1+\nu)}\begin{bmatrix} 1-\nu & \nu & \nu & 0 & 0 & 0 \\ \nu & 1-\nu & \nu & 0 & 0 & 0 \\ \nu & \nu & 1-\nu & 0 & 0 & 0 \\ 0 & 0 & 0 & \frac{1-2\nu}{2} & 0 & 0 \\ 0 & 0 & 0 & 0 & \frac{1-2\nu}{2} & 0 \\ 0 & 0 & 0 & 0 & 0 & \frac{1-2\nu}{2} \end{bmatrix} \quad (5.14)$$

where,

E = Young's modulus

ν = Poisson's ratio

The global stiffness matrix is generated by assembling the local stiffness matrix of the elements that are active in the structural model, ie, elements with tan δ greater than 1.

Loads due to self-weight are distributed to element nodes using equation 5.15.

$$\{F_z\} = \sum_{i=1}^{8}[N]^T \rho g(z/h)\,|[J]_i|. \quad (5.15)$$

The nodal load vector for each element is added to a global load vector. Since only self-weight is being considered for the study, $\{F_x\} = \{F_y\} = 0$. The elastic deformations at the nodes of active elements are solved using equation 5.16.

$$\{u_{e\_bc}\} = [K_{g\_bc}]^{-1}\{F_{bc}\} \tag{5.16}$$

where,

$\{u_{el\_bc}\}$ = elastic deformation at free nodes.

$[K_g]$ = global stiffness matrix corresponding to free nodes.

$\{F_{bc}\}$ = loads at free nodes.

Equation (15) is solved using iterative conjugate-gradient method [188].

Elastic strain, $\{\varepsilon_e\}$, and elastic stress$\{\sigma_e\}$, are calculated using equation 5.17 and equation 5.18.

$$\{\varepsilon_e\} = \sum_{i=1}^{8}[B]_i^T\{u_e\} \tag{5.17}$$

$$\{\sigma_e\}, = \sum_{i=1}^{8}[C][B]_i^T\{u_e\} \tag{5.18}$$

where,

$\{u_e\}$ = elastic deformation at nodes of an element

The deviatoric stresses, $\{\sigma_{dev}\}$, are calculated using equation 5.19.

$$\{\sigma_{dev}\} = \{\sigma_e\} - \frac{1}{3}trace(\{\sigma_e\}) \tag{5.19}$$

where,

$trace(\{\sigma_e\})$ = $\sigma_e(1,1) + \sigma_e(2,2) + \sigma_e(3,3)$

Viscous strain rate, $\{\dot{\varepsilon_v}\}$, and viscous strain, $\{\varepsilon_v\}$, are calculated using equation 5.20 and equation 5.21.

$$\{\dot{\varepsilon_v}\} = \frac{\{\sigma_{dev}\}}{2\eta} \tag{5.20}$$

$$\{\varepsilon_v\}^{i+1} = \{\varepsilon_v\}^i + \{\dot{\varepsilon_v}\}\,\Delta t \tag{5.21}$$

where,

η	=	viscosity
Δt	=	time difference
$\{\varepsilon_v\}^{i+1}$	=	viscous strain at i+1 th time step
$\{\varepsilon_v\}^{i}$	=	viscous strain at ith step

The total load on an element increases as the number of layers above the element increases. The viscoelastic deformation increases with time and the layer deforms in the z-direction under its own weight and the weight of the layers above it. The layer also cools down in the meanwhile and increases in shear modulus and viscosity, thus reducing the rate of viscoelastic deformation in the z-direction. If the deformation in the z-direction is too high, the new layer to be deposited does not have a solid base layer upon which it can be laid. As a result, the layer collapses and print failure occurs. Duty et al. used a maximum limit of 10% strain in the layer to be used as a criterion for the collapse of the layer.

Convective heat transfer film coefficient is an important parameter that characterizes the heat loss per unit area at an interface with fluid due to convection. For large-scale extrusion-based 3D printing, convective heat losses occur at the interface on the boundary of the 3D printed part and the air surrounding it. For polymer extrusion-based processes, the convective heat losses control the cooling process [189] and heat losses due to radiation are negligible, especially at low extrusion temperatures used in this research work. Several empirical relations have been proposed to estimate a convective

heat transfer coefficient for isolated vertical and horizontal surfaces [190]. Research works have adapted these empirical relations to be used for additive manufacturing processes [175, 184]. A convective heat transfer of 12 $W/(m^2.K)$ was used as recommended by Breken et. al. [135, 191] based on experimental observations.

An emissivity value of 0.92 was based on experiments carried out by Morgan et al for 3D printed polymer composites [192].

The following sources of error have been identified in the model:

1. A viscoelastic behavior modeled using solid mechanics assumptions is used for the molten material. However, the molten material acts as a viscous liquid.
2. The material is assumed to have viscous deformation only at temperatures where tan δ is greater than 1.
3. Elastic deformations are calculated based on small deformation assumption. Large viscous strains are calculated based on the deviatoric stresses generated using linear elastic material behavior. Errors are introduced as the computational mesh remains unchanged after large deformations. However, the model is conservative in the sense that large strains result in the model predicting failure. Hence, the results when strains are excessively large are not used for the process design.
4. Shear locking due to the use of 8-noded linear hexahedral elements with full integration results in higher bending stiffness in the model.

These errors cause the model to have reduced accuracy. However, the low-fidelity model is less computationally intensive to solve. The model needs to be accurate enough to generate a pass/fail criteria regarding the collapse of the layer for a given set of printing parameters for the given geometry.

5.3.3 Application and Model validation

A 28” high 30” wide tapering section was analyzed using the model. Figure 41 shows the geometry of the 3D printed part for the study [193]. The part is one of the four segments of a culvert diffuser. The part is a thin-walled structure designed to improve the flow of water through culverts across the highways. An Ingersoll Masterprint large-scale additive manufacturing equipment was used to manufacture the part. A bead width of 12.7 mm and a layer height of 5.08 mm were chosen for this study. Three different layer times of 2 minutes 30 seconds, 3 minutes 10 seconds, and 4 minutes 45 seconds were used for the study. Two different extrusion temperatures of 200°C and 207°C were used for the experimental study. The part has a thickness of 25.4 mm and is 2 beads wide.

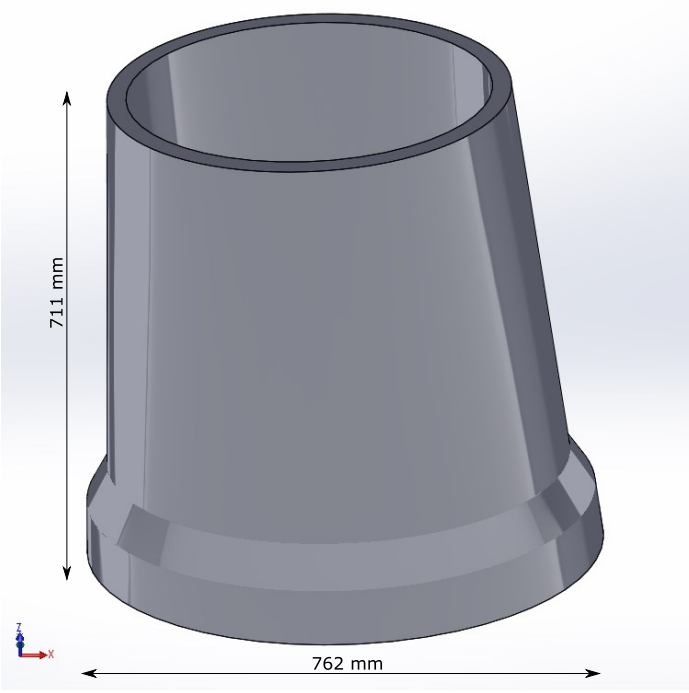

Figure 41: A segment of the 3D printed part used for this study.

Specific heat capacity, thermal conductivity, storage modulus, and viscosity were determined experimentally. Mesh size of 4.23 mm x 4.23 mm x 1.69 mm was chosen so that a single bead (12.7 mm width 5.07 mm height) into a 3 x 3 x 3 mesh. A mesh convergence study was carried out to verify mesh independence of the results. A single bead was divided into 1 x 1 x 1 (12.7 mm x 12.7 mm x 5.08 mm), 2 x 2 x 2 (6.35mm x 6.35 mm x 5.54 mm), and 3 x 3 x 3 meshes (4.23 mm x 4.23 mm x 1.69 mm). An extrusion rate of 27.22 kg/hr and extrusion temperature of 205 °C was chosen for the study. The maximum strain in the z-direction in the part was plotted as a function of number of elements in the model.

5.4 Results

5.4.1 Material Characterization tests

Figure 42 shows the specific heat capacity vs temperature for the PLA/wood material. The negative specific heat values are observed at about 100 °C due to the exothermic peak of the material due to cold crystallization. The specific heat capacity peaks at the melting region of the material which is at around 150 °C. The dual exothermic peaks indicate the melt recrystallization during the processing of the material .

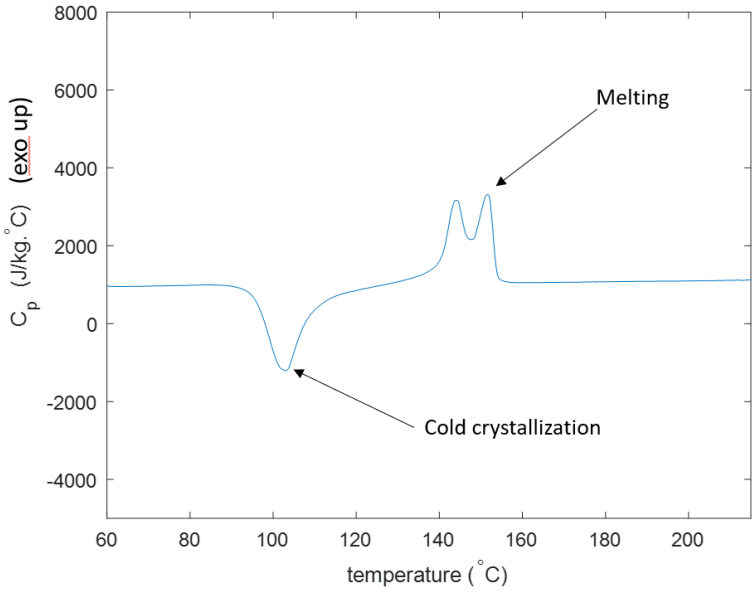

Figure 42: Specific heat capacity vs temperature for PLA/wood material.

The conductivity of the 3D printed PLA/wood material was found to be 0.205 $\mathrm{W}/(\mathrm{m}.\mathrm{K})$ with a COV of 8.7%.

Figure 43 shows the storage shear modulus of PLA/wood material during the cooling cycle at a cooling rate of 1°C/min at an oscillation frequency of 0.1 Hz. The shear modulus increases with decreasing temperature. There is a sudden increase at 60°C which marks the glass transition temperature of the material.

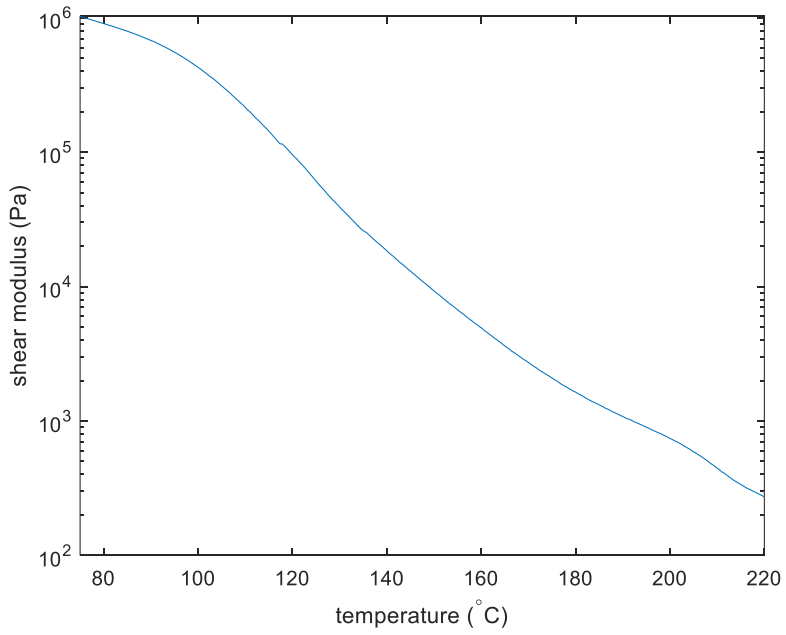

Figure 43: Storage shear modulus of PLA/wood material during the cooling cycle.

Figure 44 shows the tan δ for the PLA/wood material used for the study. The tan δ values are used for determining the viscoelastic state of the material at a given temperature. The material is in the viscoelastic liquid region from 220°C to 120°C, in the viscoelastic solid region below 120°C. This model uses Maxwell-type elements to determine the non-recoverable viscous deformation of the material in the viscoelastic region of the material behavior. The deformation in the viscoelastic solid and the elastic solid region of the material behavior is ignored. The elastic deformation is recoverable and has a negligible effect on the collapsing behavior of the 3D printed material during molten material deposition.

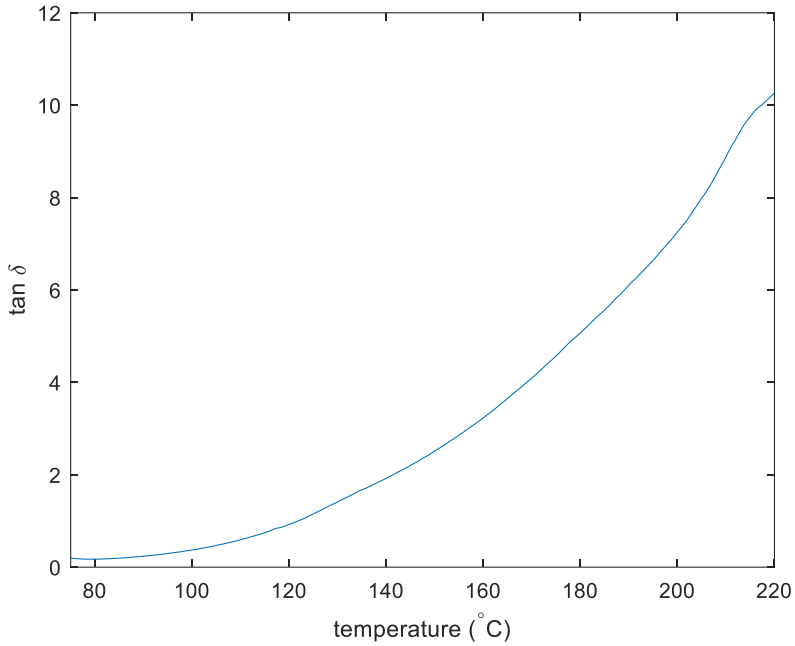

Figure 44: Tan δ for PLA/wood material during the cooling cycle.

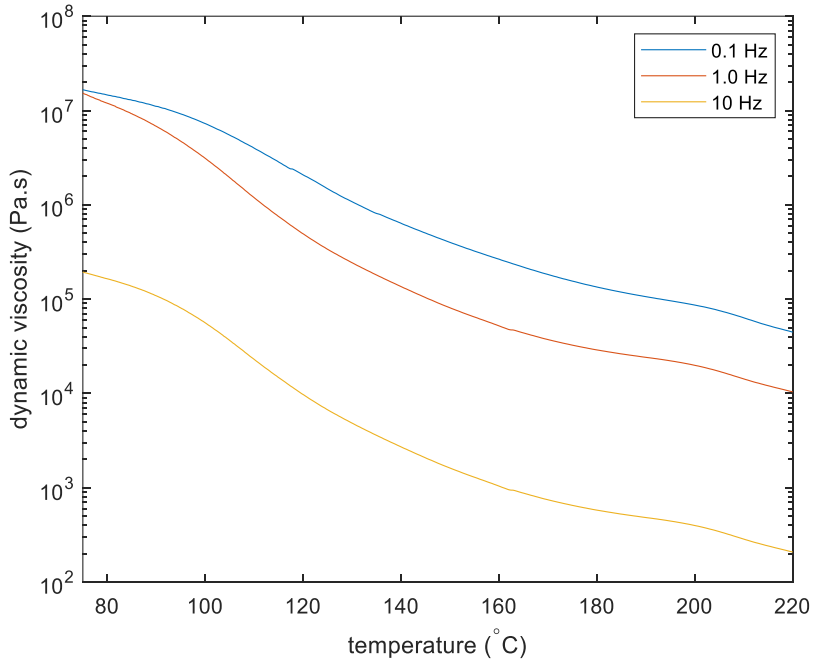

Figure 45: Viscosity of PLA/wood material during the cooling cycle.

Figure 45 shows the viscosity of PLA/wood material during the cooling cycle at a cooling rate of 1°C/min measured using DMA in shear mode. The viscosity increases with decreasing temperature. The viscosity

increases with decreasing shear rate. The shear rate of 0.1 Hz is adopted as zero-shear viscosity for this study.

The temperature-dependent material properties for this study were chosen for the cooling cycle because the viscous deformation that can lead to the collapse of the material occurs during the cooling cycle after the material is deposited.

5.4.2 Mesh convergence study

Figure 46 shows the maximum strain in the z-direction vs the number of elements in the model. The maximum strain for the entire model in the z-direction ($\varepsilon_{z,max}$) can be seen to be converging with the increasing number of elements. There is a -0.0362% change in $\varepsilon_{z,max}$ when the number of elements is increased from 311456 to 1051164 compared to -0.3611% change in $\varepsilon_{z,max}$ when the number of elements is increased from 38932 to 311456 elements.

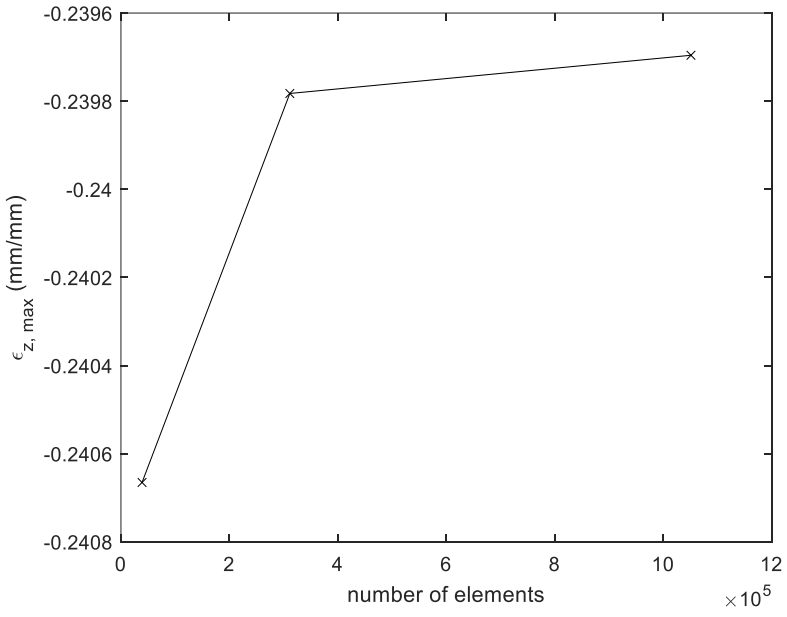

Figure 46: Mesh convergence study for the model with 205°C and 27.3 kg/hr extrusion rate.

5.4.3 Model predictions

Figure 47 shows the results from simulation for maximum strain in the z-direction vs extrusion rate at different extrusion temperatures. The black cross marks show the simulation results for the temperature and extrusion rates at which the test parts were printed. The red line marks the acceptable non-recoverable viscous strain of 10% as recommended by Duty et. al [183]. The low-fidelity numerical model predicts that the combination of extrusion rate and temperature below the red line will result in print failure due to the collapse of the layers. The model predicts that printing at 36.4 kg/hr (143 s layer time) and 27.3 kg/hr (190 s layer time) at 200°C will result in a print failure while printing at 18.2 kg/hr (285 s layer time) at 210°C will prevent the collapse of layers due to slow printing speed.

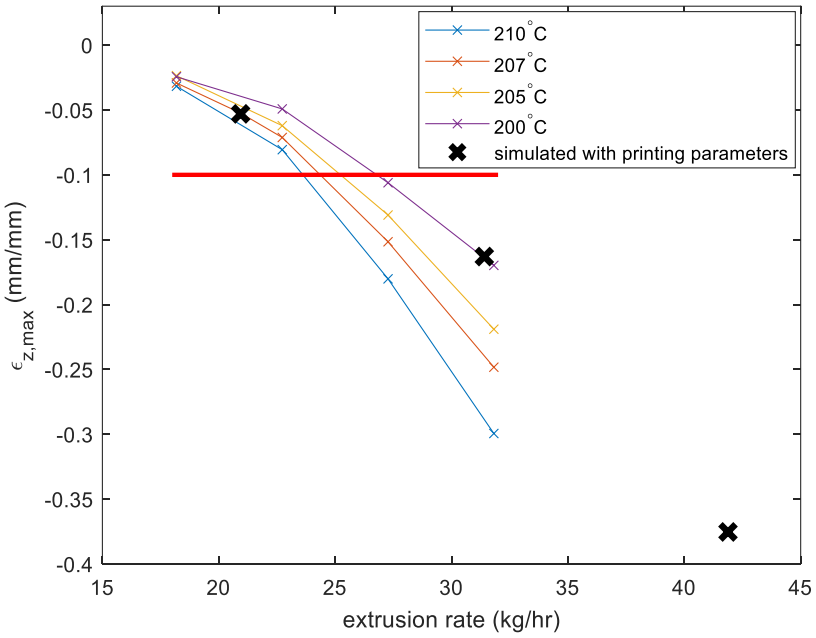

Figure 47: Maximum strain in the z-direction vs extrusion rate at different temperatures.

Figure 48 shows the histogram of strains in the z-direction for all elements at the different printing conditions that were carried out in the verification experiments. Figure 48a shows the histogram for an extrusion temperature of 210°C and a layer time of 285 s. Figure 48b shows the histogram for an

extrusion temperature of 200°C and a layer time of 190 s. Figure 48c shows the histogram from an extrusion temperature of 200°C and a layer time of 143 s. It can be observed that increasing the layer time reduces the maximum viscous strain in the z-direction.

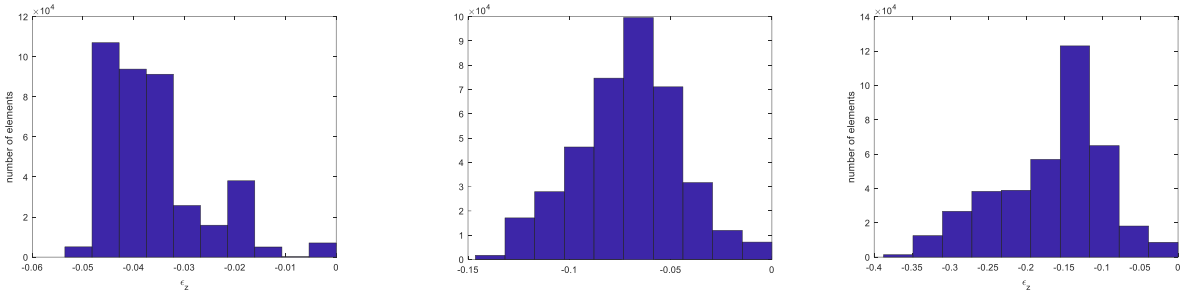

a) *207°C, 285 s.* b) *200°C, 190 s.* c) *200°C, 143 s.*

Figure 48: Histograms of strains in the z-direction for all elements at different test printing conditions.

Figure 49a shows the temperature-time history of the first element that exceeds the 10% total strain for an extrusion temperature of 200°C and a layer time of 143 seconds. Figure 49c shows the temperature-time history of the first element that undergoes the 10% viscous strain for an extrusion temperature of 200°C and a layer time of 190 seconds. A small reheating peak is observed in both figures after the layer time has elapsed when a layer is deposited over the element. The rate of cooling also decreases as free surfaces facilitating convection are covered by the deposition of layers next to the surface. Figure 49b and Figure 49d show the viscous strain accumulation in the first element that exceeds the 10% viscous strain for extrusion temperatures/layer times of 200°C/143 seconds and 200°C/190 seconds respectively. Four distinct regions can be observed in the curves. The first region is the viscous deformation of the layer under its self-weight. The material is hotter and has less viscosity during the initial phase. The material cools down considerably and has increased viscosity and starts to deform at a slower rate with time. The second and the third region are marked by a sudden increase in the viscous deformation rate as a layer of material is deposited over the element in consideration. The deposited layers increase the temperature, thus reducing viscosity, as well as increasing the load over the element,

increasing the rate of deformation of the material. The fourth region begins when the material has cooled down to a point where the tanδ of the material goes below 1. The material behavior changes to viscoelastic solid and the strains are recoverable as the material cools down. The numerical model implemented does not account for the elastic strains and the accumulated viscous strains remain constant.

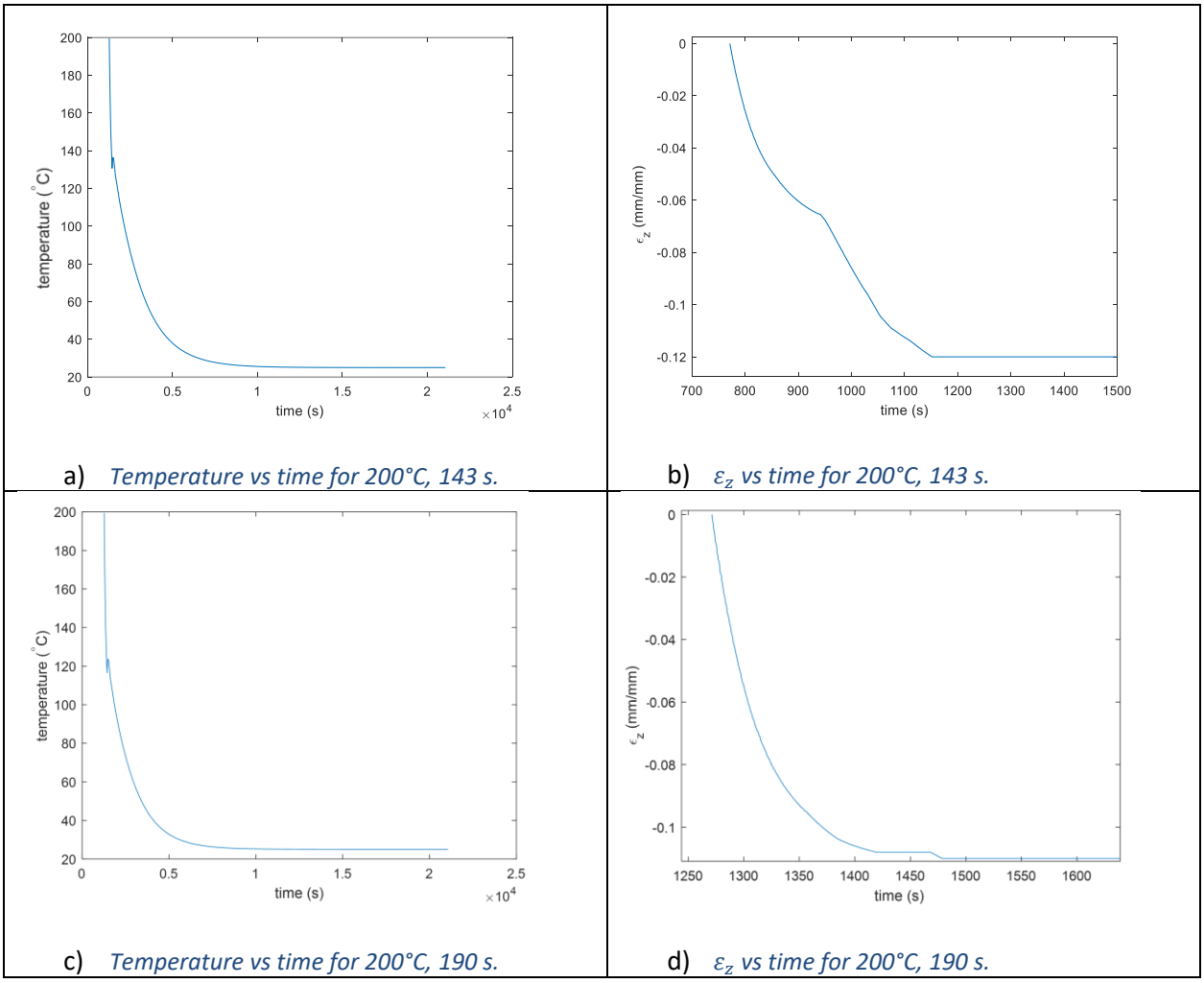

a) *Temperature vs time for 200°C, 143 s.*

b) *ε_z vs time for 200°C, 143 s.*

c) *Temperature vs time for 200°C, 190 s.*

d) *ε_z vs time for 200°C, 190 s.*

Figure 49: Temperature vs time and strain vs time for the first element to cross the failure criteria.

Figure 50 shows the accumulated viscous strain in the additively manufactured part for different layer times. The elements that are deposited later tend to have higher viscous strain in the z-direction compared to the elements that are deposited earlier. The farther away the elements are from the

printing bed, the slower they cool down. In fact, the printing bed acts as a heat sink, which cools down faster the elements near it. Consequently, the viscosity of the layers that are deposited later remains higher for an extended period of time, resulting in higher viscous deformation. Figure 50a and Figure 50b show the average viscous strain in each layer vs the layer number in the additively manufactured part. The trend can be seen more clearly with the higher layer having greater viscous strain in the z-direction. The final few layers have a lower strain as they have fewer layers above them and consequently withstand a lesser load.

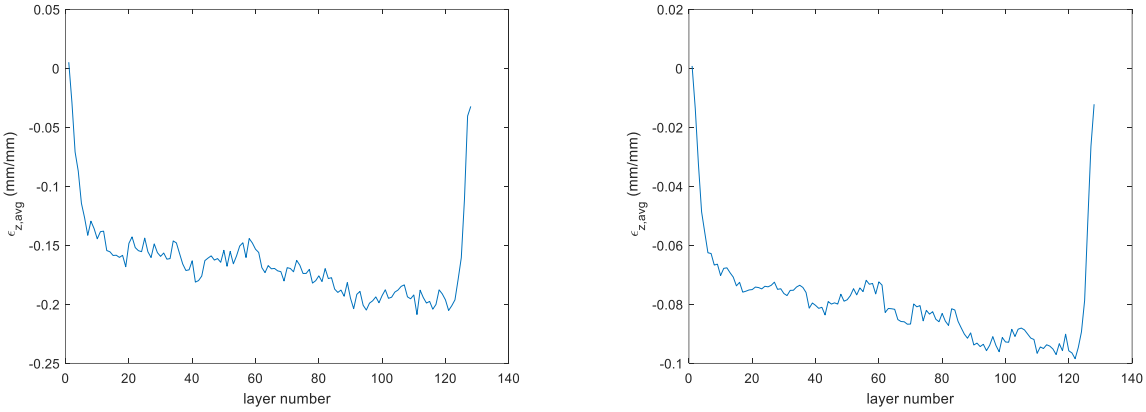

a) *Average viscous strain in layer vs layer number for 200°C, 143 s.*

d) *Average viscous strain in layer vs strain in layer vs layer number for 200°C, 190 s.*

Figure 50: Viscous strain in the additively manufactured part for different layer times.

5.4.4 Validation test results

Figure 51 shows the print failure caused by the collapse of layers caused due to high viscous strains printing at 200°C extrusion temperature, 190 s layer time, and at 200°C extrusion temperature, 143 s layer time. The failure occurs at a higher layer in the part printed at 90s layer time, at a later time of deposition, compared to the part printed with a layer time of 143 s.

a) *200°C, 143 s.*

b) *200°C, 190 s.*

Figure 51: Print failure caused by the collapse of the layer due to high viscous strain.

The 3D model was modified to create a continuous path connecting four segments of the culvert diffuser while maintaining the reduced extrusion rate (18.2kg/hr) and the corresponding increased layer time (285 s).

Figure 52: Final printed part with extrusion temperature 207°C and layer time 285s.

5.5 Conclusions

The following conclusions were drawn from the research work:

1. The collapse of extruded layers due to self-weight in a large-scale additively manufactured part of PLA/wood polymer composite can be prevented by using a fast low-fidelity numerical procedure.

2. A discrete element thermal model sequentially coupled with a finite element mechanical model can be used to evaluate a pass/fail criterion on whether a print will fail due to excessive viscous strains for a given combination of layer time and extrusion temperature for extrusion-based large scale additive manufacturing.
3. The sequentially coupled thermo-mechanical model can be used to determine a suitable layer time and extrusion temperature for a part with a given deposition toolpath.
4. The extruded thermoplastic material in a layer that is farther away from the print bed undergoes higher viscous strain as it cools slower and remains at a lower viscosity for a longer period of time.

CHAPTER 6
CONCLUSIONS AND RECOMMENDATIONS

The following conclusions have been drawn from the research works carried out in this dissertation.

Conclusion 1: Among the orthotropic mechanical properties in thermoplastic composites AM parts, the interlayer mechanical properties are the lowest. The cooling down of the deposited material and the consequent increase in viscosity causes incomplete diffusion bonding between the beads across layers. The addition of carbon fibers to the thermoplastics increases the melt viscosity and slows the diffusion bonding process, resulting in further reduction of interlayer mechanical properties. Annealing of the AM parts aids the diffusion bonding process and hence enhances their interlayer mechanical properties. Amorphous polymer AM parts should be annealed above their glass transition temperature. Semi-crystalline polymer AM parts should be annealed above their glass transition temperature and below their cold-crystallization temperature.

Recommendation 1: The orthotropic properties of polymer extrusion-based parts are not only feedstock material based but are also process-dependent. Processing parameters like printing speed, extrusion temperature, beadwidth, and beadheight. Postprocessing techniques like annealing can further change the mechanical properties. Numerical modeling of the AM parts requires the orthotropic material properties of the AM part as an input. An approach to obtain the material properties as input for the finite element model could be the experimental evaluation of test coupons to generate orthotropic material properties.

Conclusion 2: The orthotropic mechanical properties of thermoplastic extrusion-based AM parts can be modeled by experimentally evaluating homogenized properties from coupon testing. Some AM polymer composites, for example, short carbon fiber reinforced ABS parts, exhibit different compressive and tensile modulus. Such bimodular nature of the parts affects its bending behavior and can be simulated

using laminate analysis-based finite element modeling. The failure of such AM parts under bending loads can be modeled using Hill's yield criteria.

Recommendation 2: The experimentally derived homogenized orthotropic mechanical properties might not be suitable for the AM parts with varying process parameters or for the AM parts with complex geometry. Since the degree of bonding between the extruded beads depends on the temperature history of the beads, locations of the AM part with different temperature histories end up having different mechanical properties. A numerical thermal model can generate a temperature history of a 3D printed part based on the processing parameters and the part geometry. The thermal history generated can be used to make predictions about the variabilities in mechanical properties within the AM parts.

Conclusion 3: The deposition of material during manufacturing in an AM part can be simulated as a series of discrete events. The temperature histories at different locations of the part can be simulated using an explicit finite difference solution to the partial differential equation that governs heat flow. The accuracy of the results obtained from the DES-driven explicit finite difference analysis is comparable to the results obtained from finite element analysis. The DES model is more computationally efficient at generating the thermal histories of AM part. It can also effectively use temperature-dependent and orthotropic material properties.

Recommendation 3: The DES thermal model can be coupled with a mechanical model to determine the deformation and stresses in the AM part. A finite element model coupled with the DES thermal model could be used to evaluate the deformations and residual stresses in the AM part.

Conclusion 4: A sequentially coupled explicit DES thermal and implicit finite element mechanical analysis can be used as a low-fidelity model that can predict the occurrence of excessive viscous deformation in the deposited layer of material. The mechanical finite element model can be simplified to only include

the small set of elements that are actively undergoing viscous deformation as they are at a higher temperature. The efficient low-fidelity thermo-mechanical model can be used to determine a suitable set of processing parameters of extrusion rate and extrusion temperature that will avoid excessive non-recoverable viscoelastic deformation.

Recommendation 4: A high-fidelity finite element mechanical model can be used to accurately evaluate the large viscous deformations that occur until the part cools down to the temperature where the tan δ of the material is less than 1. Since large deformations can occur during the time the tan δ of the material is above 1, the deformations calculated might have significant errors. A remeshing technique needs to be used for the finite element model to compensate for the large viscous deformations. Alternatively, a numerical method that can handle large deformations, e.g. material point method, could be used to account for large viscous deformations. The elastic deformation and the residual stress when the part cools down to ambient temperature can also be calculated using the high-fidelity numerical method. All deposited elements need to be considered in such a mechanical finite element model to get accurate residual stresses and deformations.

BIBLIOGRAPHY

[1] A. Internatinal, ISO / ASTM52900-15, Standard Terminology for Additive Manufacturing – General Principles – Terminology, West Conshohocken, PA, 2015.

[2] T. Wohlers, Rapid Prototyping, Tooling & Manufacturing State of the Industry Wohlers Associated, Inc., 2005.

[3] V. Zukas, J.A. Zukas, An introduction to 3D printing, First Edition Design Pub.2015.

[4] Y.H. Chen, C.T. Ng, Y.Z. Wang, Generation of an STL File from 3D Measurement Data with User-Controlled Data Reduction, The International Journal of Advanced Manufacturing Technology 15(2) (1999) 127-131.

[5] I. Stroud, P. Xirouchakis, STL and extensions, Advances in Engineering Software 31(2) (2000) 83-95.

[6] J.D. Hiller, H. Lipson, STL 2.0: a proposal for a universal multi-material additive manufacturing file format, Proceedings of the Solid Freeform Fabrication Symposium, Citeseer, 2009, pp. 266-278.

[7] X. Wang, M. Jiang, Z. Zhou, J. Gou, D. Hui, 3D printing of polymer matrix composites: A review and prospective, Composites Part B: Engineering 110 (2017) 442-458.

[8] Y. Qin, Q. Qi, P.J. Scott, X. Jiang, Status, comparison, and future of the representations of additive manufacturing data, Computer-Aided Design 111 (2019) 44-64.

[9] D. Zhao, W. Guo, Shape and Performance Controlled Advanced Design for Additive Manufacturing: A Review of Slicing and Path Planning, Journal of Manufacturing Science and Engineering 142(1) (2020).

[10] J.C. Steuben, A.P. Iliopoulos, J.G. Michopoulos, Implicit slicing for functionally tailored additive manufacturing, Computer-Aided Design 77 (2016) 107-119.

[11] L. Zeng, L.M.-L. Lai, D. Qi, Y.-H. Lai, M.M.-F. Yuen, Efficient slicing procedure based on adaptive layer depth normal image, Computer-Aided Design 43(12) (2011) 1577-1586.

[12] R. Minetto, N. Volpato, J. Stolfi, R.M.M.H. Gregori, M.V.G. da Silva, An optimal algorithm for 3D triangle mesh slicing, Computer-Aided Design 92 (2017) 1-10.

[13] C. Wu, C. Dai, G. Fang, Y.-J. Liu, C.C. Wang, RoboFDM: A robotic system for support-free fabrication using FDM, 2017 IEEE International Conference on Robotics and Automation (ICRA), IEEE, 2017, pp. 1175-1180.

[14] K. Castelli, H. Giberti, Simulation of a robotic arm for multi-directional 3D printing, Sim-AM 2019: II International Conference on Simulation for Additive Manufacturing, CIMNE, 2019, pp. 120-129.

[15] Y. Yang, J.Y.H. Fuh, H.T. Loh, Y.S. Wong, Multi-orientational deposition to minimize support in the layered manufacturing process, Journal of Manufacturing Systems 22(2) (2003) 116-129.

[16] B. Huang, S. Singamneni, Curved Layer Fused Deposition Modeling with Varying Raster Orientations, Applied Mechanics and Materials 446-447 (2013) 263-269.

[17] J. Huang, Q. Chen, H. Jiang, B. Zou, L. Li, J. Liu, H. Yu, A survey of design methods for material extrusion polymer 3D printing, Virtual and Physical Prototyping 15(2) (2020) 148-162.

[18] M.R. Dunlavey, Efficient polygon-filling algorithms for raster displays, ACM Transactions on Graphics 2(4) (1983) 264-273.

[19] V.T. Rajan, V. Srinivasan, K.A. Tarabanis, The optimal zigzag direction for filling a two-dimensional region, Rapid Prototyping Journal 7(5) (2001) 231-241.

[20] S.C. Park, B.K. Choi, Tool-path planning for direction-parallel area milling, Computer-Aided Design 32(1) (2000) 17-25.

[21] M. Bertoldi, M. Yardimci, C. Pistor, S. Guceri, Domain decomposition and space filling curves in toolpath planning and generation, 1998 International Solid Freeform Fabrication Symposium, 1998.

[22] Y. Jin, Y. He, A. Shih, Process Planning for the Fuse Deposition Modeling of Ankle-Foot-Othoses, Procedia CIRP 42 (2016) 760-765.

[23] Y. Jin, Y. He, G. Fu, A. Zhang, J. Du, A non-retraction path planning approach for extrusion-based additive manufacturing, Robotics and Computer-Integrated Manufacturing 48 (2017) 132-144.

[24] T. Llewellyn-Jones, R. Allen, R. Trask, Curved Layer Fused Filament Fabrication Using Automated Toolpath Generation, 3D Print Addit Manuf 3(4) (2016) 236-243.

[25] D. Popescu, A. Zapciu, C. Amza, F. Baciu, R. Marinescu, FDM process parameters influence over the mechanical properties of polymer specimens: A review, Polymer Testing 69 (2018) 157-166.

[26] M. Samykano, S.K. Selvamani, K. Kadirgama, W.K. Ngui, G. Kanagaraj, K. Sudhakar, Mechanical property of FDM printed ABS: influence of printing parameters, The International Journal of Advanced Manufacturing Technology 102(9-12) (2019) 2779-2796.

[27] A.W. Gebisa, H.G. Lemu, Influence of 3D Printing FDM Process Parameters on Tensile Property of ULTEM 9085, Procedia Manufacturing 30 (2019) 331-338.

[28] V.E. Kuznetsov, A.N. Solonin, A. Tavitov, O. Urzhumtsev, A. Vakulik, Increasing strength of FFF three-dimensional printed parts by influencing on temperature-related parameters of the process, Rapid Prototyping Journal (2020).

[29] L. Zhang, H.W. Zhang, J. Wu, B. Yan, A stabilized complementarity formulation for nonlinear analysis of 3D bimodular materials, Acta Mechanica Sinica 32(3) (2015) 481-490.

[30] K.S. Kumar, R. Soundararajan, G. Shanthosh, P. Saravanakumar, M. Ratteesh, Augmenting effect of infill density and annealing on mechanical properties of PETG and CFPETG composites fabricated by FDM, Materials Today: Proceedings 45 (2021) 2186-2191.

[31] J. Beniak, P. Križan, Ľ. Šooš, M. Matúš, Research on shape and dimensional accuracy of FDM produced parts, IOP Conference Series: Materials Science and Engineering, IOP Publishing, 2019, p. 012030.

[32] O.E. Akbaş, O. Hıra, S.Z. Hervan, S. Samankan, A. Altınkaynak, Dimensional accuracy of FDM-printed polymer parts, Rapid Prototyping Journal (2019).

[33] S. A. Gold, R. Strong, B. N. Turner, A review of melt extrusion additive manufacturing processes: I. Process design and modeling, Rapid Prototyping Journal 20(3) (2014) 192-204.

[34] J. Shah, B. Snider, T. Clarke, S. Kozutsky, M. Lacki, A. Hosseini, Large-scale 3D printers for additive manufacturing: design considerations and challenges, The International Journal of Advanced Manufacturing Technology 104(9-12) (2019) 3679-3693.

[35] Krishnanand, S. Soni, M. Taufik, Design and assembly of fused filament fabrication (FFF) 3D printers, Materials Today: Proceedings (2020).

[36] C.E. Duty, V. Kunc, B. Compton, B. Post, D. Erdman, R. Smith, R. Lind, P. Lloyd, L. Love, Structure and mechanical behavior of Big Area Additive Manufacturing (BAAM) materials, Rapid Prototyping Journal 23(1) (2017) 181-189.

[37] S. Bhandari, R.A. Lopez-Anido, Discrete-Event Simulation Thermal Model for Extrusion-Based Additive Manufacturing of PLA and ABS, Materials (Basel) 13(21) (2020).

[38] V. Mazzanti, L. Malagutti, F. Mollica, FDM 3D Printing of Polymers Containing Natural Fillers: A Review of their Mechanical Properties, Polymers (Basel) 11(7) (2019).

[39] Y. Wang, Y. Zhou, L. Lin, J. Corker, M. Fan, Overview of 3D additive manufacturing (AM) and corresponding AM composites, Composites Part A: Applied Science and Manufacturing 139 (2020) 106114.

[40] S.M.F. Kabir, K. Mathur, A.-F.M. Seyam, A critical review on 3D printed continuous fiber-reinforced composites: History, mechanism, materials and properties, Composite Structures 232 (2020) 111476.

[41] P. Parandoush, L. Tucker, C. Zhou, D. Lin, Laser assisted additive manufacturing of continuous fiber reinforced thermoplastic composites, Materials & Design 131 (2017) 186-195.

[42] T. Hofstätter, D.B. Pedersen, G. Tosello, H.N. Hansen, State-of-the-art of fiber-reinforced polymers in additive manufacturing technologies, Journal of Reinforced Plastics and Composites 36(15) (2017) 1061-1073.

[43] S. Dul, L. Fambri, A. Pegoretti, Filaments Production and Fused Deposition Modelling of ABS/Carbon Nanotubes Composites, Nanomaterials (Basel) 8(1) (2018).

[44] A.A. D'Amico, A. Debaie, A.M. Peterson, Effect of layer thickness on irreversible thermal expansion and interlayer strength in fused deposition modeling, Rapid Prototyping Journal 23(5) (2017) 943-953.

[45] L.J. Love, V. Kunc, O. Rios, C.E. Duty, A.M. Elliott, B.K. Post, R.J. Smith, C.A. Blue, The importance of carbon fiber to polymer additive manufacturing, Journal of Materials Research 29(17) (2014) 1893-1898.

[46] L.J. Tan, W. Zhu, K. Zhou, Recent Progress on Polymer Materials for Additive Manufacturing, Advanced Functional Materials 30(43) (2020) 2003062.

[47] J.M. Chacón, M.A. Caminero, E. García-Plaza, P.J. Núñez, Additive manufacturing of PLA structures using fused deposition modelling: Effect of process parameters on mechanical properties and their optimal selection, Materials & Design 124 (2017) 143-157.

[48] S. Singh, S. Ramakrishna, F. Berto, 3D Printing of polymer composites: A short review, Material Design & Processing Communications 2(2) (2019).

[49] S. Wickramasinghe, T. Do, P. Tran, FDM-Based 3D Printing of Polymer and Associated Composite: A Review on Mechanical Properties, Defects and Treatments, Polymers (Basel) 12(7) (2020).

[50] V. Kishore, C. Ajinjeru, A. Nycz, B. Post, J. Lindahl, V. Kunc, C. Duty, Infrared preheating to improve interlayer strength of big area additive manufacturing (BAAM) components, Additive Manufacturing 14 (2017) 7-12.

[51] D. Moreno Nieto, S.I. Molina, Large-format fused deposition additive manufacturing: a review, Rapid Prototyping Journal 26(5) (2019) 793-799.

[52] A.R. Torrado, D.A. Roberson, Failure Analysis and Anisotropy Evaluation of 3D-Printed Tensile Test Specimens of Different Geometries and Print Raster Patterns, Journal of Failure Analysis and Prevention 16(1) (2016) 154-164.

[53] S. Shaffer, K. Yang, J. Vargas, M.A. Di Prima, W. Voit, On reducing anisotropy in 3D printed polymers via ionizing radiation, Polymer 55(23) (2014) 5969-5979.

[54] M. Somireddy, C.V. Singh, A. Czekanski, Analysis of the Material Behavior of 3D Printed Laminates Via FFF, Experimental Mechanics 59(6) (2019) 871-881.

[55] S. Bhandari, R.A. Lopez-Anido, L. Wang, D.J. Gardner, Elasto-Plastic Finite Element Modeling of Short Carbon Fiber Reinforced 3D Printed Acrylonitrile Butadiene Styrene Composites, Jom 72(1) (2019) 475-484.

[56] S.H. Ahn, M. Montero, D. Odell, S. Roundy, P.K. Wright, Anisotropic material properties of fused deposition modeling ABS, Rapid prototyping journal (2002).

[57] R.T.L. Ferreira, I.C. Amatte, T.A. Dutra, D. Bürger, Experimental characterization and micrography of 3D printed PLA and PLA reinforced with short carbon fibers, Composites Part B: Engineering 124 (2017) 88-100.

[58] M.A. Caminero, J.M. Chacón, I. García-Moreno, J.M. Reverte, Interlaminar bonding performance of 3D printed continuous fibre reinforced thermoplastic composites using fused deposition modelling, Polymer Testing 68 (2018) 415-423.

[59] R.J. Zaldivar, D.B. Witkin, T. McLouth, D.N. Patel, K. Schmitt, J.P. Nokes, Influence of processing and orientation print effects on the mechanical and thermal behavior of 3D-Printed ULTEM® 9085 Material, Additive Manufacturing 13 (2017) 71-80.

[60] W. Zhang, C. Cotton, J. Sun, D. Heider, B. Gu, B. Sun, T.-W. Chou, Interfacial bonding strength of short carbon fiber/acrylonitrile-butadiene-styrene composites fabricated by fused deposition modeling, Composites Part B: Engineering 137 (2018) 51-59.

[61] H.L. Tekinalp, V. Kunc, G.M. Velez-Garcia, C.E. Duty, L.J. Love, A.K. Naskar, C.A. Blue, S. Ozcan, Highly oriented carbon fiber–polymer composites via additive manufacturing, Composites Science and Technology 105 (2014) 144-150.

[62] D. Jiang, D.E. Smith, Anisotropic mechanical properties of oriented carbon fiber filled polymer composites produced with fused filament fabrication, Additive Manufacturing 18 (2017) 84-94.

[63] S. Hwang, E.I. Reyes, K.-s. Moon, R.C. Rumpf, N.S. Kim, Thermo-mechanical Characterization of Metal/Polymer Composite Filaments and Printing Parameter Study for Fused Deposition Modeling in the 3D Printing Process, Journal of Electronic Materials 44(3) (2014) 771-777.

[64] C. Duty, J. Failla, S. Kim, T. Smith, J. Lindahl, V. Kunc, Z-Pinning approach for 3D printing mechanically isotropic materials, Additive Manufacturing 27 (2019) 175-184.

[65] P.G. de Gennes, Reptation of a Polymer Chain in the Presence of Fixed Obstacles, The Journal of Chemical Physics 55(2) (1971) 572-579.

[66] Y.H. Kim, R.P. Wool, A theory of healing at a polymer-polymer interface, Macromolecules 16(7) (1983) 1115-1120.

[67] L. Woo Il, G.S. Springer, A Model of the Manufacturing Process of Thermoplastic Matrix Composites, Journal of Composite Materials 21(11) (1987) 1017-1055.

[68] Q. Sun, G.M. Rizvi, C.T. Bellehumeur, P. Gu, Effect of processing conditions on the bonding quality of FDM polymer filaments, Rapid Prototyping Journal 14(2) (2008) 72-80.

[69] T.J. Coogan, D.O. Kazmer, Healing simulation for bond strength prediction of FDM, Rapid Prototyping Journal 23(3) (2017) 551-561.

[70] P.C. Chesser, R.F. Lind, B.K. Post, A.C. Roschli, L.J. Love, K.T. Gaul, Using post-tensioning in large scale additive parts for load bearing structures, Oak Ridge National Lab.(ORNL), Oak Ridge, TN (United States), 2018.

[71] W.S. Yerazunis, J.C. Barnwell III, D.N. Nikovski, Strengthening ABS, nylon, and polyester 3D printed parts by stress tensor aligned deposition paths and five-axis printing, Proceedings of the Solid Freeform Fabrication Symposium, AT&T Conference Center, Austin, Texas, 2016.

[72] C.B. Sweeney, B.A. Lackey, M.J. Pospisil, T.C. Achee, V.K. Hicks, A.G. Moran, B.R. Teipel, M.A. Saed, M.J. Green, Welding of 3D-printed carbon nanotube-polymer composites by locally induced microwave heating, Sci Adv 3(6) (2017) e1700262.

[73] A.K. Ravi, A. Deshpande, K.H. Hsu, An in-process laser localized pre-deposition heating approach to inter-layer bond strengthening in extrusion based polymer additive manufacturing, Journal of Manufacturing Processes 24 (2016) 179-185.

[74] A. Deshpande, A. Ravi, S. Kusel, R. Churchwell, K. Hsu, Interlayer thermal history modification for interface strength in fused filament fabricated parts, Progress in Additive Manufacturing 4(1) (2018) 63-70.

[75] M. Faes, E. Ferraris, D. Moens, Influence of Inter-layer Cooling time on the Quasi-static Properties of ABS Components Produced via Fused Deposition Modelling, Procedia CIRP 42 (2016) 748-753.

[76] T. Takayama, M. Todo, H. Tsuji, Effect of annealing on the mechanical properties of PLA/PCL and PLA/PCL/LTI polymer blends, J Mech Behav Biomed Mater 4(3) (2011) 255-60.

[77] D. Bassett, R. Olley, I. Alraheil, On crystallization phenomena in PEEK☆, Polymer 29(10) (1988) 1745-1754.

[78] B. Wittbrodt, J.M. Pearce, The effects of PLA color on material properties of 3-D printed components, Additive Manufacturing 8 (2015) 110-116.

[79] C. Yang, X. Tian, D. Li, Y. Cao, F. Zhao, C. Shi, Influence of thermal processing conditions in 3D printing on the crystallinity and mechanical properties of PEEK material, Journal of Materials Processing Technology 248 (2017) 1-7.

[80] C. Benwood, A. Anstey, J. Andrzejewski, M. Misra, A.K. Mohanty, Improving the Impact Strength and Heat Resistance of 3D Printed Models: Structure, Property, and Processing Correlationships during Fused Deposition Modeling (FDM) of Poly(Lactic Acid), ACS Omega 3(4) (2018) 4400-4411.

[81] B.S. Thakkar, L.J. Broutman, Impact strength of polymers. 3: The effect of annealing on cold worked polycarbonates, Polymer Engineering and Science 21(3) (1981) 155-162.

[82] Y. Song, Y. Li, W. Song, K. Yee, K.Y. Lee, V.L. Tagarielli, Measurements of the mechanical response of unidirectional 3D-printed PLA, Materials & Design 123 (2017) 154-164.

[83] A. Kantaros, D. Karalekas, Fiber Bragg grating based investigation of residual strains in ABS parts fabricated by fused deposition modeling process, Materials & Design 50 (2013) 44-50.

[84] C. Casavola, A. Cazzato, V. Moramarco, G. Pappalettera, Residual stress measurement in Fused Deposition Modelling parts, Polymer Testing 58 (2017) 249-255.

[85] B. Brenken, E. Barocio, A. Favaloro, V. Kunc, R.B. Pipes, Fused filament fabrication of fiber-reinforced polymers: A review, Additive Manufacturing 21 (2018) 1-16.

[86] C. Bellehumeur, L. Li, Q. Sun, P. Gu, Modeling of Bond Formation Between Polymer Filaments in the Fused Deposition Modeling Process, Journal of Manufacturing Processes 6(2) (2004) 170-178.

[87] K.R. Hart, R.M. Dunn, J.M. Sietins, C.M. Hofmeister Mock, M.E. Mackay, E.D. Wetzel, Increased fracture toughness of additively manufactured amorphous thermoplastics via thermal annealing, Polymer 144 (2018) 192-204.

[88] C. McIlroy, P.D. Olmsted, Disentanglement effects on welding behaviour of polymer melts during the fused-filament-fabrication method for additive manufacturing, Polymer 123 (2017) 376-391.

[89] C. McIlroy, P.D. Olmsted, Deformation of an amorphous polymer during the fused-filament-fabrication method for additive manufacturing, Journal of Rheology 61(2) (2017) 379-397.

[90] ASTM, D638-14: Standard test method for tensile properties of plastics. ASTM International, West Conshohocken, PA.

[91] E.W. Fischer, H.J. Sterzel, G. Wegner, Investigation of the structure of solution grown crystals of lactide copolymers by means of chemical reactions, Kolloid-Zeitschrift und Zeitschrift für Polymere 251(11) (1973) 980-990.

[92] R. Vadori, A.K. Mohanty, M. Misra, The Effect of Mold Temperature on the Performance of Injection Molded Poly(lactic acid)-Based Bioplastic, Macromolecular Materials and Engineering 298(9) (2013) 981-990.

[93] C.-C. Tsai, R.-J. Wu, H.-Y. Cheng, S.-C. Li, Y.-Y. Siao, D.-C. Kong, G.-W. Jang, Crystallinity and dimensional stability of biaxial oriented poly(lactic acid) films, Polymer Degradation and Stability 95(8) (2010) 1292-1298.

[94] Y. Srithep, P. Nealey, L.-S. Turng, Effects of annealing time and temperature on the crystallinity and heat resistance behavior of injection-molded poly(lactic acid), Polymer Engineering & Science 53(3) (2013) 580-588.

[95] Q. Fang, M.A. Hanna, Rheological properties of amorphous and semicrystalline polylactic acid polymers, Industrial Crops and Products 10(1) (1999) 47-53.

[96] T. Tabi, I.E. Sajo, F. Szabo, A.S. Luyt, J.G. Kovacs, Crystalline structure of annealed polylactic acid and its relation to processing, Express Polymer Letters 4(10) (2010) 659-668.

[97] T. Tábi, S. Hajba, J.G. Kovács, Effect of crystalline forms (α′ and α) of poly(lactic acid) on its mechanical, thermo-mechanical, heat deflection temperature and creep properties, European Polymer Journal 82 (2016) 232-243.

[98] M.R. Fazita, K. Jayaraman, D. Bhattacharyya, M. Hossain, M.K. Haafiz, A. H.P.S, Disposal Options of Bamboo Fabric-Reinforced Poly(Lactic) Acid Composites for Sustainable Packaging: Biodegradability and Recyclability, Polymers 7(8) (2015) 1476-1496.

[99] D. Kurniawan, B.S. Kim, H.Y. Lee, J.Y. Lim, Effect of Silane Treatment on Mechanical Properties of Basalt Fiber/Polylactic Acid Ecofriendly Composites, Polymer-Plastics Technology and Engineering 52(1) (2013) 97-100.

[100] F. Rezaei, R. Yunus, N.A. Ibrahim, Effect of fiber length on thermomechanical properties of short carbon fiber reinforced polypropylene composites, Materials & Design 30(2) (2009) 260-263.

[101] T. Kitano, T. Kataoka, T. Shirota, An empirical equation of the relative viscosity of polymer melts filled with various inorganic fillers, Rheologica Acta 20(2) (1981) 207-209.

[102] S. Prager, M. Tirrell, The healing process at polymer–polymer interfaces, The Journal of Chemical Physics 75(10) (1981) 5194-5198.

[103] T. Ge, M.O. Robbins, D. Perahia, G.S. Grest, Healing of polymer interfaces: Interfacial dynamics, entanglements, and strength, Phys Rev E Stat Nonlin Soft Matter Phys 90(1) (2014) 012602.

[104] G. Perego, G.D. Cella, C. Bastioli, Effect of molecular weight and crystallinity on poly(lactic acid) mechanical properties, Journal of Applied Polymer Science 59(1) (1996) 37-43.

[105] G. Liu, X. Zhang, D. Wang, Tailoring crystallization: towards high-performance poly(lactic acid), Adv Mater 26(40) (2014) 6905-11.

[106] S. Timoshenko, Strength of Materials, Part II: Advanced theory and problems, Van Nostrand Reinhold1958.

[107] C.W. Bert, C.J. Rebello, Bending of laminated thick beams of bimodular material, Engineering Structures 5(3) (1983) 227-231.

[108] C. Ziemian, M. Sharma, S. Ziemian, Anisotropic mechanical properties of ABS parts fabricated by fused deposition modelling, Mechanical engineering, InTechOpen2012.

[109] J.-y. Sun, H.-q. Zhu, S.-h. Qin, D.-l. Yang, X.-t. He, A review on the research of mechanical problems with different moduli in tension and compression, Journal of Mechanical Science and Technology 24(9) (2010) 1845-1854.

[110] C. Bert, Models for fibrous composites with different properties in tension and compression, Journal of Engineering Materials and Technology 99(4) (1977) 344-349.

[111] S. Ambartsumyan, A.A. Khachatryan, Basic Equation fo the Theory of Elasticity for Materials with Different Resistance to Tension and Compression, Mekhanika Tverdogo Tela 1 (1986) 44.

[112] M.E. Babeshko, Y.N. Shevchenko, Elastoplastic stress-strain state of flexible layered shells made of isotropic and transversely isotropic materials with different moduli and subjected to axisymmetric loading, International Applied Mechanics 43(11) (2007) 1208-1217.

[113] M. Shi, Y. Zhang, L. Cheng, Z. Jiao, W. Yang, J. Tan, Y. Ding, Interfacial Diffusion and Bonding in Multilayer Polymer Films: A Molecular Dynamics Simulation, J Phys Chem B 120(37) (2016) 10018-29.

[114] G. Alaimo, S. Marconi, L. Costato, F. Auricchio, Influence of meso-structure and chemical composition on FDM 3D-printed parts, Composites Part B: Engineering 113 (2017) 371-380.

[115] M. Somireddy, C.V. Singh, A. Czekanski, Analysis of the Material Behavior of 3D Printed Laminates Via FFF, Experimental Mechanics (2019).

[116] M. Destrade, M.D. Gilchrist, J.A. Motherway, J.G. Murphy, Bimodular rubber buckles early in bending, Mechanics of Materials 42(4) (2010) 469-476.

[117] S. Bhandari, R. Lopez-Anido, Finite element modeling of 3D-printed part with cellular internal structure using homogenized properties, Progress in Additive Manufacturing (2018).

[118] S. Bhandari, R. Lopez-Anido, Finite element analysis of thermoplastic polymer extrusion 3D printed material for mechanical property prediction, Additive Manufacturing 22 (2018) 187-196.

[119] H. Nouri, S. Guessasma, S. Belhabib, Structural imperfections in additive manufacturing perceived from the X-ray micro-tomography perspective, Journal of Materials Processing Technology 234 (2016) 113-124.

[120] S. Guessasma, S. Belhabib, H. Nouri, Printability and Tensile Performance of 3D Printed Polyethylene Terephthalate Glycol Using Fused Deposition Modelling, Polymers (Basel) 11(7) (2019).

[121] N. van de Werken, J. Hurley, P. Khanbolouki, A.N. Sarvestani, A.Y. Tamijani, M. Tehrani, Design considerations and modeling of fiber reinforced 3D printed parts, Composites Part B: Engineering 160 (2019) 684-692.

[122] M. Somireddy, A. Czekanski, C.V. Singh, Development of constitutive material model of 3D printed structure via FDM, Materials Today Communications 15 (2018) 143-152.

[123] K.-S. Liu, S.W. Tsai, A Progressive Quadratic Failure Criterion for a Laminate, Composites Science and Technology 58(7) (1998) 1023-1032.

[124] D. Notta-Cuvier, F. Lauro, B. Bennani, Modelling of progressive fibre/matrix debonding in short-fibre reinforced composites up to failure, International Journal of Solids and Structures 66 (2015) 140-150.

[125] P. Gotsis, C.C. Chamis, M. L., Prediction of composite laminate fracture: micromechanics and progressive fracture, Composites Science and Technology 58(7) (1998) 1137-1149.

[126] W.W. El-Tahan, G.H. Staab, S.H. Advani, J.K. Lee, Structural Analysis of Bimodular Materials, Journal of Engineering Mechanics 115(5) (1989) 963-981.

[127] L. Chen, W. Wen, H. Cui, Generalization of Hill's yield criterion to tension-compression asymmetry materials, Science China Technological Sciences 56(1) (2012) 89-97.

[128] L. Zhang, Q. Gao, H.W. Zhang, An efficient algorithm for mechanical analysis of bimodular truss and tensegrity structures, International Journal of Mechanical Sciences 70 (2013) 57-68.

[129] Z. Du, Y. Zhang, W. Zhang, X. Guo, A new computational framework for materials with different mechanical responses in tension and compression and its applications, International Journal of Solids and Structures 100-101 (2016) 54-73.

[130] F. Mollica, M. Ventre, F. Sarracino, L. Ambrosio, L. Nicolais, Implicit constitutive equations in the modeling of bimodular materials: An application to biomaterials, Computers & Mathematics with Applications 53(2) (2007) 209-218.

[131] H. Mehdipour, P.P. Camanho, G. Belingardi, Elasto-plastic constitutive equations for short fiber reinforced polymers, Composites Part B: Engineering 165 (2019) 199-214.

[132] A. Nanda, T. Kuppusamy, Three-dimensional elastic-plastic analysis of laminated composite plates, Composite Structures 17(3) (1991) 213-225.

[133] F. Dunne, N. Petrinic, Introduction to Computational Plasticity, illustrated, reprint ed., OUP Oxford 2005.

[134] A. Cattenone, S. Morganti, G. Alaimo, F. Auricchio, Finite Element Analysis of Additive Manufacturing Based on Fused Deposition Modeling: Distortions Prediction and Comparison With Experimental Data, Journal of Manufacturing Science and Engineering 141(1) (2019).

[135] B. Brenken, E. Barocio, A. Favaloro, V. Kunc, R.B. Pipes, Development and validation of extrusion deposition additive manufacturing process simulations, Additive Manufacturing 25 (2019) 218-226.

[136] J. Yin, C. Lu, J. Fu, Y. Huang, Y. Zheng, Interfacial bonding during multi-material fused deposition modeling (FDM) process due to inter-molecular diffusion, Materials & Design 150 (2018) 104-112.

[137] T.J. Coogan, D.O. Kazmer, Prediction of interlayer strength in material extrusion additive manufacturing, Additive Manufacturing 35 (2020) 101368.

[138] S. Bhandari, R.A. Lopez-Anido, D.J. Gardner, Enhancing the interlayer tensile strength of 3D printed short carbon fiber reinforced PETG and PLA composites via annealing, Additive Manufacturing 30 (2019) 100922.

[139] C. Casavola, A. Cazzato, D. Karalekas, V. Moramarco, G. Pappalettera, The Effect of Chamber Temperature on Residual Stresses of FDM Parts, (2019) 87-92.

[140] J.M. Barrios, P.E. Romero, Improvement of Surface Roughness and Hydrophobicity in PETG Parts Manufactured via Fused Deposition Modeling (FDM): An Application in 3D Printed Self-Cleaning Parts, Materials (Basel) 12(15) (2019).

[141] D. Pranzo, P. Larizza, D. Filippini, G. Percoco, Extrusion-Based 3D Printing of Microfluidic Devices for Chemical and Biomedical Applications: A Topical Review, Micromachines (Basel) 9(8) (2018).

[142] M. Harris, J. Potgieter, R. Archer, K.M. Arif, Effect of Material and Process Specific Factors on the Strength of Printed Parts in Fused Filament Fabrication: A Review of Recent Developments, Materials (Basel) 12(10) (2019).

[143] N.G. Tanikella, B. Wittbrodt, J.M. Pearce, Tensile strength of commercial polymer materials for fused filament fabrication 3D printing, Additive Manufacturing 15 (2017) 40-47.

[144] O.S. Carneiro, A.F. Silva, R. Gomes, Fused deposition modeling with polypropylene, Materials & Design 83 (2015) 768-776.

[145] L. Wang, D.J. Gardner, D.W. Bousfield, Cellulose nanofibril-reinforced polypropylene composites for material extrusion: Rheological properties, Polymer Engineering & Science 58(5) (2018) 793-801.

[146] P. Geng, J. Zhao, W. Wu, W. Ye, Y. Wang, S. Wang, S. Zhang, Effects of extrusion speed and printing speed on the 3D printing stability of extruded PEEK filament, Journal of Manufacturing Processes 37 (2019) 266-273.

[147] L.J. Love, C.E. Duty, B.K. Post, R.F. Lind, P.D. Lloyd, V. Kunc, W.H. Peter, C.A. Blue, Breaking barriers in polymer additive manufacturing, Oak Ridge National Lab.(ORNL), Oak Ridge, TN (United States). Manufacturing …, 2015.

[148] Y. Zhang, V. Shapiro, Linear-Time Thermal Simulation of As-Manufactured Fused Deposition Modeling Components, Journal of Manufacturing Science and Engineering 140(7) (2018).

[149] L. Wang, D.J. Gardner, Contribution of printing parameters to the interfacial strength of polylactic acid (PLA) in material extrusion additive manufacturing, Progress in Additive Manufacturing 3(3) (2018) 165-171.

[150] S. Solarski, M. Ferreira, E. Devaux, Characterization of the thermal properties of PLA fibers by modulated differential scanning calorimetry, Polymer 46(25) (2005) 11187-11192.

[151] N.W. Khun, E. Liu, Thermal, mechanical and tribological properties of polycarbonate/acrylonitrile-butadiene-styrene blends, Journal of Polymer Engineering 33(6) (2013) 535-543.

[152] A.C. Brown, D. de Beer, Development of a stereolithography (STL) slicing and G-code generation algorithm for an entry level 3-D printer, Africon, Pointe-Aux-Piments, 2013, pp. 1-5.

[153] G.W. Recktenwald, Finite-difference approximations to the heat equation, Mechanical Engineering 10 (2004) 1-27.

[154] Y. Zhou, H. Lu, G. Wang, J. Wang, W. Li, Voxelization modelling based finite element simulation and process parameter optimization for Fused Filament Fabrication, Materials & Design 187 (2020) 108409.

[155] S.T. Lee, L. Kareko, J. Jun, Study of Thermoplastic PLA Foam Extrusion, Journal of Cellular Plastics 44(4) (2008) 293-305.

[156] Z. Lule, J. Kim, Thermally conductive and highly rigid polylactic acid (PLA) hybrid composite filled with surface treated alumina/nano-sized aluminum nitride, Composites Part A: Applied Science and Manufacturing 124 (2019) 105506.

[157] A. El Moumen, M. Tarfaoui, K. Lafdi, Modelling of the temperature and residual stress fields during 3D printing of polymer composites, The International Journal of Advanced Manufacturing Technology 104(5-8) (2019) 1661-1676.

[158] J. Zhang, X.Z. Wang, W.W. Yu, Y.H. Deng, Numerical investigation of the influence of process conditions on the temperature variation in fused deposition modeling, Materials & Design 130 (2017) 59-68.

[159] C. Kousiatza, D. Karalekas, In-situ monitoring of strain and temperature distributions during fused deposition modeling process, Materials & Design 97 (2016) 400-406.

[160] S.F. Costa, F.M. Duarte, J.A. Covas, Towards modelling of Free Form Extrusion: analytical solution of transient heat transfer, International Journal of Material Forming 1(S1) (2008) 703-706.

[161] L.J. Love, C. Duty, Cincinnati big area additive manufacturing (BAAM), Oak Ridge, TN (2015).

[162] V. Kunc, A.A. Hassen, J. Lindahl, S. Kim, B. Post, L. Love, Large scale additively manufactured tooling for composites, Proceedings of 15th Japan International SAMPE Symposium and Exhibition, 2017.

[163] L. Love, 3D Printed Shelby Cobra, Oak Ridge National Lab.(ORNL), Oak Ridge, TN (United States), 2015.

[164] B.K. Post, P.C. Chesser, R.F. Lind, A. Roschli, L.J. Love, K.T. Gaul, M. Sallas, F. Blue, S. Wu, Using Big Area Additive Manufacturing to directly manufacture a boat hull mould, Virtual and Physical Prototyping 14(2) (2019) 123-129.

[165] S. Bhandari, R.A. Lopez-Anido, J. Anderson, Large Scale 3D Printed Thermoplastic Composite Forms for Precast Concrete Structures, ITHEC 2020, 5th International Conference & Exhibition on Thermoplastic Composites, Bremen, Germany, 2020, pp. 182-187.

[166] A.C. Roschli, B.K. Post, P.C. Chesser, M.R. Sallas, L.J. Love, K.T. Gaul, Precast concrete molds fabricated with big area additive manufacturing, Oak Ridge National Lab.(ORNL), Oak Ridge, TN (United States), 2018.

[167] D.J. Byard, A.L. Woern, R.B. Oakley, M.J. Fiedler, S.L. Snabes, J.M. Pearce, Green fab lab applications of large-area waste polymer-based additive manufacturing, Additive Manufacturing 27 (2019) 515-525.

[168] S.J. Park, J.E. Lee, H.B. Lee, J. Park, N.-K. Lee, Y. Son, S.-H. Park, 3D printing of bio-based polycarbonate and its potential applications in ecofriendly indoor manufacturing, Additive Manufacturing 31 (2020) 100974.

[169] R. Mülhaupt, Green Polymer Chemistry and Bio-based Plastics: Dreams and Reality, Macromolecular Chemistry and Physics 214(2) (2013) 159-174.

[170] S. Khoramnejadian, J.J. Zavareh, S. Khoramnejadian, Bio-based plastic a way for reduce municipal solid waste, Procedia Engineering 21 (2011) 489-495.

[171] E.H. Tümer, H.Y. Erbil, Extrusion-Based 3D Printing Applications of PLA Composites: A Review, Coatings 11(4) (2021) 390.

[172] R. Kumar, R. Singh, I. Farina, On the 3D printing of recycled ABS, PLA and HIPS thermoplastics for structural applications, PSU Research Review 2(2) (2018) 115-137.

[173] J. Wootthikanokkhan, T. Cheachun, N. Sombatsompop, S. Thumsorn, N. Kaabbuathong, N. Wongta, J. Wong-On, S.I. Na Ayutthaya, A. Kositchaiyong, Crystallization and thermomechanical properties of PLA composites: Effects of additive types and heat treatment, Journal of Applied Polymer Science 129(1) (2013) 215-223.

[174] M. Borish, B.K. Post, A. Roschli, P.C. Chesser, L.J. Love, K.T. Gaul, M. Sallas, N. Tsiamis, In-Situ Thermal Imaging for Single Layer Build Time Alteration in Large-Scale Polymer Additive Manufacturing, Procedia Manufacturing 34 (2019) 482-488.

[175] B.G. Compton, B.K. Post, C.E. Duty, L. Love, V. Kunc, Thermal analysis of additive manufacturing of large-scale thermoplastic polymer composites, Additive Manufacturing 17 (2017) 77-86.

[176] K. Choo, B. Friedrich, T. Daugherty, A. Schmidt, C. Patterson, M.A. Abraham, B. Conner, K. Rogers, P. Cortes, E. MacDonald, Heat retention modeling of large area additive manufacturing, Additive Manufacturing 28 (2019) 325-332.

[177] D. Bermudez, P.A. Quiñonez, E.J. Vasquez, I.A. Carrete, T.J. Word, D.A. Roberson, A Comparison of the physical properties of two commercial 3D printing PLA grades, Virtual and Physical Prototyping 16(2) (2021) 178-195.

[178] P.C. Hiemenz, T.P. Lodge, Polymer chemistry, CRC press2007.

[179] T. Ishinabe, A Molecular Theory of the Thermal Transitions of Polymers. II, Journal of the Physical Society of Japan 30(4) (1971) 1029-1035.

[180] M. Rinaldi, T. Ghidini, F. Cecchini, A. Brandao, F. Nanni, Additive layer manufacturing of poly (ether ether ketone) via FDM, Composites Part B: Engineering 145 (2018) 162-172.

[181] P. Parandoush, D. Lin, A review on additive manufacturing of polymer-fiber composites, Composite Structures 182 (2017) 36-53.

[182] J.W. Stansbury, M.J. Idacavage, 3D printing with polymers: Challenges among expanding options and opportunities, Dent Mater 32(1) (2016) 54-64.

[183] C. Duty, C. Ajinjeru, V. Kishore, B. Compton, N. Hmeidat, X. Chen, P. Liu, A.A. Hassen, J. Lindahl, V. Kunc, What makes a material printable? A viscoelastic model for extrusion-based 3D printing of polymers, Journal of Manufacturing Processes 35 (2018) 526-537.

[184] A. D'Amico, A.M. Peterson, An adaptable FEA simulation of material extrusion additive manufacturing heat transfer in 3D, Additive Manufacturing 21 (2018) 422-430.

[185] Y. Zhou, T. Nyberg, G. Xiong, D. Liu, Temperature Analysis in the Fused Deposition Modeling Process, (2016) 678-682.

[186] L. Vendland, V. Volkov-Muzylev, A. Demidov, Y.A. Borisov, Room temperature testing of PLA plastics, Journal of Physics: Conference Series, IOP Publishing, 2019, p. 012107.

[187] G. Surya Rao, K. Debnath, R.N. Mahapatra, Development and Characterization of PLA-Based Green Composites: Experimental and Simulation Studies, in: S. Thomas, P. Balakrishnan (Eds.), Green Composites, Springer Singapore, Singapore, 2021, pp. 209-223.

[188] J.R. Shewchuk, An introduction to the conjugate gradient method without the agonizing pain, Carnegie-Mellon University. Department of Computer Science, 1994.

[189] S.F. Costa, F.M. Duarte, J.A. Covas, Thermal conditions affecting heat transfer in FDM/FFE: a contribution towards the numerical modelling of the process, Virtual and Physical Prototyping 10(1) (2014) 35-46.

[190] A.-J.N. Khalifa, Natural convective heat transfer coefficient – a review, Energy Conversion and Management 42(4) (2001) 491-504.

[191] B. Brenken, Extrusion Deposition Additive Manufacturing of Fiber Reinforced Semi-Crystalline Polymers, Purdue University, 2017.

[192] R.V. Morgan, R.S. Reid, A.M. Baker, B. Lucero, J.D. Bernardin, Emissivity Measurements of Additively Manufactured Materials, (2017).

[193] S. Bhandari, R.A. Lopez-Anido, J. Anderson, A. Mann, Large-scale extrusion-based 3D printing for highway culvert rehabilitation, SPE ANTEC 2021, SPE, Virtual Conference, 2021.

APPENDIX A: FURTHER ANALYSIS OF BIMODULAR BEAM USING MOMENT-CURVATURE AND ULTIMATE TENSILE STRAIN-BASED FAILURE CRITERIA

The simply supported beam used in this study has a span of 101.6 mm, a width of 12.7 mm, and a height of 3.24 mm. Experimental observations showed that the beam withstood a deflection of nearly 25 mm. At this deflection, the curvature is huge and geometric non-linearity needs to be considered if a force-deflection analysis of the beam is to be carried out.

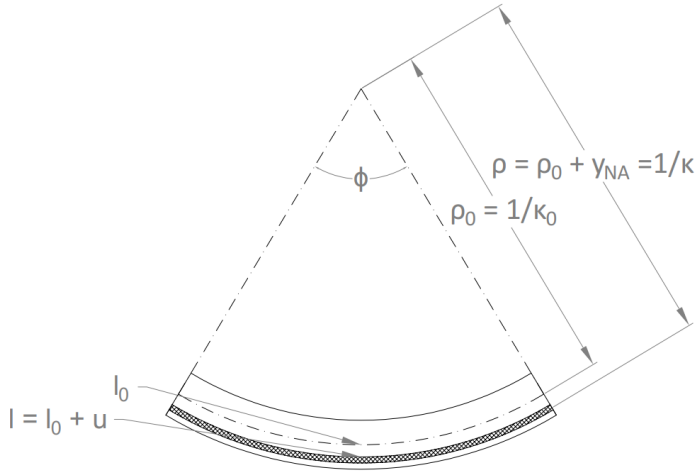

Figure 53: Displacements and radius of curvature in the fiber of a beam section.

Figure 53 shows a section of the bending element. In Figure, l_0 are the length of the fiber at the neutral axis and l is the length of the fiber at distance c from the neutral axis.

The arc lengths l and $l_0$are expressed as the product of the radial angle ϕ and the radius of curvature ρ and $\rho_0$respectively in Equation A1.1 and Equation A1.2. The extension of the fiber is expressed as the differences of arc lengths is shown by Equation A1.3. The strain in the fiber is shown by Equation A1.4 From Equation A1.5, where y_{NA} is the distance from the neutral axis to the strained fiber and Equation A1.6, the strain in the fiber can be reduced to Equation A1.7, where κ is the curvature.

$$l_0 = \phi\rho_0 \tag{A1.1}$$

$$l = \phi\rho \tag{A1.2}$$

$$u = l - l_0 \tag{A1.3}$$

$$\varepsilon_x = \frac{u}{l_0} = \frac{l - l_0}{l_0} = \frac{\phi\rho - \phi\rho_0}{\phi\rho_0} = \frac{\rho - \rho_0}{\rho_0} \tag{A1.4}$$

$$\rho = \rho_0 + y_{NA} \tag{A1.5}$$

$$\varepsilon_x = \frac{\rho_0 + y_{NA} - \rho_0}{\rho_0} \tag{A1.6}$$

$$\varepsilon_x = \frac{y_{NA}}{\rho_0} = y_{NA}\kappa \tag{A1.7}$$

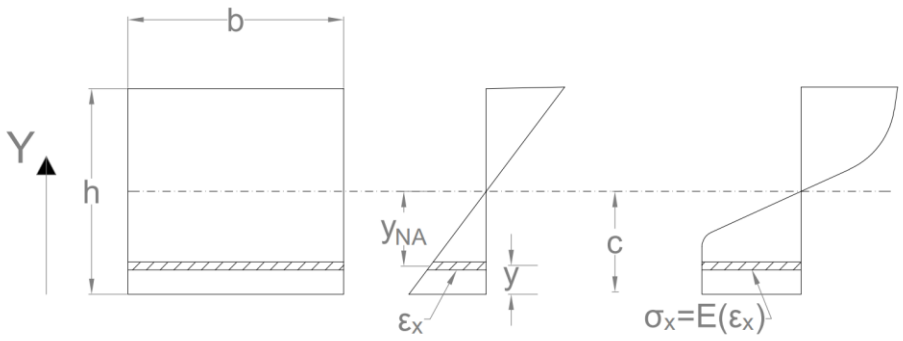

Figure 54: Strain and stress at the midspan cross-section in fibers of the bending element.

Figure 54 shows the strain and stress at the midspan cross-section in fibers of a bending element. y_{NA}can be expressed as Equation A1.8 in terms of distance from the bottom fiber, where y is the distance from the bottom fiber to the fiber in consideration. Equation A1.7 can be rewritten as Equation A1.9. Equation A1.10 shows the relation between the curvature and the deflection of the beam, where *w* is the deflection of the beam. For the thin beam used in this research work, which has a length to

depth ratio of 31.4, large rotations are observed which result in a large deflection of the beam. The denominator term in curvature cannot be ignored, and the bending is geometrically nonlinear.

$$y_{NA} = c - y \tag{A1.8}$$

$$\varepsilon_x = \frac{y_{NA}}{\rho_0} = (c - y)\kappa \tag{A1.9}$$

$$\kappa = \frac{\frac{d^2w}{dx^2}}{\left(1 + \left(\frac{dw}{dx}\right)^2\right)^{3/2}} \tag{A1.10}$$

The stress-strain relations are derived based on the material model presented in chapter 3. The MATLAB script used to derive the stress-strain relations is presented in Appendix B. Stress in the fiber can be expressed as a function of strain in the fiber as shown in Equation A1.11.

The location of the neutral axis in the bimodular elasto-plastic bending cross-section is found by equating compression forces with the tension forces as shown in Equation A1.12, where c_{guess} is the initial guess value provided for the distance of the neutral axis from the bottom fiber, and h is the height of the beam (3.24 mm). The numeric solution for the location of the neutral axis can be found by the Newton-Raphson method. The MATLAB script used to find the location of the neutral axis for different values of curvature is presented in Appendix B.

$$\sigma_x = E(\mathcal{E}_x) \tag{A1.11}$$

$$\int_0^{cguess} E((c_{guess} - y)\kappa)dy = \int_{cguess}^{h} E((c_{guess} - y)\kappa)dy \tag{A1.12}$$

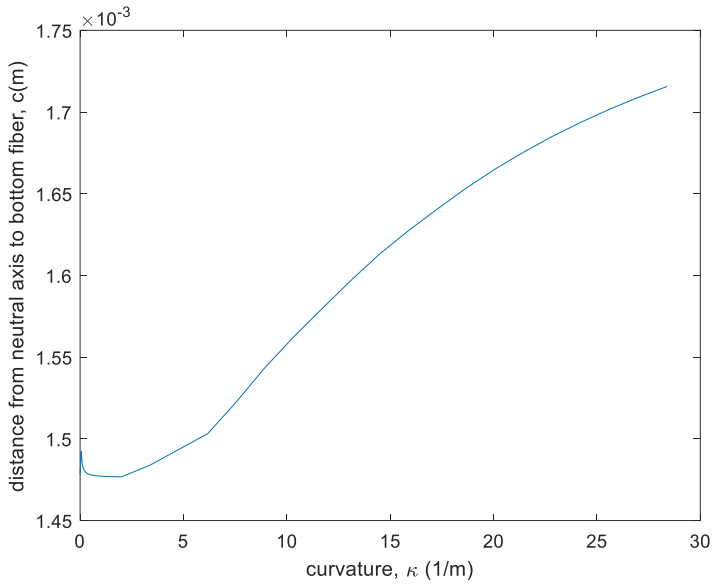

Figure 55: Location of neutral axis vs curvature of the cross-section.

Figure 55 shows how the location of the neutral axis changes with curvature. Initially, at very low curvatures, the neutral axis lies below the geometric centroid of the cross-section, since Young's modulus in tension is higher than that in compression. As curvature increases and partial yielding begins, the neutral axis shifts higher. The tangent stiffness in tension drops more rapidly compared to the tangent stiffness in compression and the material can withstand higher loads in compression. As a result, the neutral axis moves above the geometric centroid of the cross-section in this analysis.

The internal moment in the section that resists the external applied moment is calculated using Equation A1.13. The MATLAB script for calculating the internal moments resisted by the beam cross-section in elasto-plastic bending has been presented in Appendix B.

$$M_{int} = \int_0^{cguess} E((c_{guess} - y).\kappa).y.dy + \int_{cguess}^{h} E((c_{guess} - y).\kappa).y.dy \qquad \text{(A1.13)}$$

Figure 56 shows the Moment vs curvature diagram for the beam section considered for the study. The maximum moment resisted by the beam cross-section is predicted to be 1.604 Nm by the moment-curvature analysis. This maximum moment occurs at a curvature of 28.8 m^{-1}. The curvature is large and hence would result in large deflection before failure. Large midspan deflection of nearly 25 mm over a span of 101.6 mm was observed in the experiments.

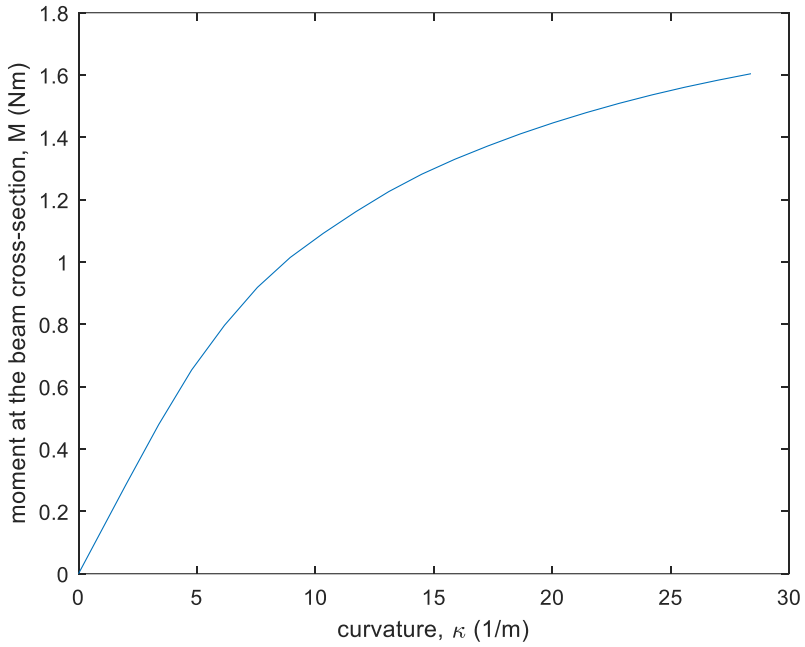

Figure 56: Moment vs curvature for the elasto-plastic bending of the beam.

For a simply-supported beam of span L loaded at midspan with a point load P, the moment at midspan is calculated using Equation A1.14. Equating external moments with internal moments for equilibrium and rearranging Equation A1.14 results in Equation A1.15.

$$M_{ext} = PL/4 \tag{A1.14}$$

$$P = 4 * M_{int}/L \tag{A1.15}$$

Plugging in the maximum moment of 1.62 Nm from the moment-curvature analysis, in equation A1.15, predicts a maximum load of 63.6 N, which is 8.0% lower than the mean experimental ultimate loads of 69.1 N. This prediction from the moment-curvature analysis is also very close to the maximum load of 67.3 N predicted by the finite element analysis with a bimodular yielding material model.

A new analysis was carried out to model failure using a strain-based failure in tension in the 1-direction. Strain at failure in the 1-direction was calculated by averaging the strain at failure values of the 1-direction specimen under tension loading. The mean value for strain at failure was calculated as 1.72%. A discounted ply method was used such that when the strain in the ply in 1-direction (layer) reached 1.72%, the stress in the ply was set to zero. Figure 57 shows the load vs displacement results from the finite element analysis using the failure criteria of 1.72% tensile strain in the 1-direction. The failure criteria based on tensile strain-based failure in the 1-direction predicts the first failure at 35.7 N at a displacement of 6.60 mm. Subsequent failures are observed with increasing displacements. The peak with maximum load is at 51.1 N at a displacement of 13.2 mm. The experimentally observed mean failure loads occurred at 69.1 N at a mean displacement of 27.1 mm.

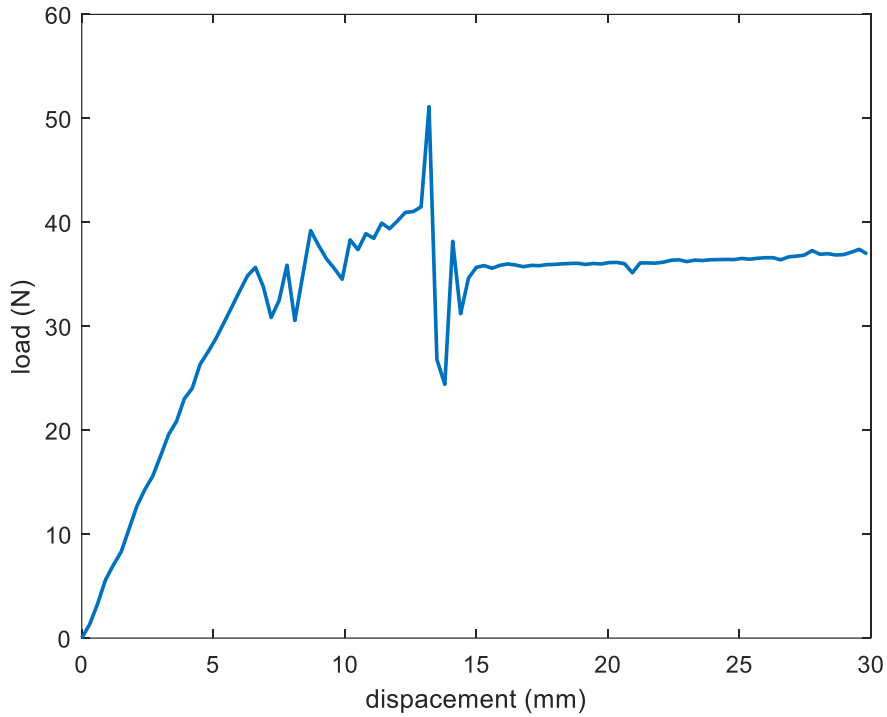

Figure 57: Load vs displacement with a failure strain of 1.72% in the 1-direction.

A simple strain-based failure criteria that used experimentally derived strain at failure from tension tests in 1-direction was not found to be a good predictor of failure of the specimen under bending loads. The simple failure criteria underpredicted the failure loads.

APPENDIX B: MATLAB SCRIPTS FOR GENERATING MOMENT-CURVATURE DIAGRAMS OF ELASTO-PLASTIC BIMODULAR BEAM BENDING

Bending_analysis_MK.m (script)

```
clc; clear all; close all;
%dimensions of beam
l = 101.6e-3; %length in m
b = 12.7e-3; %width in m
h = 3.24e-3; %height in m
layer_thickness = 3.6e-4;

%layup of beam
layup = [0,45,-45,90,0,90,-45,45,0];

%elastic constants
E1t = 5.70*1e9;
E1c = 3.58*1e9;
E2t = 2.17*1e9;
E2c = 2.32*1e9;
G12 = 0.851*1e9;
nu12t = 0.392;
nu12c = 0.391;
nu21t = 0.161;
nu21c = 0.137;

%calculate yield constants
sy = [21.5,12.9,23.5,21.4,14.4]*1e6; %yield stresses

% load hardening_curve_data
%
% %% create a table for stress strain relations for the different lamina
% % %orientations
%% the commented out coode generates the stress vs strain for different
%% orientations used in the laminate
%
% [strain0,stress0] = calc_stress_strain_relation_for_single_lamina(true,0, 0.05, 0,
10000, E1t, E2t, E1c, E2c,  nu12t, nu21t, nu12c, nu21c, G12, sy, hardening_curve);
% [strain1,stress1] = calc_stress_strain_relation_for_single_lamina(false,0, 0.05, 0,
10000, E1t, E2t, E1c, E2c,  nu12t, nu21t, nu12c, nu21c, G12, sy, hardening_curve);
%
% X = [fliplr(strain1),strain0(2:end)];
% Y = [-90,-45,0,45,90];
%
% V = zeros(size(Y,2),size(X,2));
%
% V(3,:) = [fliplr(stress1),stress0(2:end)];
%
% [strain0,stress0] = calc_stress_strain_relation_for_single_lamina(true,0, 0.05, -90,
10000, E1t, E2t, E1c, E2c,  nu12t, nu21t, nu12c, nu21c, G12, sy, hardening_curve);
% [strain1,stress1] = calc_stress_strain_relation_for_single_lamina(false,0, 0.05, -
90, 10000, E1t, E2t, E1c, E2c,  nu12t, nu21t, nu12c, nu21c, G12, sy, hardening_curve);
% V(1,:) = [fliplr(stress1),stress0(2:end)];
%
% [strain0,stress0] = calc_stress_strain_relation_for_single_lamina(true,0, 0.05, -45,
10000, E1t, E2t, E1c, E2c,  nu12t, nu21t, nu12c, nu21c, G12, sy, hardening_curve);
% [strain1,stress1] = calc_stress_strain_relation_for_single_lamina(false,0, 0.05, -
45, 10000, E1t, E2t, E1c, E2c,  nu12t, nu21t, nu12c, nu21c, G12, sy, hardening_curve);
% V(2,:) = [fliplr(stress1),stress0(2:end)];
%
```

```
% [strain0,stress0] = calc_stress_strain_relation_for_single_lamina(true,0, 0.05, 45,
10000, E1t, E2t, E1c, E2c,  nu12t, nu21t, nu12c, nu21c, G12, sy, hardening_curve);
% [strain1,stress1] = calc_stress_strain_relation_for_single_lamina(false,0, 0.05, 45,
10000, E1t, E2t, E1c, E2c,  nu12t, nu21t, nu12c, nu21c, G12, sy, hardening_curve);
% V(4,:) = [fliplr(stress1),stress0(2:end)];
%
% [strain0,stress0] = calc_stress_strain_relation_for_single_lamina(true,0, 0.05, 90,
10000, E1t, E2t, E1c, E2c,  nu12t, nu21t, nu12c, nu21c, G12, sy, hardening_curve);
% [strain1,stress1] = calc_stress_strain_relation_for_single_lamina(false,0, 0.05, 90,
10000, E1t, E2t, E1c, E2c,  nu12t, nu21t, nu12c, nu21c, G12, sy, hardening_curve);
% V(5,:) = [fliplr(stress1),stress0(2:end)];
% save('strain_orientation_stress_table', 'X','Y','V');

%load strain_orientation_stress_table.mat

%% create a range of curvatures and calculate moments for them
phi =
[linspace(0,2.0,40),linspace(2.0,28.37,20),linspace(28.37,30.39,10)];%linspace(0,pi/2*
.95,20);



moments1 = zeros(size(phi));
moments2 = zeros(size(phi));
nas = zeros(size(phi));
moments = zeros(size(phi));

for i = 1:size(phi,2)
    % find neutral axis
    % find compression force
    tens =@(cguess) integral(@(y)
map_y_to_stress(phi(i),layup,layer_thickness,X,Y,V,cguess,y),0,cguess);
    comp = @(cguess) integral(@(y)
map_y_to_stress(phi(i),layup,layer_thickness,X,Y,V,cguess,y),cguess,h);
    '';% this is here so that this line can be used as breakpoint for debugging

    % function equating the compression forces with the tension forces

    f = @(cguess) (tens(cguess)+comp(cguess))*1e8;
    if i>1
        naguess = nas(i-1);
    else
        naguess =  0.001478403695826;
    end
    nas(i) = fsolve(f, naguess);
    cguess =nas(i);
    moments1(i) =   b*(integral(@(y)
map_y_to_stress(phi(i),layup,layer_thickness,X,Y,V,cguess,y).*(cguess-y),0,cguess));
    moments2(i) =  b*(integral(@(y)
map_y_to_stress(phi(i),layup,layer_thickness,X,Y,V,cguess,y).*(cguess-y),cguess,h));
    i
    '';% this is here so that this line can be used as breakpoint for debugging

end
moments = moments1+moments2;
plot(phi,nas);
xlabel('curvature, \kappa (1/m)')
ylabel('distance from neutral axis to bottom fiber, c(m)')
figure
plot(phi,moments1+moments2)
xlabel('curvature, \kappa (1/m)');
```

```
ylabel('moment at the beam cross-section, M (Nm)')
```

map_y_to_stress.m *(function)*

```
function [stress] = map_y_to_stress(phi, layup, layer_thickness, X,Y,V, cguess,y)
%MAP_Y_TO_STRESS for a given phi, map y to stress for a given laminate

%stress = 0;
curvature = phi;
%curvature = tan(phi);
strain = curvature*(cguess-y);
%layup_thickness = layer_thickness*size(layup,2);
laminate_location = ceil(y/layer_thickness);
if laminate_location == 0
    laminate_location = 1;
end
orientation = layup(laminate_location);

yloc = zeros(size(orientation));

for i = 1:size(yloc,2)
   for j = 1:size(layup,2)
       if orientation(i) == Y(j)
           yloc(i) = j;
           break;
       end
   end
end

stress = zeros(size(y));
for i = 1:size(y,2)
    stress_curve = V(yloc(i),:);
    stress(i) = interp1(X,stress_curve,strain(i));
end
'';
end
```

calc_stress_strain_relation_for_a_single_lamina.m *(function for material model)*

```
function [strains,stresses_x] =
calc_stress_strain_relation_for_single_lamina(positive,strainbegin, strainend,
orientation, numdivs, E1t, E2t, E1c, E2c,  nu12t, nu21t, nu12c, nu21c, G12, sy,
hardening_curve)
%strainbegin = 0;
%strainend = 5/100;
%orientation = 0;
%numdivs = 10000;
if positive
    %'positive'
    strains = linspace(strainbegin, strainend, numdivs);
else
    %'negative'
    strains = -linspace(strainbegin, strainend, numdivs);
end

stress_lamina = zeros(3,numdivs);
stresses_x = zeros(1,numdivs);
dstrain = strains(2)-strains(1);
hs = zeros(0,numdivs);
```

```
m = cosd(orientation);
n = sind(orientation);
T = [m^2, n^2, 2*m*n; n^2, m^2, -2*m*n; -m*n, m*n, m^2-n^2];
R = [1 0 0; 0 1 0; 0 0 2];

for i = 2:numdivs%size(strains,2)

    dstrain_lamina = R*T*inv(R)*[dstrain 0 0]';
    if stress_lamina(1,i-1) >= 0
        E1 = E1t;
        nu21 = nu21t;
    else
        E1 = E1c;
        nu21 = nu21c;
    end

    if stress_lamina(2,i-1) >= 0
        E2 = E2t;
        nu12 = nu12t;
    else
        E2 = E2c;
        nu12 = nu12c;
    end

    % calculate stiffness matrix for lamina
    S = [1/E1, -nu21/E2,0; -nu12/E1, 1/E2, 0;0,0,1/G12]; %compliance matrix
    C = inv(S); %stiffness matrix

    % calculate stress in lamina in local coordinates
    dstress_lamina = C*dstrain_lamina;

    % calculate Hill's stress to check if yielding
    %R1 = yield_coefficients(1);
    if stress_lamina(1,i-1) >= 0
        %R2 = yield_coefficients(2);
        %R6 = yield_coefficients(3);
        %F = 0.5* (1/sy(2)^2+1/sy(2)^2-1/sy(1)^2);
        %G = 1/2* (1/sy(2)^2+1/sy(1)^2-1/sy(2)^2);
        %H = 1/2*(1/sy(1)^2+1/sy(2)^2-1/sy(12)^2);
        F = 1/2 * (1/sy(2)^2*2 -1/sy(1)^2);
        G = 1/2 * (1/sy(1)^2);
        H = 1/2 * (1/sy(1)^2);
        N = 1/2 *1/sy(5)^2;

    else
        %R2 = yield_coefficients(5);
        %R6 = yield_coefficients(4);
        F = 1/2 * (1/sy(4)^2*2 -1/sy(3)^2);
        G = 1/2 * (1/sy(3)^2);
        H = 1/2 * (1/sy(3)^2);
        N = 1/2 * 1/sy(5)^2;
    end


    %F = 0.5*(1/R2^2-1/R1^2);
    %G = 0.5*(1/R1^2-1/R2^2);
    %H = 0.5*(1/R1^2+1/R2^2);
    %N = 3/R6^2;
```

```
    if stress_lamina(1,i-1) > 1
        sigy1 = sy(1);
    else
        sigy1 = sy(3);
    end

    % calculate Hills stress
    f_hill = calc_hills_yield_stress(F,G,H,N,stress_lamina(:,i-1),sigy1);%

    %yield check based on sigy1
    dStress = C*dstrain_lamina;

    %check for yield
    if f_hill > sigy1
        %directions

        % calculate hardening coefficient
        if stress_lamina(1,i-1) >= 0
            hstrain = hardening_curve(:,1);
            hstress = hardening_curve(:,2);
        else
            hstrain = hardening_curve(:,3);
            hstress = hardening_curve(:,4);
        end

        df_ds_den = calc_hills_yield_stress(F,G,H,N,stress_lamina(:,i-1),sigy1);
        df_ds(1,1) = 2*stress_lamina(1,i-1)*(G+H)/df_ds_den;
        df_ds(2,1) = 2*stress_lamina(2,i-1)*(F-H)/df_ds_den;
        %df_ds(3,1) = 0;
        df_ds(3,1) = 2*N*stress_lamina(3,i-1)/df_ds_den;
        ncap = df_ds/norm(df_ds);

        %calculate hardening coefficient
        [~,loc] = min(abs(hstress-df_ds_den));
        if loc < size(hstress,1)
            h = (hstress(loc)-hstress(loc+1))/(hstrain(loc)-hstrain(loc+1));
        else
            h = 1e-7;
        end
        hs(i) = h;

        %plastic strain multiplier
        dlambda = (ncap' * C * dstrain_lamina)/(ncap'*C*ncap+h);

        dStress = C *(dstrain_lamina - dlambda * ncap);
    end

    stress_lamina(:,i) = stress_lamina(:,i-1) + dStress;
    stress_global = inv(T) * stress_lamina(:,i);
    stresses_x(i) = stress_global(1);

end
end
```

BIOGRAPHY OF THE AUTHOR

Sunil Bhandari was born in Nepal. He was raised in Pokhara, Nepal and graduated from Budhanilkantha School, Kathmandu in 2007. He attended Tribhuvan University and graduated in 2012 with a Bachelor's degree in Civil Engineering. He started the Civil Engineering graduate program at The University of Maine in the fall of 2014. Sunil graduated from the Master's degree program in May 2017 and started his Ph.D. in Civil Engineering in June 2017. Sunil is a candidate for the Doctor of Philosophy degree in Civil Engineering from the University of Maine in December 2021.